



Raymond and Beverly Sackler
Faculty of Exact Sciences
School of Physics and Astronomy

Research Thesis for a degree "Doctor of Philosophy"

Pattern Formation in Thin Elastic Sheets

Submitted to the Senate of Tel Aviv University by

Oz Oshri

Advisor: Prof. Haim Diamant

February 2017

This research was carried out under the supervision of
Professor Haim Diamant
Tel-Aviv University

Abstract

The study of pattern formation in general, and patterns on thin elastic sheets in particular, is at present an active field of research. A thin elastic sheet is a 3D solid material whose thickness is much smaller compared with its other dimensions. Due to this unique geometric property thin sheets are highly deformable and exhibit numerous morphological structures under external loads or confinement. This thesis aims to advance the theory of thin elastic sheets through the following three projects.

The first project deals with a laterally confined thin elastic sheet that is lying on a liquid substrate. Upon small confinement this system displays regular undulations, called wrinkles, characterized by a spatially extended energy distribution and a well-defined wavelength λ . As the confinement increases, the deformation energy is progressively localized into a single narrow fold. An exact solution for the deformation of an infinite sheet was previously found, indicating that wrinkles in an infinite sheet are unstable against localization for arbitrarily small confinement. We present an extension of the theory to sheets of finite length L , accounting for the experimentally observed wrinkle-to-fold transition. We derive an exact solution for the strong periodic deformation in the wrinkled state, and an approximate solution for the localized, folded state. We find that a second-order transition between these two states occurs at a critical confinement $\Delta_F = \lambda^2/L$.

In the second project we study the analogy between thin filaments (also equivalent to thin sheets that deform uniaxially) and the motion of rigid bodies. Kirchhoff's kinetic analogy relates the deformation of an incompressible elastic rod to the classical dynamics of rigid body rotation. We advance the analogy further to extensible filaments and find that this is equivalent to the introduction of relativistic effects into the dynamical system. The extended analogy reveals a surprising symmetry in the deformations of extensible elastica. In addition, we use known results for the buckling of extensible elastica to derive the explicit solution for the motion of a relativistic nonlinear pendulum. We discuss cases where the extended Kirchhoff analogy may be useful for the study of other soft matter systems.

The third project is on the subject of incompatible thin sheets — sheets that include residual stresses even in the absence of external forces. The existing theory of incompatible elastic sheets uses the deviation of the surface metric from a prescribed reference metric to define the strain tensor. For a class of simple axisymmetric problems we present and examine an alternative formulation, defining the strain based on deviations of distances (rather than distances squared) from their rest values. While the two formulations converge in the limit of small slopes and in the limit of an incompressible sheet, for other cases they are found not to be equivalent. The alternative formulation offers several features which are absent in the existing theory. (a) In the case of planar deformations of flat incompatible sheets, it yields linear, exactly solvable, equations of equilibrium. (b) When reduced to uniaxial (one-dimensional) deformations, it coincides with the theory of extensible elastica; in particular, for a uniaxially bent sheet it yields an unstrained cylindrical configuration. (c) It gives a simple criterion determining whether

a strain-free configuration (isometric immersion) of an incompatible sheet is at mechanical equilibrium with respect to normal forces. For a reference metric of constant positive Gaussian curvature, a spherical cap is found to satisfy this criterion except in an arbitrarily narrow boundary layer.

Overall, the results of this thesis make another step towards a complete, non-linear, elastic theory that is able to describe arbitrarily large deformations of thin elastic sheets far away from their relaxed state.

Acknowledgments

I am most indebted to my advisor Prof. Haim Diamant for his guidance and support during the PhD. I am especially grateful to him for introducing me to the field of thin sheets elasticity, for suggesting the research on extensible filaments and incompatible sheets and for sharing with me his illuminating ideas.

I also want to thank Prof. David Andelman for suggesting me to cooperate with Haim and for helpful comments on my work, to Prof. Christian D. Santangelo and Prof. Benjamin Davidovitch for many helpful discussions in early stages of this work.

I thank my colleagues, Tomer, Yulia and Chen, for helpful discussions and useful suggestions.

And last, but not least, I would like to thank my wife, Taly, for her love, encouragements, and understanding during these years.

Contents

| | | |
|----------|---|-----------|
| 1 | Introduction | 1 |
| 1.1 | Background | 1 |
| 1.2 | Uniaxial deformations of thin sheets | 5 |
| 1.3 | The elastic theory of two-dimensional thin sheets | 12 |
| 1.4 | Outline of the Thesis | 21 |
| 2 | Wrinkles and folds in a fluid-supported sheet of finite size | 23 |
| 2.1 | Introduction | 23 |
| 2.2 | System and governing equation | 25 |
| 2.3 | Exact periodic solutions | 27 |
| 2.4 | Approximate localized solutions | 31 |
| 2.5 | Wrinkle-to-fold transition | 38 |
| 2.6 | Discussion | 41 |
| 3 | Properties of extensible elastica from relativistic analogy | 45 |
| 3.1 | Introduction | 45 |
| 3.2 | The elastic energy from a discrete model | 46 |
| 3.3 | Analogy to relativistic dynamics | 47 |
| 3.4 | Symmetry of extensible elastica | 48 |
| 3.5 | Exact solution to the relativistic non-linear pendulum | 50 |
| 3.6 | Discussion | 53 |
| 4 | Strain tensor selection and the elastic theory of incompatible thin sheets | 55 |
| 4.1 | Introduction | 55 |
| 4.2 | Alternative two-dimensional formulation for simple deformations | 57 |
| 4.3 | Uniaxial deformation by bending | 62 |
| 4.4 | Exact solutions for planar deformations of incompatible sheets | 65 |
| 4.5 | Stability criterion for isometric immersions | 72 |
| 4.6 | Discussion | 75 |
| 5 | Concluding remarks and future directions | 79 |
| 5.1 | The problem of floating elastica | 79 |

| | |
|--|------------|
| CONTENTS | 1 |
| 5.2 Elastic-kinetic analogies | 80 |
| 5.3 The elastic theory of incompatible sheets | 81 |
| Appendices | 85 |
| A Wrinkles and folds in a fluid supported sheet - Appendices | 87 |
| A.1 Exact localized solutions to Eq. (2.8) | 87 |
| A.2 Accuracy of Δ_F and P_F | 90 |
| A.3 Scaling approach | 92 |
| B Analogy between extensible elastica and relativistic dynamics — Appendices | 95 |
| B.1 On Galilean and Lorentz invariance of a free extensible filament | 95 |
| B.2 Analogy between extensible 3D Kirchhoff's rod and relativistic rotor | 103 |
| B.3 Minimization of Eq. (B.26) | 105 |
| C Strain tensor selection - Appendices | 107 |
| C.1 Consistent energy minimization for a uniaxially deformed sheet | 107 |
| C.2 Boundary layer in a sheet with elliptic reference metric | 109 |
| C.3 Stability criterion for isometric immersions with negative Gaussian curvature . . | 112 |
| C.4 Comparison between thin sheet theories based on model-independent force-balance equations | 114 |

Chapter 1

Introduction

1.1 Background

Pattern formation refers to macroscopic and mesoscopic ordered structures that spontaneously emerge out of a uniform environment as an instability or symmetry breaking [1–3]. Numerous phenomena in nature are gathered under this master field. Examples are plentiful, e.g., large scale structures in the universe, solidification of snowflakes out of vapor, creation of sand ripples or fluid vortices in thermal convection. Almost every industrial manufacturing process involves at one stage or another some version of pattern formation [2]. Since designing a material to have a certain shape and functionality has always been of great importance, many studies on pattern formation concentrated on elasticity phenomena.

1.1.1 Elastic bodies

The theory of elasticity was founded as a tool for describing the behavior of a macroscopic three-dimensional (3D) solid material under applied external forces.

In a nutshell, the mathematical formulation of elasticity aims to describe how the relaxed configuration, \mathbf{r}_0 , is deformed into $\mathbf{r} = \mathbf{r}_0 + \mathbf{u}$, under the application of external loads, \mathbf{f}_{ext} . The vector \mathbf{u} is called the displacement vector and determining its components is the main goal of the elastic theory. For this purpose two tensors are defined: (i) The strain tensor, $\epsilon_{ij}(\mathbf{u})$ (where $i, j = 1, 2, 3$), which measures the extension of line elements with respect to their rest

values, and (ii) the stress tensor, σ_{ij} , which measures the internal forces within the deformed configuration. The elastic energy of a given configuration is the work done to displace the 3D body from its rest state,

$$E_{3D} = \int_{\mathcal{V}} \sigma_{ij} \epsilon_{ij} dV, \quad (1.1)$$

where \mathcal{V} is the total volume of the undeformed configuration. Expressing the stresses as a function of the strains, the so-called constitutive stress-strain relations, one can minimize the elastic energy under the given constraints and solve the equilibrium equations to obtain the deformed configuration. An important limit of this formalism is the framework of linear elasticity. If the strains, ϵ_{ij} , are small we may assume that the stress-strain relations are linear, $\sigma_{ij} = A_{ijkl} \epsilon_{kl}$, such that Eq. (1.1) becomes quadratic in ϵ ,

$$\text{small strains: } E_{3D} = \int_{\mathcal{V}} A_{ijkl} \epsilon_{ij} \epsilon_{kl} dV. \quad (1.2)$$

In the last few decades there has been a renewed interest in elasticity theory as nano-scale structures were considered either for engineering or for fundamental science [4]. Although the theory was developed to fit a macroscopic continuous material of the size that we see with a naked eye, it turns out to reasonably describe more delicate structures such as DNA rings [5] and carbon nanotubes [6]. In addition, patterns appearing on the surface of soft materials and biological tissues, such as wrinkles on human skin [7], sulcus in the human brain [8], or curvature excitations of red blood cells [9], were described to great accuracy by elastic theories. These observations resulted in the expansion of elasticity into the high bendability regime [10–12] — phenomena in which thin elastic bodies are free to undergo large deflections far away from their initial state.

1.1.2 Thin sheets

A large group of these highly bendable materials lies in the category of *thin elastic sheets*. A thin elastic sheet is a solid material whose thickness is small compared with its other dimensions, for instance office paper, curtains, T-shirt fabric and leaves, see Fig. 1.1.

The theoretical framework of thin sheet elasticity has its roots in the standard linear elasticity in three-dimensions, Eq. (1.2), where on top of the small strains approximation another set of assumptions are used that effectively reduce the problem’s dimensionality. These assumptions are known as the *Kirchhoff-Love* hypotheses and are formulated as follows [15, p. 65]: “straight

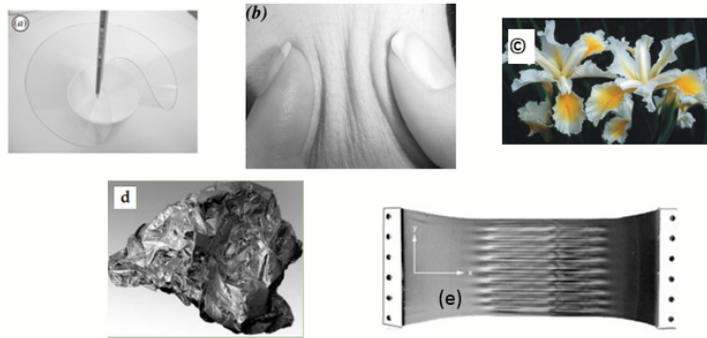


Figure 1.1: Different morphologies of thin elastic sheets. (a) Packing of a flat thin sheet in a hollow cylinder results in a conical deformation [13]. (b) Wrinkles on a human skin due to lateral compression [7]. (c) Wrinkles on the edge of flower petals. (d) Crumpled sheet of aluminized Mylar [14]. (e) Wrinkles in a polyethylene sheet under a uniaxial tensile strain [7].

transverse fibers of the sheet which were normal to the middle surface before the deformation remain straight and normal to the deformed middle surface and do not undergo any stretching or compression”. Physically, these assumptions neglect the stress-strain relations along the thin direction, such that the thickness remains unchanged (see [15] for further discussion). The main benefit from these hypotheses is that a 3D thin sheet can be modeled by the deformation of its two-dimensional (2D) mid-surface, and similarly, a slender filament can be represented by its one-dimensional (1D) mid-axis.

Mathematically, a deformed 3D body that satisfies the Kirchhoff-Love assumptions is given by,

$$\mathbf{f}^*(x_1, x_2, x_3) = \mathbf{f}(x_1, x_2) + x_3 \hat{\mathbf{n}}(x_1, x_2), \quad (1.3)$$

where $\mathbf{f}^*(x_1, x_2, x_3)$ is the position vector of the 3D configuration, $\mathbf{f}(x_1, x_2)$ is the position vector of the mid-surface, (x_1, x_2) are the two in-plane coordinates, x_3 is the coordinate along the thin direction and $\hat{\mathbf{n}}$ is a unit vector normal to the mid-surface. Since the dependence on x_3 is explicit, given the mid-surface, $\mathbf{f}(x_1, x_2)$, the entire 3D body can be constructed (see Fig. 1.2). The limits of validity of these assumptions were extensively investigated in Refs. [15–18]. It can be shown that these assumptions are expected to hold as long as $t/R_{\min} \ll 1$, where R_{\min} is the minimum radius of curvature on the surface and t is the thickness.

Intuitively, as a material becomes thinner, its ability to oppose bending is dramatically reduced. Quantitatively, using the Kirchhoff-Love hypotheses, the elastic energy, Eq. (1.2), can

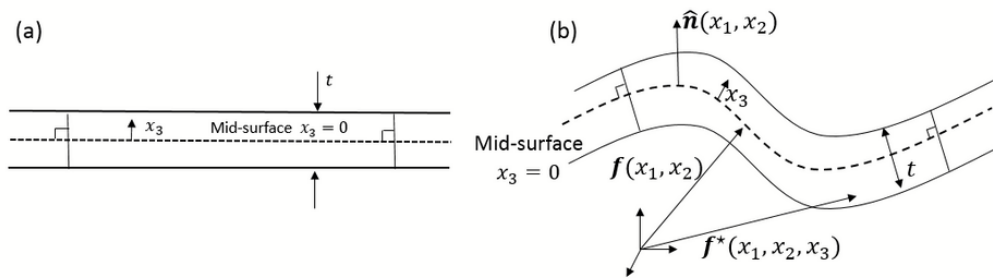


Figure 1.2: Deformation of a plate under the Kirchhoff-Love assumptions. An initially stress-free and flat plate with thickness t in panel (a) is deformed into the configuration presented in panel (b). Since straight lines (“fibers”) normal to the mid-surface remain straight and normal after deformation and the thickness remains unchanged, the 3D configuration is fully determined by the position of the mid-surface.

be integrated over the thin dimension of the 3D body to give the following expansion,

$$E_{2D} \simeq E_s + E_b = Y \int_{\mathcal{A}} e_s dA + B \int_{\mathcal{A}} e_b dA, \quad (1.4)$$

where E_s and E_b account respectively for the energies associated with the in-plane and out-of-plane deformations and the integration is over the undeformed area of the sheet. Since the bending term, E_b , is proportional to the bending rigidity given by $B \propto Et^3$, where E is the Young’s modulus, and the stretching contribution, E_s , is proportional to the compression modulus, $Y \propto Et$, the relative energetic cost for bending is greatly reduced with decreasing thickness [19, p.50].

The rest of this Introduction is divided into three sections. In the first, Sec. 1.2, we introduce the elastic theory of 1D extensible filaments (the so-called extensible elastica). This theory holds as well for 2D sheets that deform uniaxially along a single direction (with zero Gaussian curvature¹). We then utilize this theory for two applications: (i) formulating the problem of floating elastica - a thin sheet that overlies a fluid substrate and uniaxially compressed from the boundaries, and (ii) demonstrating the analogy between thin planar filaments and a dynamic problem. The second section in this Introduction, Sec. 1.3, presents the general theory for thin sheets in two dimensions, accounting for arbitrary deformations along the two in-plane directions on the surface. We then specialize this formulation to two cases: (i) the small slope approximation (also known as the Föppl-von Kármán model), and (ii) the elastic theory of incompatible thin sheets. Finally, in Sec. 1.4, we present the outline of this thesis.

¹The Gaussian curvature at a point on a surface is the product of its two principal curvatures at that point [20].

1.2 Uniaxial deformations of thin sheets

1.2.1 The theory of extensible elastica

The mathematical theory of thin filaments (or uniaxially deformed sheets) which are inextensible along their mid-axis was first derived by Euler [21]. By minimizing the square curvature functional Euler obtained the general equation for the deflection of an elastic rod (the so-called *elastica*) [21, 22]. Since then, thin inextensible filaments have been extensively investigated, for example, in the context of structural engineering [22, 23], and biological tissues [24–27]. Less attention was given in the literature to extensible filaments (the so-called model of extensible elastica) due to the seemingly insignificant effect of extensibility in the limit of small thickness. Nevertheless, as extensible elastica will be important for Chapters 3 and 4, we review here the relevant literature and briefly derive its main equations.

Consider a straight, stress-free, filament of relaxed length L and relaxed arclength parameter, s . A planar deformation away from the relaxed state is parametrized by two fields, the angle $\phi(s)$ (see Fig. 1.3a) and the strain $\gamma(s) = d\hat{s}/ds$, where \hat{s} is the arclength parameter in the deformed configuration. In addition, we define the co-moving orthonormal coordinate system $\{\hat{\mathbf{t}}(s), \hat{\mathbf{n}}(s)\}$, tangent and normal to the filament at a position s .

Following Fig. 1.3b and balancing the forces and moments that are applied on an infinitesimal segment of the filament, we immediately obtain the conditions for mechanical equilibrium,

$$0 = \frac{d\sigma_{ss}}{ds} - \gamma\kappa\sigma_{ns}, \quad (1.5a)$$

$$0 = \frac{d\sigma_{sn}}{ds} + \gamma\kappa\sigma_{ss} - \gamma F, \quad (1.5b)$$

$$0 = \frac{dM_{ss}}{ds} + \gamma\sigma_{sn}, \quad (1.5c)$$

where $F(s)$ is an external force per unit length in the normal direction (not drawn in Fig. 1.3b) and $\kappa = d\phi/d\hat{s}$ is the curvature. Since Eqs. (1.5) form a system of three equations for five unknowns $\{\sigma_{ss}, \sigma_{sn}, M_{ss}, \gamma, \kappa\}$, some constitutive relations that relate the stress and torque to the actual configuration are required to have a closure. In the framework of extensible elastica these constitutive relations are given by [22, 28–34],

$$\sigma_{ss}(s) = Y\epsilon_{ss}, \quad (1.6a)$$

$$M_{ss}(s) = B\phi_{ss}, \quad (1.6b)$$

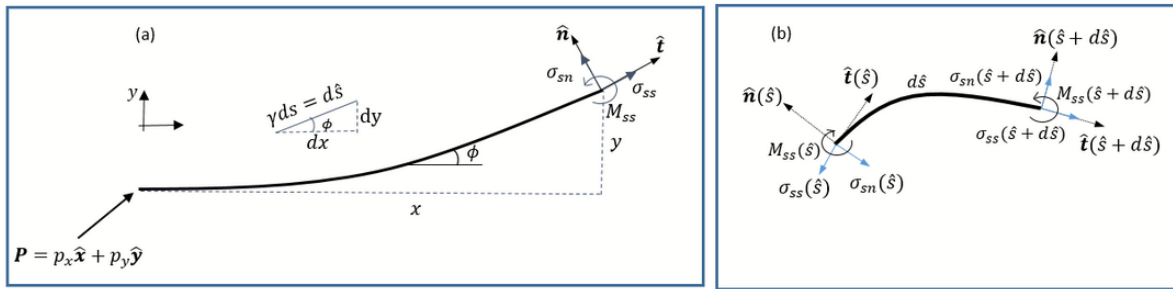


Figure 1.3: Balance of forces on finite and infinitesimal segment of the sheet. (a) Force and torque balance on a finite segment of the filament. It is straightforward to verify from this schematic drawing that that balance gives Eqs. (1.8). (b) Illustration of force balance on an infinitesimal segment of the filament, $d\hat{s}$. Balance of forces in the tangential direction, $\hat{t}(\hat{s})$, is given by, $-\sigma_{ss}(\hat{s}) + \sigma_{ss}(\hat{s} + d\hat{s})\hat{t}(\hat{s} + d\hat{s}) \cdot \hat{t}(\hat{s}) + \sigma_{sn}(\hat{s} + d\hat{s})\hat{n}(\hat{s} + d\hat{s}) \cdot \hat{t}(\hat{s}) = 0$. Expanding this equation to leading order in the differential $d\hat{s}$ we obtain $d\sigma_{ss}/d\hat{s} - \kappa\sigma_{sn} = 0$. Transforming back to ds yields Eq. (1.5a). Similarly, force balance in the normal direction and balance of bending moments gives Eqs. (1.5b) and (1.5c).

where $\epsilon_{ss} = \gamma - 1$ and $\phi_{ss} = d\phi/ds$ are the the 1D strain “tensor” and bending-strain [30, p. 98]. In summary, Eqs. (1.5) and the constitutive relations, Eqs. (1.6), form a closed system of five equations for five unknowns.

The extensible elastica model, Eqs. (1.5), reduces to Euler’s elastica in the limit of inextensibility, $\gamma = 1$ (implying $\hat{s} = s$). In this limit the first constitutive relation, Eq. (1.6a), is redundant and the second one, Eq. (1.6b), reduces to $M_{ss} = B\dot{\phi}$, where $\dot{\phi} = d\phi/ds = \kappa$ is the curvature. Substituting this relation in Eqs. (1.5c) and (1.5a) we obtain the normal stress, $\sigma_{sn} = -B\ddot{\phi}$, and the in-plane stress, $\sigma_{ss} = -(B/2)\dot{\phi}^2 - p_t$, where p_t is the external force at the boundary in the tangent direction. Substituting the latter relations in Eq. (1.5b) gives,

$$B\ddot{\phi} + B(\dot{\phi}^2/2 + p_t)\dot{\phi} + F = 0. \quad (1.7)$$

This equation coincides with Euler’s elastica [22]. It expresses balance of normal forces on infinitesimal segment of an inextensible filament.

In special cases, where the external forces act only on the filament edges, $F(s) = 0$, Eqs. (1.5) become integrable and the equations of extensible elastica take a somewhat simpler form (including derivatives of lower order). Once integrated, these equations describe balance of forces and torques on a finite (rather than infinitesimal) segment of the filament, as illustrated in

Fig. 1.3a. These equations read,

$$0 = \sigma_{ss} + p_x \cos \phi + p_y \sin \phi, \quad (1.8a)$$

$$0 = \sigma_{sn} - p_x \sin \phi + p_y \cos \phi, \quad (1.8b)$$

$$0 = M_{ss} + p_x y - p_y x, \quad (1.8c)$$

$$dx/ds = \gamma \cos \phi, \quad (1.8d)$$

$$dy/ds = \gamma \sin \phi, \quad (1.8e)$$

where p_x and p_y are the components of the external force in the horizontal and vertical directions (see Fig. 1.3a). Equations (1.6) and (1.8) form a closure; we now have a system of seven equations for seven unknowns $\{\sigma_{ss}, \sigma_{sn}, M_{ss}, \gamma, \kappa, x, y\}$.

Lastly, the energy functional of the filament is given by,

$$\begin{aligned} E_{1D} &= E_s + E_b + W_{ext} = \frac{1}{2} \int_0^L (\sigma_{ss} \epsilon_{ss} + M_{ss} \phi_{ss}) ds + W_{ext} \\ &= \int_0^L \left[\frac{B}{2} \left(\frac{d\phi}{ds} \right)^2 + \frac{Y}{2} (\gamma - 1)^2 \right] ds + W_{ext}, \end{aligned} \quad (1.9)$$

where W_{ext} is the work of the external forces and in the second line we have used the constitutive relations, Eq. (1.6). We note that this functional is derived in Chapter 3 as the continuum limit of a jointly connected chain of elastic rods, and as discussed there it has the key property of keeping bending and stretching contributions independent.

As noted in Ref. [28], the extensible elastica problem was first derived by Pflüger [35]. Exact solutions to this model in terms of elliptic integrals can be found in Ref. [36]. Based on a virtual-work procedure, the extensible elastica equations were also derived in Refs. [28, 30, 34] for an arbitrary beam cross-section. In Ref. [28] a complete linear stability analysis was performed for the case of an extensible filament under hinged boundary conditions. Several nontrivial effects were noted in this study, and here we mention three of them: (i) The critical buckling load depends on the slenderness of the beam, YL^2/B , where L is the total relaxed length. (ii) The buckling instability has a finite number of unstable modes when extensibility corrections are taken into account. This is in contrast to the infinite number of modes in the inextensible case. (iii) The critical flat-to-buckle bifurcation becomes subcritical at slenderness values of order one, unlike the supercritical bifurcation in the inextensible case. Humber extended the work in [28] to include clamped-clamped and clamped-hinged boundary conditions. Lately, exact solutions of this model in terms of Jacobi elliptic functions were given in Ref. [37]. In Ref. [38] an extension of this model was used to develop an amplitude equation that accounts for the

dynamics of twisted rods. This analysis was found useful in describing the evolution of climbing plants and the self-assembly of bacterial filaments.

1.2.2 Fluid supported sheet

In this section we utilize the formulation derived above to study the behavior of a thin sheet that is lying on a fluid substrate. Experimentally controlled systems that not just have a certain pattern but also exhibit transitions between several patterns are of special interest. Recent studies have shown that thin elastic sheets that lie on a liquid or an elastic foundation exhibit such a behavior. These systems are known by the name of “floating elastica” [39–48].

Much attention was paid to a special experimental configuration in which the floating sheet is uniaxially compressed from the boundaries. This configuration allows one-dimensional treatment and a relatively simple experimental setup. For example, an experimental study by Pociavsek *et al* [39] placed a polyester thin film on a water substrate and applied a compression force, P , from the boundaries (also equivalent to a controlled boundary displacement, Δ). The results show two critical transitions as a function of pressure or displacement. The first is from a flat state to a state of uniform sinusoidal undulations, termed “wrinkles” [7], and the second transition is from the extended wrinkles to a localized pattern termed “fold” [41], see Fig. 1.4.

Theoretically, the system was modeled by an energy functional that includes three terms: the bending energy, E_b , and two external forces - the hydrostatic pressure of the underlying liquid and the uniaxial compressive force, P . Following the formulation in the previous section, Eq. (1.9), and neglecting extensibility effects (setting $\gamma = 1$), the energy functional of the floating sheet was given by,

$$E = \frac{B}{2} \int_0^L \dot{\phi}^2 ds + W_{ext} = \frac{B}{2} \int_0^L \dot{\phi}^2 ds + \frac{\rho g}{2} \int_0^L h^2 \cos \phi ds - P\Delta, \quad (1.10)$$

where h is the sheet height ($dh/ds = \sin \phi$), ρ is the fluid density and g is the gravitational acceleration. In addition we have denoted $\dot{\phi} = d\phi/ds$. Applying dimensional analysis to this energy immediately reveals, in good agreement with experiments, the main features of the wrinkled state — the characteristic wavelength and the amplitude of the wrinkles are found to be $\lambda \sim (B/(\rho g))^{1/4}$ and $A \sim \lambda \sqrt{\Delta/L}$.

A more careful theoretical analysis is required in the folded state. In [49] it was shown using a variational Ansatz that the localized fold is energetically preferable over the extended wrinkles

starting from a critical displacement, $\Delta_W \propto 1/L$. To simplify the mathematical framework later studies took the sheet length to infinity ($L \rightarrow \infty$). Utilizing this assumption and using a multiple-scale approach, it was proven in Ref. [40] that the minimizing profile close to the transition coincides with the Ansatz of Ref. [49].

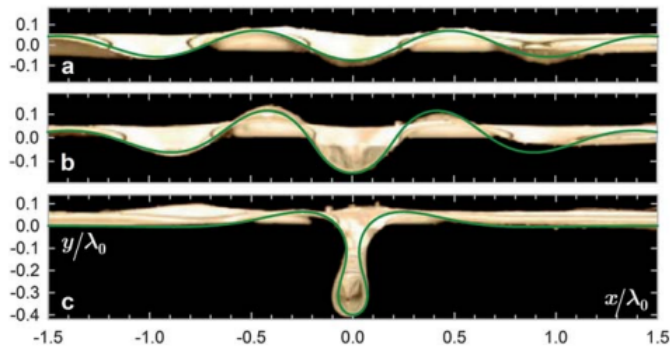


Figure 1.4: Three pictures from experiment placing a thin sheet on a fluid substrate [39, 43]. Increasing the boundary displacement transforms the system from a state of extended wrinkles (a) to a localized fold (c). Profile (b) is obtained close to the localization onset. The green curves that mimic the sheet configuration is the exact solution given in Eq. (1.12).

Subsequently, in Ref. [41] an exact solution was derived for this problem. In this study the energy functional, Eq. (1.10), was minimized to yield the following equilibrium equation²,

$$B\ddot{\phi} + B(\dot{\phi}^2/2 + P)\dot{\phi} + \rho gh = 0, \quad (1.11)$$

Then, by linking this equation to a known mathematical hierarchy of dynamical equations, its solution was related to the solution of a physical pendulum, a lower member of the hierarchy. The solution to Eq. (1.11) is a breather Sine-Gordon wave which is given by,

$$\phi(s) = 4 \tan^{-1} \left[\frac{\kappa \sin(ks)}{k \cosh(\kappa s)} \right], \quad (1.12)$$

where k, κ are respectively the wrinkles wavenumber and profile decay parameter. Equation (1.12) is the solution for a symmetric fold as shown in Fig. 1.4; other exact solutions exist too [41]. Further study [44] exposed the additional symmetry underlying the integrability of this problem. It also allowed to obtain an analytic expression for the sheet's height configuration, which is found to be in a remarkable agreement with experiment (see Fig. 1.4) [43].

In Chapter 2 of this thesis we present an extension of the floating-elastica theory [41] to sheets of finite length L , accounting for the experimentally observed wrinkle-to-fold transition. We

²Alternatively it can be derived from Eq. (1.7) by setting $F = \rho gh$. This force accounts for the hydrostatic pressure of the fluid.

derive an exact solution for the periodic deformation in the wrinkled state, and an approximate solution for the localized, folded state. We find that a second-order transition between these two states occurs at a critical displacement, $\Delta_F = \lambda^2/L$.

1.2.3 Elastic-kinetic analogies

In this section the elastic formulation that we have derived in Sec. 1.2.1 is utilized to study the analogy between thin filaments and the motion of rigid bodies. In some cases problems with no *a priori* link to elasticity turn out to be mathematically connected to it by the same formulation of the energy functional or equations of motion. For example, a ball constrained to roll without slip while sandwiched between two plates [50], turns out to follow the curves of the Euler elastica. Laplace connected the elastica to capillarity, identifying that the profile of a fluid surface between two vertical planes satisfies its equilibrium equation [51].

Another example is known by the name of *Kirchhoff's kinetic analogy*. Kirchhoff showed that the equations of motion of a 3D rigid body, fixed at a point and free to rotate under the influence of an external torque, are mathematically equivalent to the equilibrium equations of a spatial inextensible elastic filament that is confined by external forces on its edges [22, 52]. When the filament is further confined to a plane its equilibrium equation becomes equivalent to the equation of motion of a physical pendulum.

The latter lower-dimensional analogy can directly be shown from the formulation in Sec. 1.2.1. Setting $\gamma = 1$ in Eqs. (1.6) and (1.8), the equilibrium equation in the normal direction reduces to,

$$B \frac{d^2 \phi}{ds^2} + p \sin(\phi + \phi_0) = 0, \quad (1.13)$$

where $p = \sqrt{p_x^2 + p_y^2}$ and $\phi_0 = \sin^{-1}(p_y/p)$. By a constant shift of the angle, $\phi \rightarrow \phi + \phi_0$, it is readily seen that Eq. (1.13) is mathematically equivalent to the equation of motion of a physical pendulum.

This equivalence led Love [22, p. 402] to sort the curves of elastica into three different groups, in equivalence with the different trajectories of the pendulum: (i) Inflexional curves (inflexions are points of vanishing curvature) are analogous to an oscillating pendulum. (ii) Noninflexional curves are analogous to a revolving pendulum. (iii) An aperiodic curve is analogous to a pendulum that starts its motion at the unstable vertical point and ends up (after infinite time)

at the same position.

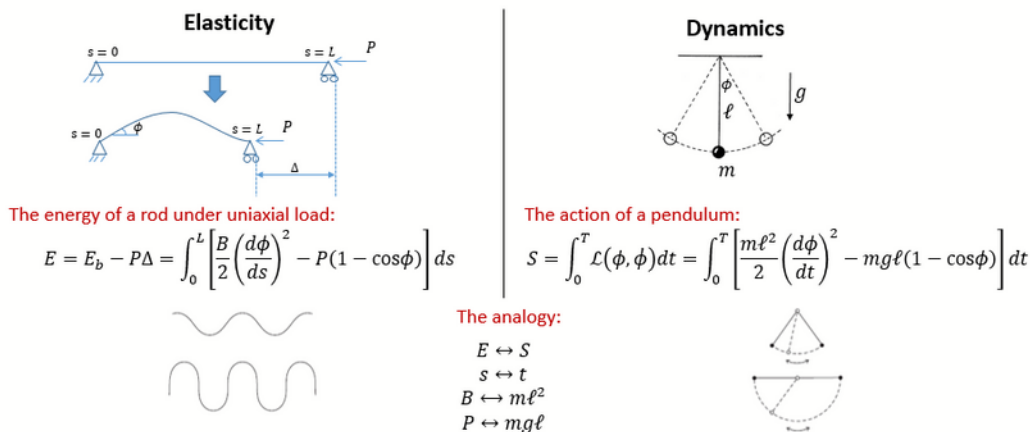


Figure 1.5: The analogy between a planar elastic filament and pendulum dynamics. The energy functional of an elastic filament confined by the force P (or displacement Δ), is a sum of the bending energy plus the external work, while the action of the pendulum is an integral over the Lagrangian, \mathcal{L} . Thus, within this analogy the energy is analogous to the action, arclength is analogous to time and the bending moment and the external force are respectively analogous to the moment of inertia and the external torque. The pendulum vs. elastica lines are taken from Ref. [53].

Although the two problems, elastica and pendulum, share an equivalent mathematical structure, and therefore have the same set of solutions, they also bear significant differences. One example that manifests this discrepancy is the buckling instability of a straight rod under uniaxial compression (Euler buckling). A straight rod that is subjected to a uniaxial load, P , buckles when the load exceeds a critical threshold, $P \geq P_{cr}$. Since a straight rod corresponds to a pendulum at rest and P is analogous to g (see Fig. 1.5), we are led to the *wrong* conclusion that for $g \geq g_{cr}$ a stationary pendulum will start swinging. The reason for this difference is that in elasticity we are given *boundary* conditions, whereas in the dynamic problem we are provided with *initial* conditions. The boundary conditions determine the periodicity which is independent of the external loads. Varying the force while keeping the periodicity fixed is the mechanism that leads to the buckling instability. By contrast, in the dynamic problem the initial conditions do not fix the period of motion.

Nevertheless, the kinetic analogue of the buckling instability can be viewed, to leading order, in the context of parametric resonance. A pendulum at rest whose pivot is subject to periodic oscillations with a finite frequency but vanishingly small amplitude, loses stability when its natural frequency becomes comparable to that of the oscillating pivot. Thus, at a

certain effective perpendicular acceleration, $g \geq g_{cr}$, the parametrically driven pendulum indeed becomes unstable, mimicking the buckling of an elastic rod for $P \geq P_{cr}$.

In all the examples given above the elastic body was assumed inextensible. In Chapter 3 we relax the inextensibility assumption in Kirchhoff's analogy and show that these corrections are mathematically equivalent to relativistic effects. We then utilize this analogy to derive an exact solution to the problem of a relativistic physical pendulum.

1.3 The elastic theory of two-dimensional thin sheets

The elastic theory of thin sheets in two dimensions is by far more complicated than the one-dimensional theory of uniaxially deformed sheets (Sec. 1.2.1). The scalars of stress (σ_{ss}), bending moment (M_{ss}), strain (ϵ_{ss}) and bending-strain (ϕ_{ss}) now become tensorial entities to account for the two in-plane directions on the sheet, $\alpha, \beta = 1, 2$. Thus, we have: (i) $\sigma_{\alpha\beta}$ - the stress tensor, (ii) $M_{\alpha\beta}$ - the torque tensor (stress couple), (iii) $\epsilon_{\alpha\beta}$ - the strain tensor, and (iv) $\phi_{\alpha\beta}$ - the bending strain tensor³.

Two equivalent approaches are used in the literature to derive the elastic theory of thin sheets. In the first approach the energy functional of the 3D body is reduced to 2D by direct integration over the thin dimension (dimensional reduction process, as in the Kirchhoff-Love scheme described in Sec. 1.1.2). Minimization of the resulting 2D energy with respect to spatial configurations of the sheet yields the equilibrium equations. In the second approach the elastic body is considered as a 2D surface from the very beginning. Balancing the forces and torques on that surface and introducing their relations to the actual configuration (the constitutive relations) yield the equilibrium equations. In the following derivation we take the second approach, similar to our derivation in Sec. 1.2.1. The first approach will be further discussed in Chapter 4.

To derive the force and torque balance equations on an infinitesimal segment of the 2D surface [15, 18] we first define the co-moving coordinate system, $\{\hat{\mathbf{t}}_1, \hat{\mathbf{t}}_2, \hat{\mathbf{n}}\}$. Given the position vector from the origin to the mid-surface, $\mathbf{f}(x_1, x_2)$, the two in-plane vectors are given by $\hat{\mathbf{t}}_\alpha = \partial_\alpha \mathbf{f} / |\partial_\alpha \mathbf{f}|$ ($\alpha = 1, 2$) and $\hat{\mathbf{n}}$, the unit normal to these vectors. Second, we consider an infinitesimal patch of the surface whose borders lie along lines of constant coordinates and sum to zero the forces and torques that are applied on its edges. This gives the following equations

³The tensor $\phi_{\alpha\beta}$ is related in the literature to the curvature tensor [54].

of equilibrium [15],

$$0 = \partial_1 \mathbf{F}_1 + \partial_2 \mathbf{F}_2 + |\partial_1 \mathbf{r} \times \partial_2 \mathbf{r}| \mathbf{P}, \quad (1.14a)$$

$$0 = \partial_1 \mathbf{M}_1 + \partial_2 \mathbf{M}_2 - \partial_1 \mathbf{r} \times \mathbf{F}_1 - \partial_2 \mathbf{r} \times \mathbf{F}_2, \quad (1.14b)$$

where \mathbf{F}_α and \mathbf{M}_α are force and torque vectors per undeformed unit length along lines of coordinates, x_α . In addition, an external body force per unit area in the normal direction is assumed, $\mathbf{P} = P \hat{\mathbf{n}}$. Lastly, we resolve the components of \mathbf{F}_α and \mathbf{M}_α along the triad basis,

$$\mathbf{F}_\alpha = \sigma_{1\alpha} \hat{\mathbf{t}}_1 + \sigma_{2\alpha} \hat{\mathbf{t}}_2 + \sigma_{3\alpha} \hat{\mathbf{n}}, \quad (1.15a)$$

$$\mathbf{M}_\alpha = \hat{\mathbf{n}} \times (M_{1\alpha} \hat{\mathbf{t}}_1 + M_{2\alpha} \hat{\mathbf{t}}_2). \quad (1.15b)$$

Equations (1.14) form a system of five differential equations (three from balance of forces and two from balance of torques) for eleven unknowns (five stresses, three torques and three unknowns that are related to the spatial configuration). Thus, to close the system we must derive constitutive relations between the force and torque components and the actual deformation (the components of the vector $\mathbf{f}(x_1, x_2)$).

Since these constitutive relations are material-dependent they can, in general, take many different forms, $\sigma_{\alpha\beta} = \sigma_{\alpha\beta}(\epsilon_{\alpha\beta}, \phi_{\alpha\beta})$ and $M_{\alpha\beta} = M_{\alpha\beta}(\epsilon_{\alpha\beta}, \phi_{\alpha\beta})$. It is also important to note that unlike the 1D case, Eqs. (1.6), we are no longer privileged to keep the bending and stretching deformations independent since the sheet may include Gaussian curvature. This curvature inevitably couples in-plane strains to out-of-plane deformations [20]. Thus, the in-plane stresses are expected to be functions of the out-of-plane strains and vice-versa. In the next subsection we will introduce the constitutive relations of 2D sheets in the special case of the small slope approximation.

Regardless of the constitutive laws, the total elastic energy that is stored in the sheet, i.e., the one required to deform the sheet from its rest state, is necessarily generalized from Eq. (1.9) to be,

$$E_{2D} = E_s + E_b = \frac{1}{2} \int_{\mathcal{A}} [\sigma_{\alpha\beta} \epsilon_{\alpha\beta} + M_{\alpha\beta} \phi_{\alpha\beta}] dx_1 dx_2 + W_{ext}, \quad (1.16)$$

where the first two terms are respectively the stretching and bending contributions and the last term is, again, the work of the external forces.

1.3.1 The Föpple-von Kármán model

The first systematic model that describes large deflections of thin sheets was derived by A. Föppl [55] and T. von-Kármán [56] and is called either the FvK model or the small slope approximation. Many experimentally observed patterns on thin sheets have been explained based on this model. However, before we review them let us derive its governing equations directly from Eqs. (1.14).

Specializing our derivations to Cartesian coordinates, $\{x_1, x_2\} \rightarrow \{x, y\}$, and to the Monge representation, the deformed configuration is given by,

$$\mathbf{r}(x, y) = \mathbf{r}_0(x, y) + \mathbf{u}(x, y) = [x + u_x(x, y)]\hat{\mathbf{x}} + [y + u_y(x, y)]\hat{\mathbf{y}} + \zeta(x, y)\hat{\mathbf{z}}, \quad (1.17a)$$

where $\mathbf{r}_0 = (x, y, 0)$ is the position vector to the flat undeformed surface, and $\mathbf{u}(x, y)$ is the displacement vector. Assuming that $\zeta \gg u_x, u_y$ and keeping only leading orders in these displacements, the linear extension of line elements (in-plane strains) and curvatures (out-of-plane “bending-strains”) are given by,

$$\epsilon_{\alpha\beta} = \frac{1}{2} (\partial_\alpha u_\beta + \partial_\beta u_\alpha + \partial_\alpha \zeta \partial_\beta \zeta), \quad (1.18a)$$

$$\phi_{\alpha\beta} = \partial_{\alpha\beta} \zeta. \quad (1.18b)$$

Furthermore, specializing to homogenous and isotropic materials and assuming linear stress-strain constitutive relations,

$$\sigma_{\alpha\beta} = Y [(1 - \nu)\epsilon_{\alpha\beta} + \nu\epsilon_{\gamma\gamma}\delta_{\alpha\beta}], \quad (1.19a)$$

$$M_{\alpha\beta} = B [(1 - \nu)\phi_{\alpha\beta} + \nu\phi_{\gamma\gamma}\delta_{\alpha\beta}], \quad (1.19b)$$

it can be shown that the force and torque balance equations, Eqs. (1.14), reduce to,

$$\partial_\alpha \sigma_{\alpha\beta} = 0, \quad (1.20a)$$

$$B(\partial_{xx} + \partial_{yy})^2 \zeta - \sigma_{\alpha\beta} \phi_{\alpha\beta} = P. \quad (1.20b)$$

These equations along with the constitutive relations, Eqs. (1.19) and (1.18), form a system of three equations for the three unknown components of the displacement, u_x, u_y and ζ . Lastly, following Eq. (1.16) the elastic energy that is stored in the deformed surface is given by [19, p. 52],

$$E_{\text{FvK}} = \frac{Y}{2} \int_{\mathcal{A}} [(\text{tr}\epsilon)^2 + 2(1 - \nu)\text{det}\epsilon] dx dy + \frac{B}{2} \int_{\mathcal{A}} [(\text{tr}\phi)^2 + 2(1 - \nu)\text{det}\phi] dx dy. \quad (1.21)$$

Many patterns have been explained based on these equations. Here are several examples. In Ref. [57] the FvK equations were used to determine the stability of a straight delamination blister, namely, predicting the critical buckling force and the corresponding emergent wavelength. Numerical analysis, based on the FvK functional, reveals to a remarkable accuracy the patterns of fingerprints [58]. Thin elastic bodies undergoing growth, morphogenesis, were shown to obey a generalized FvK model [59]. In Ref. [60] the FvK equations were used to study the dynamics of cracks in thin sheets. In this work a criterion for the path selection of the propagating crack was invoked and compared with experimental results. In Ref. [54] ridge singularities were analyzed based on the FvK model. Scaling laws for the radius of curvature with the thickness were obtained. In Ref. [61] the onset of a ruck in a rug was shown to be an effect of finite stretching energy in the FvK limit.

The FvK equations are qualified as well to describe the post-buckling behavior of ultra-thin sheets far from the threshold of instability. Such a theoretical description was presented by Davidovitch *et al.* for the Lamé configuration [11, 12]. In this problem a thin annulus is differentially stretched by radial forces from the inner and outer radii, see Fig. 1.6a. Based on the FvK equations two dimensionless parameters are defined: one is the *bendability* which is inversely proportional to the bending modulus, and the other is the *confinement* which depends on the ratio between the inner and outer tensile loads. For a given bendability and at a critical confinement wrinkles appear around the inner radius. These wrinkles grow vertically and radially towards the outer radius with increasing confinement.

In these studies it was shown that a naïve perturbative expansion of the height function about the flat configuration (near-threshold analysis) becomes invalid in the limit of vanishing thickness. A singular perturbation method (far-from-threshold analysis) that assumes vanishing hoop stresses ($\sigma_{\theta\theta} = 0$) above the flat-to-wrinkles transition was used to fit the theory to the experimental observations. For example, this assumption leads to experimentally consistent scaling laws for the number of wrinkles with the thickness. This approach has been successfully used to explain other experimentally observed patterns, e.g., in a sheet on a drop (Fig. 1.6c) [62] and in point indentation of a pressurized shell (Fig. 1.6b) [63, 64].

In Ref. [65] a flat elastic ribbon, subjected to a twist, η , and tension, T , was experimentally investigated. Under different combinations of the two control parameters, six different morphologies were observed, see Fig. 1.7. A theoretical study that followed this experiment used an extension of the FvK model to patterns that cannot be described by the Monge representation

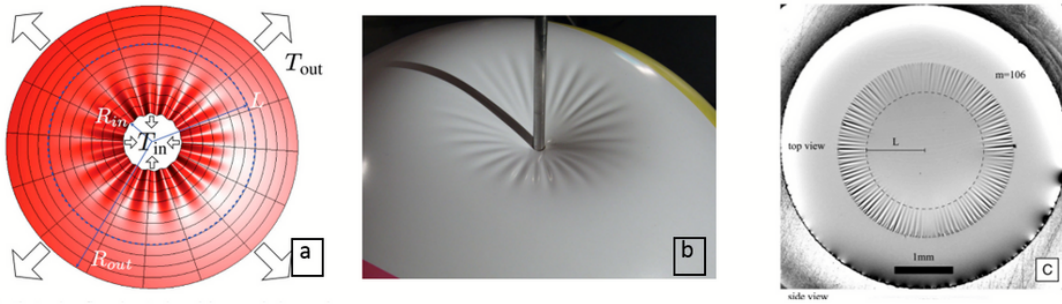


Figure 1.6: (a) Lamé configuration [11]. Thin annulus, radially stretched from the boundaries, reveals wrinkles close to the inner radius. (b) Point loading of an internally pressurized elastic shell presents a wrinkling instability [63]. (c) Placing a flat sheet on a spherical liquid drop creates wrinkles [62].

to analyze the transitions between the different patterns [66]. Another study that used this extension was introduced in [67] to describe the creation of a singular stress point which is related to the phenomenon of crumpled paper [14].

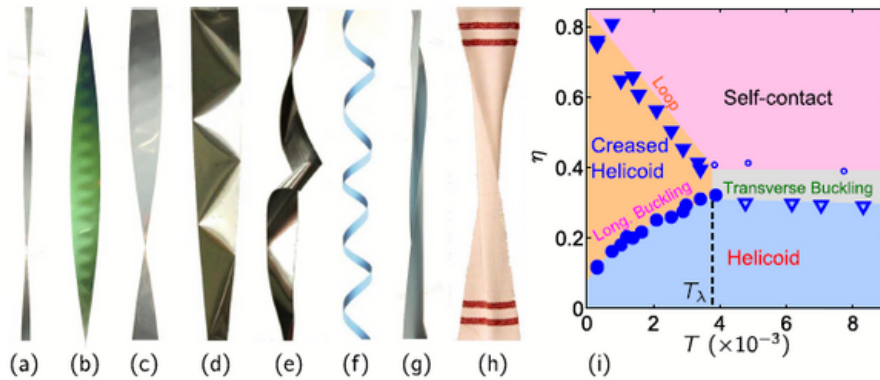


Figure 1.7: Different resulting morphologies of ribbons that are subjected to twist and stretching [65, 66]. These patterns are named as follows: (a) helicoid, (b,c) longitudinal wrinkled helicoid, (d) creased helicoid, (e) formation of loops and self-contact zones, (f) cylindrical wrapping, (g) transverse buckling, and (h) twist and transverse wrinkling. (i) Phase diagram on a twist-tension plane.

1.3.2 The elastic theory of thin incompatible sheets

Thin elastic sheets that include internal residual stresses even in the absence of external forces are named *incompatible sheets*. To mathematically explain the notion of incompatibility we

recall that in differential geometry a surface is characterized by its first ($a_{\alpha\beta}$) and second ($b_{\alpha\beta}$) fundamental forms [20],

$$a_{\alpha\beta} = \partial_\alpha \mathbf{f} \cdot \partial_\beta \mathbf{f}, \quad (1.22a)$$

$$b_{\alpha\beta} = \partial_{\alpha\beta} \mathbf{f} \cdot \hat{\mathbf{n}}, \quad (1.22b)$$

where $\mathbf{f}(x_1, x_2)$ as in Sec. 1.1.2 and 1.3 is the position vector defining the spatial configuration of the surface. While the first fundamental form, also called the metric tensor, is used to describe intrinsic properties of the surface, e.g., measuring length of line elements and areas, the second fundamental form is related to extrinsic properties such as the principal curvatures. However, not every $a_{\alpha\beta}$ and $b_{\alpha\beta}$ correspond to a physical surface that is embeddable in 3D. For the surface to be embeddable in 3D those tensors must satisfy a set of geometrical compatibility equations, known by the name of Gauss-Minardi-Patterson-Codazzi (GMPC) equations [20, p. 203].

When treating a thin solid sheet as a mathematical surface, its relaxed state is characterized by a 2D reference metric tensor, $\bar{g}_{\alpha\beta}$, and a reference second fundamental form, $\bar{b}_{\alpha\beta}$. When these tensors do not satisfy the GMPC equations, the equilibrium configuration is frustrated — its actual metric and second fundamental form, $a_{\alpha\beta}$ and $b_{\alpha\beta}$, will not coincide with their reference counterparts, leading to unavoidable intrinsic stresses.

For the sake of this thesis, let us specialize to plates (rather than shells) which are flat in their reference configuration, $\bar{b}_{\alpha\beta} = 0$. In these cases it is instructive to consider a surface constructed of a discrete lattice of springs (see Fig. 1.8a). If all the springs in the network can retain their rest lengths while being flat, the system is said to be compatible. If, however, some springs must be stretched (or compressed) to keep the network flat, the sheet is said to be incompatible. The latter case is likely to occur when the rest lengths of the springs depend on their positions, as in the specific example of Fig. 1.8b. In these cases, as we discuss below, it is energetically favorable to relax the stress in the springs by out-of-plane buckling.

In the continuous picture the reference metric, $\bar{g}_{\alpha\beta}$, coarse-grain the discrete rest lengths of the springs. In Fig. 1.8c and 1.8d we give one example for continuous incompatibility in the special case of an axisymmetric reference metric. In this case the reference metric fixes the rest length of concentric circles on a disc of radius R . If the rest lengths of the circles are different from $2\pi r$ the sheet is incompatible and internal strains must appear when the sheet remains planar.

In order to explain why in-plane frustration creates out-of-plane structures we first recall

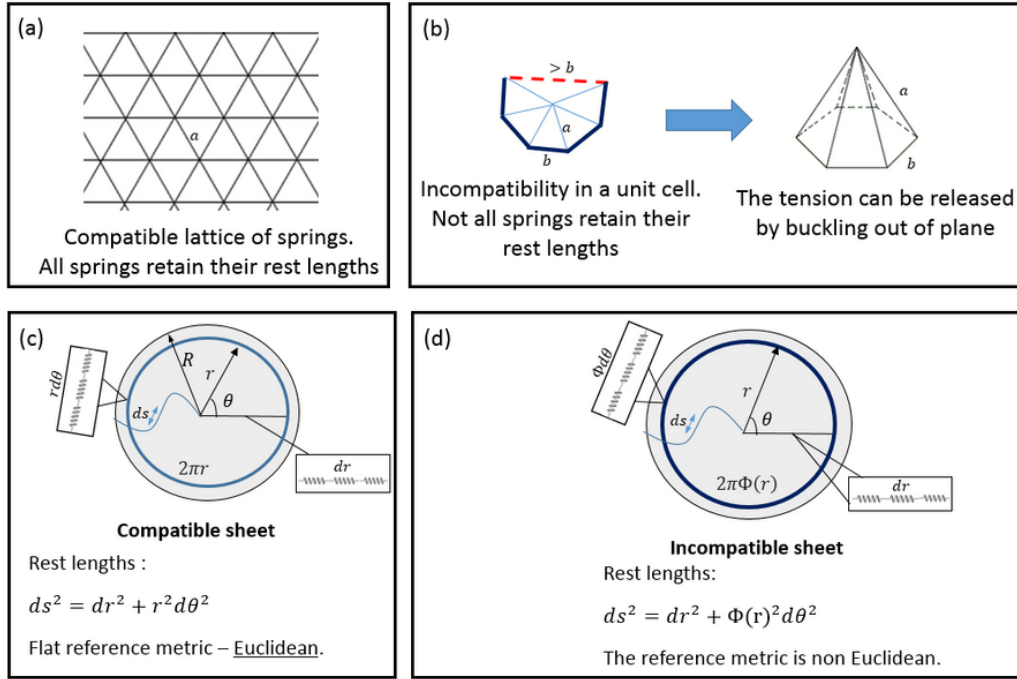


Figure 1.8: Demonstration of surface incompatibility through a discrete lattice of springs taken to the limit of continuous metric description. (a) A lattice of springs with rest length, a . Since all springs can retain their rest length while the network stays planar, the sheet is compatible. (b) Example of incompatibility in a unit cell. In this example the rest length of the azimuthal springs (thick lines) is b and the rest length of the radial springs is a . Under these conditions not all azimuthal springs can retain their rest length. As discussed in the text, in these cases it is sometimes energetically favorable to release the in-plane tension by out-of-plane buckling. (c) Compatible disc of radius R . The rest length of concentric circles on the disc is $2\pi r$. Thus, the reference metric is flat (or Euclidean) — its Gaussian curvature is zero and the sheet is compatible. (d) Continuous incompatibility. The rest length of concentric circles on the disc is $2\pi\Phi(r) \neq 2\pi r$. When the disc is flat these circles are either stretched or compressed, depending on the function $\Phi(r)$. Thus, the reference metric is not flat (non-Euclidean) and has non-zero Gaussian curvature.

that the elastic energy may be written as the sum of the following bending and stretching contributions [68],

$$\text{Incompatible: } E_{2D} = E_s + E_b \propto t(a_{\alpha\beta} - \bar{g}_{\alpha\beta})^2 + t^3(b_{\alpha\beta})^2. \quad (1.23)$$

Thus, similar to compatible sheets the relative energetic cost for stretching is significantly increased as the thickness decreases. As a result the actual metric is forced to be equal to the reference metric. Gauss's Theorema Egregium states that $a_{\alpha\beta} \rightarrow \bar{g}_{\alpha\beta}$ only if $K_a \rightarrow K_{\bar{g}}$, where $K_{\bar{g}}$ and K_a are the Gaussian curvatures of the reference and actual configurations [20]. Thus, the

actual surface must buckle in order to accommodate the Gaussian curvature of the reference metric. This behavior of incompatible sheets has been observed experimentally [69–77]; see Fig. 1.9 for several examples.

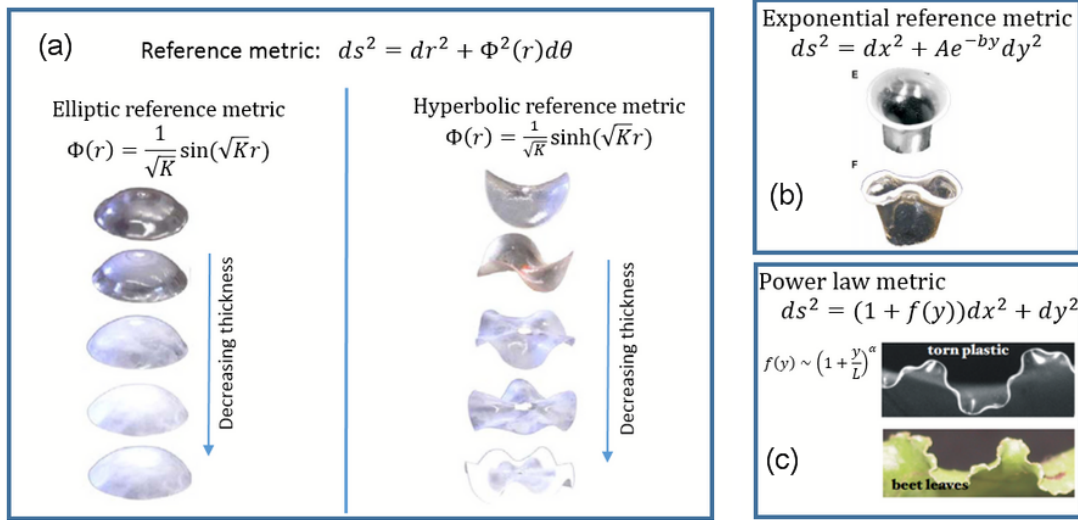


Figure 1.9: Experimental “programming” of incompatible sheets by Sharon *et al.* (a) NIPA hydrogels are programmed with axisymmetric reference metrics [75]. The rest length of concentric circles under an elliptic reference metric is $2\pi\Phi(r) < 2\pi r$. As the thickness is reduced the 3D configuration is converging towards a perfect spherical cap. For a hyperbolic reference metric we have $2\pi\Phi(r) > 2\pi r$ and when the thickness is reduced a series of wave bifurcations occur. (b) A tube with negative Gaussian curvature [70]. At a critical negative curvature the tube develops a wavy pattern on its edge. (c) Torn plastic sheet form a fractal configuration on its edge [76, 77]. Theoretically, this pattern is obtained by prescribing a metric that depends on a power law of r .

An elastic theory for incompatible thin sheets was proposed in Ref. [68] as an extension of Koiter’s plate theory [17]. Starting from the energy functional of a 3D elastic body, the Kirchhoff-Love hypothesis (see Sec. 1.1.2) was utilized to obtain the following 2D energy functional,

$$E_{2D} = E_s + E_b = \frac{t}{2} \int_{\mathcal{A}} A^{\alpha\beta\gamma\delta} \tilde{\epsilon}_{\alpha\beta} \tilde{\epsilon}_{\gamma\delta} \sqrt{g} dA + \frac{t^3}{24} \int_{\mathcal{A}} A^{\alpha\beta\gamma\delta} b_{\alpha\beta} b_{\gamma\delta} \sqrt{g} dA, \quad (1.24a)$$

$$\tilde{\epsilon}_{\alpha\beta} = \frac{1}{2}(a_{\alpha\beta} - \bar{g}_{\alpha\beta}), \quad (1.24b)$$

where $\tilde{\epsilon}_{\alpha\beta}$ is the two-dimensional strain tensor, as defined in this theory, and $A^{\alpha\beta\gamma\delta}$ is the elastic coefficient tensor. Minimization of this energy with respect to the three degrees of freedom of the displacement vector yields three force balance equations, two in-plane and one for the balance

of the out-of-plane forces.

This theory was successfully applied to several systems as we now review. In Ref. [78] the plane stress equation for incompatible sheets with axisymmetric reference metric was derived and numerically solved for three types of reference metrics: flat, elliptic and hyperbolic. This solution was then used to analyze the flat-to-buckle transition and to obtain the critical buckling thickness. In Ref. [79] equilibrium configurations of chiral ribbons were studied. Particularly the transition of a ribbon between twisted and helical configurations was quantitatively studied and compared to experimental results. A theoretical study that aimed to explain the wave refinement in a disc with negative Gaussian curvature (Fig. 1.9a) was introduced in [80, 81]. In this study the elastic energy, Eq. (1.24), was reduced to its FvK limit. Under this approximation it was shown that only two global minimizers exist, flat and saddle shape deformations with a localized region of stretching near the outer radius (boundary layer). This is in apparent contradiction with the increasing waviness shown in Fig. 1.9a (right), which has not been resolved to date. In Refs. [82, 83] the geometry of defects in amorphous materials was modeled using the abovementioned metric description. In Ref. [84] the properties of a frustrated ribbon spring were investigated. It was shown that, since the reference metric can be embedded as an isometric minimal surface (surface with no stretching and vanishing mean curvature), its bending and stretching energies vanish simultaneously, leading to a system that is controlled by delicate boundary effects. In Ref. [85] thermal fluctuations of geometrically frustrated elastic ribbons were studied. It was shown that statistical-mechanical properties of incompatible ribbons qualitatively differ from those of compatible ones.

In the present work, Chapter 4, we reconsider the formulation of incompatible thin sheets, Eq. (1.24), for a simple class of axisymmetric deformations. We show that the mathematical complexity of this theory is greatly reduced if the strain tensor, Eq. (1.24b), is redefined. Measuring strains based on deviations of line elements from their rest values, rather than distances squared (as in Eq. (1.24)), significantly simplifies the structure of the theory.

1.4 Outline of the Thesis

Following the structure of this Introduction the thesis is divided into two major parts. The first part consists of two projects concerning thin elastic sheets that deform uniaxially (without Gaussian curvature), and the second part is about configurations of thin incompatible sheets that in general can deform along the two in-plane directions.

1. Uniaxial deformations of thin sheets:

- (a) In Chapter 2 of this thesis we specialize to the problem of a sheet that is floating on a fluid substrate and uniaxially compressed from the boundaries (see Sec. 1.2.2 above). In particular, we extend the existing theory [41] to sheets of finite length. We utilize the new theory to obtain (i) exact solution to the wrinkled state, and (ii) approximate solutions to the folded state. Using the former result we obtain the pressure-displacement relation in the wrinkles regime and explore their amplitude growth as a function of the displacement. The latter solution for the folded state is used to analyze the details of the wrinkles-to-fold transition such as its order and characteristic exponents. Our analytical predictions are then compared with experimental results.
 - (b) In Chapter 3 we relax the inextensibility assumption in Kirchhoff's kinetic analogy and show that the resulting corrections in the elastic problem of uniaxial deformations are mathematically equivalent to relativistic effects in the dynamic system. We then take advantage of this result in two directions: (i) We identify a new symmetry of extensible elastic filaments, and (ii) we utilize the solution of extensible elastica to derive the exact solution for the motion of a relativistic physical pendulum.
2. In Chapter 4 we examine the effect of strain tensor selection on the theory of incompatible thin sheets. The existing theory uses the deviation of the surface metric from a reference metric to define the strain, Eq. (1.24). In the present work we define the strain based on a spring-like model that measures linear extension of line elements (rather than distances squared as in the metric description). We show that this replacement significantly reduces the mathematical complexity of the theory for a class of axisymmetric problems. Our theory yields linear, exactly solvable, equations of equilibrium in the case of planar deformations, replacing the non-linear ones derived earlier for these problems. In addition, we obtain a simple criterion determining whether an isometric immersion of such sheets

satisfies mechanical equilibrium.

Chapter 5 is dedicated to concluding remarks and the discussion of directions for future research in each of the projects addressed by the thesis.

The main chapters are supplemented by a series of Appendices at the end of the thesis, which elaborate on additional aspects of the projects.

Chapter 2

Wrinkles and folds in a fluid-supported sheet of finite size¹

2.1 Introduction

Morphological transitions are often induced by confinement or by spatially constrained growth. Structures emerge spontaneously when the energy injected into a system through the confinement process ceases to distribute uniformly. These phenomena are observed in various contexts ranging from the folding of geological layers [87] to patterns in biological membranes and monolayers [48, 88–92] and the formation of fingerprints [58, 93]. Besides the initial morphology, occurring for small confinement, various subsequent transitions may be observed as the confinement increases.

Many model systems have been developed to study the influence of confinement on morphological transitions [7, 94–99] using rods [100–102] or sheets resting on some substrate [42, 103–113]. Among them, the experimental model system of a thin elastic sheet, lying on a fluid substrate [45, 62, 114–121] and subjected to in-plane uniaxial compression, deserves special interest [39–41, 43, 44, 46, 47, 49], see also Sec. 1.2.2 in the Introduction. Beyond a certain critical confinement, Δ_W , which vanishes for an incompressible sheet, the sheet buckles, displaying regular undulations with a characteristic wavelength λ over its entire length [39, 48] (Fig. 2.1). Beyond a certain confinement, Δ_F , another transition occurs, where the wrinkles

¹The material presented in this Chapter was published in O. Oshri, F. Brau and H. Diamant, Phys. Rev. E **91**, 052408 (2015) [86]. This paper was selected as an Editor’s Suggestion.

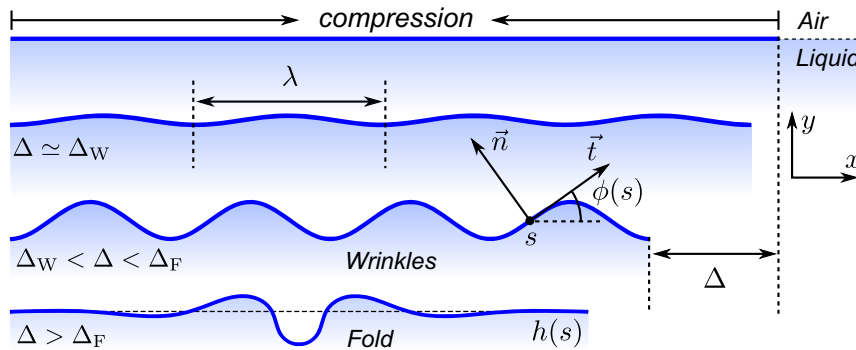


Figure 2.1: Schematic morphological evolution of a compressed finite sheet floating on a liquid. The scheme shows the emergence of a wavelength λ upon small confinement, $\Delta \gtrsim \Delta_W$, the growth in amplitude of the wrinkle state for intermediate compression, and the transition to a fold state beyond some critical confinement, Δ_F . Here \vec{t} and \vec{n} are the tangent and normal to the sheet surface, respectively. $\phi(s)$ is the angle between the local tangent and the horizontal direction x , and the arclength along the sheet is parametrized by s . $h(s)$ is the vertical elevation of the sheet.

start attenuating except near the center of the sheet, and the deformation energy gets localized into a single fold [39].

In the case of an infinitely long sheet, an exact solution describing the complete evolution of the morphology with increasing confinement proves that such a wrinkle-to-fold transition, strictly, should never occur [41], *i.e.* $\Delta_F \rightarrow \Delta_W$. The infinite-sheet morphology is always localized, but the localization decay length diverges as the buckling threshold Δ_W is approached.

Even if an infinitely long sheet is a useful idealization of real systems allowing a good agreement with experiment [43], the apparent discrepancy between theory and experiment concerning the existence of a wrinkle-to-fold transition should be resolved. Experiments are obviously performed with finite sheets. We demonstrate that a second-order wrinkle-to-fold transition does occur for finite sheets. In Sec. 2.3 we construct an exact periodic solution for wrinkles of arbitrary amplitude in a finite sheet. An exact solution for a localized deformation in a finite sheet has evaded us. Hence, in Sec. 2.4, we derive an approximate localized solution using a multiple-scale analysis. In Sec. 2.5, we identify the order parameter of the transition in the context of the Landau theory of second-order transitions. We show how both periodic and localized solutions match at the critical confinement, $\Delta_F = \lambda^2/L$, where λ is the wavelength of the wrinkles and L is the sheet length. In Sec. 2.6, we discuss the experimental implications of our theory, its limitations, and future extensions.

2.2 System and governing equation

The system studied here is composed of a thin incompressible elastic sheet ($\Delta_W = 0$) of length L , width W , and bending modulus B , lying on a fluid of mass density ρ . The sheet is uniaxially confined by a distance Δ along the x -axis and deforms in the xy plane. The shape of the sheet is described by the parametric equation

$$x(s) = \int_{-L/2}^s \cos \phi(s') ds', \quad (2.1a)$$

$$h(s) = \int_{-L/2}^s \sin \phi(s') ds', \quad (2.1b)$$

where $\phi(s)$ is the angle between the local tangent to the sheet and the x -axis at a given arclength s , see Fig. 2.1. The total energy of the system, E , is composed of the bending energy of the sheet, $E_b = (WB/2) \int_{-L/2}^{L/2} \dot{\phi}^2 ds$, and the deformation energy of the substrate, $E_s = (W\rho g/2) \int_{-L/2}^{L/2} h^2 \cos \phi ds$, where the dot denotes an s derivative [39, 41]. The displacement along the direction of confinement is given by

$$\Delta = \int_{-L/2}^{L/2} (1 - \cos \phi) ds, \quad (2.2)$$

and is related to the applied load necessary to confine the sheet by $P = dE/d\Delta$. In the following, except where it is explicitly mentioned, we use units such that the energy is rescaled by B , and lengths are rescaled by $(B/\rho g)^{1/4} \equiv \lambda/2\pi$. As a result, the applied load P is rescaled by $(B\rho g)^{1/2}$.

To find the equilibrium shape, one should minimize the total energy under appropriate constraints. This can be reformulated as a dynamical problem [41] with an action $\mathcal{S} = \int_{-L/2}^{L/2} \mathcal{L}(\phi, h, \dot{\phi}, \dot{h})$, where

$$\mathcal{L} = \frac{1}{2} \dot{\phi}^2 + \frac{1}{2} h^2 \cos \phi - P(1 - \cos \phi - \Delta/L) - Q(s)(\sin \phi - \dot{h}). \quad (2.3)$$

In Eq. (2.3), P and $Q(s)$ are Lagrange multipliers introduced to take into account, respectively, the global constraint (2.2) and the local geometrical constraint between h and ϕ . The conjugate momenta are defined as $p_\phi = \partial\mathcal{L}/\partial\dot{\phi} = \dot{\phi}$ and $p_h = \partial\mathcal{L}/\partial\dot{h} = Q$ and are used to construct the Hamiltonian $\mathcal{H} = p_\phi \dot{\phi} + p_h \dot{h} - \mathcal{L}$. Since \mathcal{L} has no explicit dependence on s , the Hamiltonian is a constant for a given displacement Δ ,

$$\mathcal{H} = \frac{1}{2} p_\phi^2 + p_h \sin \phi - \frac{1}{2} h^2 \cos \phi + P(1 - \cos \phi - \Delta/L) = C. \quad (2.4)$$

Hamilton's equation, $\dot{p}_\phi = -\partial\mathcal{H}/\partial\phi$, yields the following equation:

$$\ddot{\phi} + (h^2/2 + P) \sin \phi + p_h \cos \phi = 0. \quad (2.5)$$

Eliminating p_h between Eqs. (2.4) and (2.5), we obtain

$$\ddot{\phi} \sin \phi - \frac{1}{2} \dot{\phi}^2 \cos \phi + \frac{1}{2} h^2 + P - \tilde{P} \cos \phi = 0, \quad (2.6)$$

where $\tilde{P} \equiv P(1 - \Delta/L) - C$ is a shifted value of the load, dependent on boundary conditions. Differentiating Eq. (2.6) once, we obtain the well known equation for Euler's elastica (see also Sec. 1.2.1, Eq. 1.7),

$$\ddot{\phi} + \left(\frac{1}{2} \dot{\phi}^2 + \tilde{P} \right) \dot{\phi} + h = 0, \quad (2.7)$$

where the local normal force exerted on the elastica is given by the hydrostatic term h . A second differentiation gives the equation governing the system evolution,

$$\ddot{\phi} + \frac{3}{2} \dot{\phi}^2 \ddot{\phi} + \tilde{P} \ddot{\phi} + \sin \phi = 0. \quad (2.8)$$

Finally, Eq. (2.6) is used to relate the physical load P to the shifted value \tilde{P} . For hinged boundary conditions, where h and \ddot{h} (and also $\dot{\phi}$) vanish at the boundaries, we have

$$P = \tilde{P} \cos \phi(\pm L/2) - \ddot{\phi}(\pm L/2) \sin \phi(\pm L/2). \quad (2.9)$$

As a result, once the solution $\phi(s)$ is obtained, the physical load P can be computed from \tilde{P} . Note that in the limit of an infinite sheet, where $\phi(\pm L/2) \rightarrow 0$, P and \tilde{P} coincide.

The total rescaled energy per unit length of the system reads

$$E[\phi(s)] = \frac{1}{2} \int_{-L/2}^{L/2} ds \left(\dot{\phi}^2 + h^2 \cos \phi \right). \quad (2.10)$$

The energy, the displacement Δ and the equation giving the equilibrium shape of the sheet can also be written in terms of h instead of ϕ using $\dot{h} = \sin \phi$:

$$E[h(s)] = \frac{1}{2} \int_{-L/2}^{L/2} ds \left(\frac{\dot{h}^2}{1 - \dot{h}^2} + h^2 \sqrt{1 - \dot{h}^2} \right), \quad (2.11)$$

$$\Delta[h(s)] = \int_{-L/2}^{L/2} ds \left(1 - \sqrt{1 - \dot{h}^2} \right). \quad (2.12)$$

The shape of the sheet is determined from minimization of either E , given the displacement Δ , or the function,

$$G = E - P\Delta, \quad (2.13)$$

given the load P .

2.3 Exact periodic solutions

2.3.1 General results

We first study general solutions of Eq. (2.8) without specifying the boundary conditions. In order to construct a periodic solution of Eq. (2.8), we recall the connection existing between this equation and the dynamics of a physical pendulum [41, 122]. For this purpose, we consider the total energy U_p of a pendulum,

$$U_p \equiv 2k^2 q^2 = \frac{\dot{\phi}^2}{2} + q^2(1 - \cos \phi), \quad (2.14)$$

where q is the natural frequency of the pendulum, and k is a constant determined by the pendulum's total energy or, equivalently, by boundary conditions. (In the analogous elastic sheet these two parameters are related to the natural wrinkling wavenumber, $2\pi/\lambda$, and the total displacement Δ .) The equation of motion is obtained by taking the variation of U_p in the above equation,

$$\ddot{\phi} + q^2 \sin \phi = 0. \quad (2.15)$$

Differentiating twice this last equation and eliminating $q^2 \cos \phi$ and $q^2 \sin \phi$ using respectively Eqs. (2.14) and (2.15), we obtain

$$\ddot{\phi} + \frac{3}{2} \dot{\phi}^2 \ddot{\phi} + (1 - 2k^2) q^2 \ddot{\phi} = 0. \quad (2.16)$$

Adding Eq. (2.15) multiplied by q^{-2} , we finally obtain the equation describing the morphology of a confined floating sheet, see Eq. (2.8):

$$\ddot{\phi} + \frac{3}{2} \dot{\phi}^2 \ddot{\phi} + \tilde{P} \ddot{\phi} + \sin \phi = 0, \quad (2.17a)$$

$$\tilde{P} = q^2 (1 - 2k^2) + q^{-2}. \quad (2.17b)$$

Therefore, any solution of Eq. (2.15) is also a solution of Eq. (2.8) with \tilde{P} given by Eq. (2.17b).

It is well known that Eq. (2.15) admits a periodic solution for $0 \leq k < 1$ in terms of Jacobian elliptic functions [123, p.549],²:

$$\phi(s) = 2 \arcsin [k \operatorname{sn}(q(s + s_0), k)]. \quad (2.18)$$

The profile $h(s) = \int_{-L/2}^s \sin \phi(s') ds'$ is thus given by

$$h(s) = \frac{2k}{q} [\operatorname{cn}(q(s + s_0), k) - \operatorname{cn}(q(-L/2 + s_0), k)]. \quad (2.19)$$

²Note that there are two definitions for the modulus of the elliptic functions. In this section, we use the one given in Ref. [123]. The other one, $m = k^2$, is used in Ref. [124] and by *Mathematica*®.

This solution has a periodicity of $4K(k)/q$, where $K(x)$ is the complete elliptic integral of the first kind [123, p.487]. Finally, the horizontal displacement is given by

$$\Delta = 2k^2 \int_{-L/2}^{L/2} \text{sn}^2(q(s + s_0), k) ds = 2L - \frac{2}{q} \{\mathcal{E}(q(s + s_0), k)\}_{-L/2}^{L/2}, \quad (2.20)$$

where $\mathcal{E}(x, k)$ is the Jacobi epsilon function [123, p.562]. The quantities s_0 and q are fixed to satisfy the boundary conditions whereas the parameter k is related to the confinement ratio, Δ/L .

2.3.2 Hinged sheets

For hinged boundary conditions both h and \ddot{h} vanish at $s = \pm L/2$. The second derivative of the sheet profile, Eq. (2.19), is given by

$$\ddot{h}(s) = 2kq \text{cn}(q(s + s_0), k) (2 \text{dn}^2(q(s + s_0), k) - 1). \quad (2.21)$$

The dn function varies between $(1 - k^2)^{1/2}$ and 1; consequently, so long as $k < 1/\sqrt{2}$, the last factor in Eq. (2.21) does not vanish. As shown below, the relevant values of k are smaller than $1/3$ provided $L \geq 3\lambda$. Larger values of k lead to periodic solutions unstable against localization.

Due to the periodicity of the solution, there exists an infinite number of possible solutions depending on the number of nodes. From Eq. (2.19), $h(L/2) = 0$ provided that $qL/2 + qs_0 = -qL/2 + qs_0 + 4n_1K(k)$. From Eq. (2.21), $\ddot{h}(L/2) = 0$ provided that $qL/2 + qs_0 = (2n_2 + 1)K(k)$, with n_1 and n_2 positive integers. Due to the definite parity of the solution (either symmetric or antisymmetric), the condition $\ddot{h}(-L/2) = 0$ is then automatically satisfied. We have the following two possibilities. (a) If $s_0 = 0$, then $h(L/2) = 0$ automatically, for any q , due to the even parity of the cn function in Eq. (2.19). We are left with the condition for $\ddot{h}(L/2) = 0$ which gives $qL = 2(2n_2 + 1)K(k)$. (b) If $s_0 \neq 0$, then the two conditions above must be satisfied simultaneously, giving $qL = 4n_1K(k)$ and $qs_0 = [2(n_2 - n_1) + 1]K(k)$. Thus, combining these two results, we have

$$q = \frac{2(2p + 1)K(k)}{L} \quad \text{with } s_0 = 0 \quad (2.22)$$

$$q = \frac{2(2p)K(k)}{L} \quad \text{with } qs_0 = K(k), \quad (2.23)$$

where p is a strictly positive integer. Finally, the solution reads

$$\phi(s) = 2 \arcsin [k \text{sn}(qs + \varepsilon K(k), k)], \quad (2.24a)$$

$$h(s) = \frac{2k}{q} \text{cn}(qs + \varepsilon K(k), k), \quad (2.24b)$$

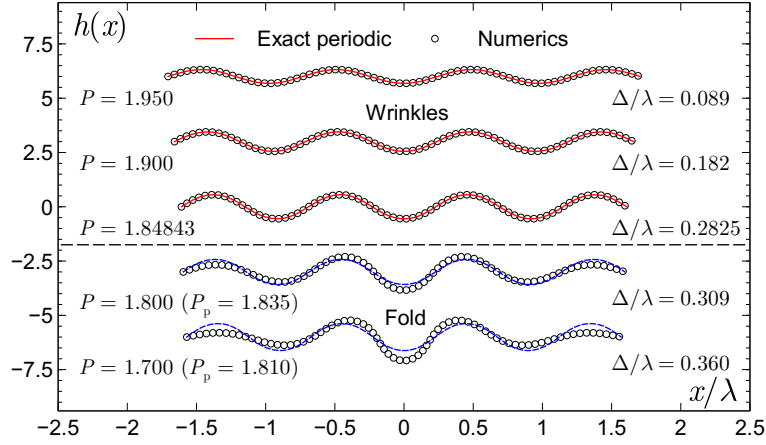


Figure 2.2: Evolution of the exact periodic solution for different values of Δ/λ and $L/\lambda = 3.5$ ($N = 7$), where $x(s)$, $h(s)$ are given by Eqs. (2.1a) and (2.24b) respectively and $\phi(s)$ is given by Eq. (2.24a). The corresponding evolution for the numerical solution of Eq. (2.8) is also shown. P and P_p correspond to the numerical and the periodic solutions respectively ($P = P_p$ for $\Delta/\lambda \leq 0.2825$). The wrinkle-to-fold transition occurs at $\Delta/\lambda \simeq 0.2825$.

where $\varepsilon = (1 + (-1)^n)/2$ and

$$q = \frac{2nK(k)}{L}, \quad n = 1, 2, 3 \dots \quad (2.25)$$

Symmetric solutions correspond to n of odd parity and antisymmetric solutions are obtained with an even parity of n . The number of nodes of the solution is equal to $n + 1$ (counting the two nodes at the boundaries).

2.3.3 Pressure, displacement, and amplitude

From Eq. (2.24a), we have

$$\begin{aligned} \cos \phi(L/2) &= 1 - 2k^2, & \ddot{\phi}(L/2) &= \mp 2kq^2 \sqrt{1 - k^2} \\ \sin \phi(L/2) &= \pm 2k \sqrt{1 - k^2}. \end{aligned} \quad (2.26)$$

The expression for the applied load is then obtained from Eq. (2.9) together with Eq. (2.17b):

$$P = q^2 + (1 - 2k^2)q^{-2}. \quad (2.27)$$

From this infinity of possible solutions for a given value of L , only the one minimizing P is selected, which fixes the value of n ; see below.

The parameter k is related to the confinement Δ by using Eq. (2.20):

$$\Delta = 2L - \frac{2}{q} [\mathcal{E}((n + \varepsilon)K, k) + \mathcal{E}((n - \varepsilon)K, k)], \quad (2.28)$$

where we used the expression (2.25) for q , $qs_0 = \varepsilon K(k)$, and the fact that \mathcal{E} is an odd function.

When $n = 2p + 1$ such that $\varepsilon = 0$, we obtain

$$\begin{aligned}\Delta &= 2L - \frac{4}{q}\mathcal{E}((2p+1)K, k) = 2L - \frac{4}{q}(2p+1)E(k) \\ &= 2L \left(1 - \frac{E(k)}{K(k)}\right),\end{aligned}\tag{2.29}$$

where $E(k)$ is the complete elliptic integral of the second kind [123, p.487]. When $n = 2p$ such that $\varepsilon = 1$, we have

$$\Delta = 2L - \frac{2}{q}[\mathcal{E}((2p+1)K, k) + \mathcal{E}(2p-1)K, k)]\tag{2.30}$$

$$= 2L - \frac{8p}{q}E(k) = 2L \left(1 - \frac{E(k)}{K(k)}\right).\tag{2.31}$$

Therefore, the relation between k and Δ is the same for symmetric and antisymmetric solutions. The decrease of the applied pressure P as a function of the confinement Δ is given by the parametric equation $(\Delta(k), P(k))$ given by Eqs. (2.27) and (2.31) and using Eq. (2.25).

However, we still have to determine the optimal value of n minimizing P . For $L = N\pi$ ($L/\lambda = N/2$), it can be shown that $n = N$ provided k is small enough. Above some threshold, $k = k^*$, we have $n = N - 1$. As $\Delta(k)$ is an increasing function of k [Eq. (2.31)] this means that for small confinement we have $n = N$ before reaching a threshold, $\Delta(k^*)$, above which the compressed system prefers to remove half a wavelength from the profile, $n = N - 1$. However, if $\Delta(k^*) \geq \Delta_F$, where Δ_F is the critical confinement for which the periodic solution is unstable against the localized solution, then $n = N$ for all the values of confinement where the periodic solution is stable. The threshold k^* can be obtained by searching for which value of k , the pressure P has the same value for $n = N$ and $n = N - 1$. We found that $\Delta(k^*)/L \simeq (k^*)^2 = 2\pi/3L = \lambda/3L$, where we used a first order expansion for the confinement which is enough for this discussion (using the full expression leads to the same conclusion). Comparison with $\Delta_F/L = \lambda^2/L^2$, which is derived in the next section, shows that for $L \geq 3\lambda$ the optimal value of n is always $n = N$ (with $L = N\pi$). Notice that it leads also to $k \leq 1/3$. From now on, we assume that the length of the sheet is at least as large as three times the wrinkle wavelength. As a result, when N is odd, the solution is symmetric and when N is even, it is antisymmetric. For $L = N\pi$, we thus have $n = N$ and the expression for the pressure reads

$$P = \frac{4}{\pi^2}K(k)^2 + \frac{\pi^2(1-2k^2)}{4K(k)^2}.\tag{2.32}$$

Let us summarize the scheme for calculating the exact periodic solution. Given $L = N\pi$, we have $n = N$. Given Δ/L we find k from Eq. (2.31). The values obtained for n and k are

substituted in Eq. (2.25) to obtain q . These values of k and q are used in Eqs. (2.24b) and (2.27) to obtain the height profile and the pressure. This solution is unique thanks to the monotonic-increasing nature of the right-hand-side of Eq. (2.31). Finally, the pressure-displacement relation is obtained parametrically from Eqs. (2.31) and (2.32); see Fig. 2.4. Figure 2.2 shows the evolution with increasing confinement of the exact periodic solution for $L = 7\pi$ ($L/\lambda = 3.5$) comparing it to the numerical solution of Eq. (2.8). For $\Delta/\lambda \lesssim 0.2825$, the numerical solution is periodic. This threshold is close to the critical wrinkle-to-fold confinement computed in Section 2.4 for large sheets, $\Delta_F/\lambda = 0.2857$.

Since it is expected that this exact periodic solution is unstable against localization for large enough confinement, we give below its expansion for small Δ . We expand Eqs. (2.31) and (2.32) in small k to obtain $\Delta = Lk^2 + \mathcal{O}(k^4)$ and $P = 2 - 2k^2 + \mathcal{O}(k^4)$. Thus, to leading order in small relative confinement, we have

$$P \simeq 2 \left(1 - \frac{\Delta}{L} \right). \quad (2.33)$$

The amplitude of the profile is $A = 2k/q$ (see Eq. (2.24b)). For $L = N\pi$, we have

$$A = \frac{\pi k}{K(k)} \simeq 2\sqrt{\frac{\Delta}{L}}. \quad (2.34)$$

The corresponding profiles for small confinement are

$$h(s) = A \cos s, \quad \text{symmetric profile}, \quad (2.35a)$$

$$h(s) = A \sin s, \quad \text{asymmetric profile}. \quad (2.35b)$$

Thus, to leading order in Δ/L , our exact solution reproduces the expressions for P , A , and $h(s)$, known for the wrinkle state [42, 48, 91, 94]. Notice that, because we consider $L \geq 3\lambda$, and a transition to the localized solution occurs for $\Delta/L = \lambda^2/L^2$, the maximum relative compression relevant for the periodic solution is $\Delta/L \leq 1/9 \simeq 0.11$, which is indeed small. Therefore, a first-order expansion is quite sufficient for describing the wrinkle state.

2.4 Approximate localized solutions

2.4.1 Construction of the localized solution

We have not been able to find exact physical solutions for folds in a finite sheet. Exact localized solutions of Eq. (2.8) for a finite sheet do exist; yet, these profiles are not solutions of the

present physical problem, as they have a finite height at the boundaries. We describe them in Appendix A.1 for the sake of mathematical interest and possible relevance for other systems to be studied in the future.

We resort to a perturbative calculation, extending the multiple-scale analysis of Ref. [40] to a finite system. The main motivation is to enable an accurate analysis of the wrinkle-to-fold transition, as will be presented in Sec. 2.5. We therefore assume a very long (yet finite) sheet compared to the wrinkle wavelength, $L \gg \lambda$. It has been established that, as L is made larger, the region of stable wrinkles shrinks and their amplitude diminishes [40, 49]. Thus, the critical values of the pressure and displacement for the wrinkle-to-fold transition, P_F and Δ_F , can be assumed arbitrarily close to the ones for the flat-to-wrinkle transition, $P_W = 2$ and $\Delta_W = 0$, as L is taken to be arbitrarily large.

At the transition from a wrinkle state to a localized one, we anticipate that the undulations of wavelength λ will be attenuated over a much larger length scale of order L . Therefore, the sheet profile contains two length scales, a short one (λ) and a long one (L). To obtain this profile near the transition, we then substitute in the energy, Eqs. (2.11)-(2.13), a multiple-scale function of the form

$$h(s) = \cos(k_c s) \sum_{j=1}^{\infty} \epsilon^j H_j(\epsilon s) \simeq \epsilon \cos(k_c s) H_1(\epsilon s), \quad (2.36)$$

and consider hinged boundary conditions,

$$h(\pm L/2) = \ddot{h}(\pm L/2) = 0. \quad (2.37)$$

In this expansion, the small parameter ϵ is given by

$$\epsilon = (P_W - P)^{1/2}, \quad (2.38)$$

where $P_W = 2$ is the critical flat-to-wrinkle pressure. k_c is the wavenumber of the fast oscillations; from the known flat-to-wrinkle transition we expect to get $k_c = 1$ [39, 48]. We have selected a symmetric profile; an antisymmetric one is obtained by replacing the cosine with a sine and leads to a similar analysis. For simplicity, we restrict the discussion to commensurate sheets, $L = N\pi$ (*i.e.* $L/\lambda = N/2$), where odd and even N correspond respectively to symmetric and antisymmetric solutions. (We will later check the effect of this approximation numerically.)

As in Ref. [40], we substitute the profile Eq. (2.36) in Eq. (2.13), expand in powers of ϵ , and integrate over the fast oscillations (which cancel the terms proportional to ϵ and ϵ^3), to obtain

a systematic expansion of the energy,

$$G = G_0\epsilon^2 + G_1\epsilon^4 + \mathcal{O}(\epsilon^6), \quad (2.39)$$

Analysis of the leading order reproduces the known wrinkling transition with $P_W = 2$ and $k_c = 1$ ($\lambda = 2\pi$) without any constraint on H_1 . This gives $G_0 = 0$, reducing the energy of the system to $G = G_1\epsilon^4$. The function H_1 is determined by minimizing the functional G_1 , given by

$$G_1 \simeq \frac{1}{2} \int_{-L/2}^{L/2} \left([H_1'(S)]^2 - \frac{1}{16} H_1^4 + \frac{1}{4} H_1^2 \right) ds, \quad (2.40)$$

where $S \equiv \epsilon s$, and a prime denotes a derivative with respect to S . Variation of Eq. (2.40) gives the amplitude equation for H_1 [40],

$$H_1''(S) + \frac{1}{8} H_1^3 - \frac{1}{4} H_1 = 0. \quad (2.41)$$

The boundary conditions of vanishing height, $h(\pm L/2) = 0$, are automatically satisfied since $\cos((N/2)\pi) = 0$ for odd N . The boundary conditions of vanishing bending moment, $\ddot{h}(\pm L/2) = 0$, impose

$$H_1'(S = \pm \epsilon L/2) = 0. \quad (2.42)$$

Equations (2.41) and (2.42) always have the trivial constant solution, $H_1 = \sqrt{2}$, corresponding to wrinkles. In addition, Eq. (2.41) has solutions in terms of Jacobian elliptic functions [124]. Out of the twelve Jacobian functions, only one is found to provide a physical solution,³

$$H_1(S) = 4\kappa \operatorname{dn}(\kappa S, m), \quad \kappa = \frac{1}{2\sqrt{2-m}}. \quad (2.43)$$

In this section using the other definition of the modulus m [124] makes the presentation more elegant. It is related to the modulus k of Sec. 2.3 by $m = k^2$. The modulus m ($0 \leq m \leq 1$) changes with the displacement Δ (see Eq. (2.50) below). The pressure is also related to the modulus m using the boundary condition (2.42),⁴

$$\kappa\epsilon L = 2K(m), \quad (2.44)$$

where $K(m)$ is the complete elliptic integral of the first kind [124], which is half the period of the function dn [124], $\kappa(m)$ is defined in Eq. (2.43), and $\epsilon = \sqrt{2-P}$. Equations (2.36), (2.43)

³The Jacobian function dc yields a solution identical to Eq. (2.43). The function cn describes a solution whose amplitude *decreases* with increasing displacement. The remaining nine functions either diverge with increasing L and/or are odd, thus reversing the symmetry of the solution.

⁴We use here the envelope at its lowest mode (no nodes). Higher modes, satisfying $\kappa\epsilon L = 2nK(m)$ with $n > 1$, are valid solutions but with higher energy.

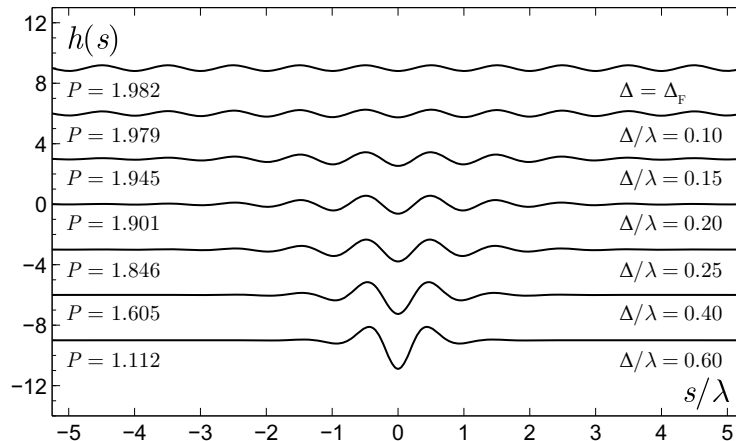


Figure 2.3: Localized height profiles for a sheet of length $L/\lambda = 10.5$ for various values of the confinement parameter.

and (2.44) yield the height profile, $h(s)$, of the sheet for a given m ,

$$h(s) = 4\kappa\epsilon \operatorname{dn}(\kappa\epsilon s, m) \cos(s), \quad (2.45a)$$

$$= \frac{8K(m)}{L} \operatorname{dn}\left(\frac{2K(m)}{L}s, m\right) \cos(s), \quad (2.45b)$$

for $L/\lambda = N/2$.

The resulting profiles are demonstrated in Fig. 2.3. In the limit $m \rightarrow 0$, the function $\operatorname{dn}(u, m) \rightarrow 1$, and from Eq. (2.45b) we recover the wrinkled profile, $h(s) = \sqrt{2}\epsilon \cos(s)$ [49]. In the opposite limit, $m \rightarrow 1$, we have $\operatorname{dn}(u, m) \rightarrow 1/\cosh(u)$, which recovers the approximate localized fold for an infinite sheet [40, 49], $h(s) = 2\epsilon \cos(s)/\cosh(\epsilon s/2)$. These two limits are further treated in Sec. 2.4.2. Thus, m serves as the order parameter of the wrinkle-to-fold transition, as will be discussed in Sec. 2.5. The antisymmetric counterpart of Eq. (2.45b) is obtained by replacing $\cos(s)$ with $\sin(s)$.

To further characterize the extent of localization, we define the decay length of the envelope as,

$$\xi \equiv \left| \frac{H_1(0)}{\ddot{H}_1(0)} \right|^{1/2} = \frac{L}{2\sqrt{m}K(m)}, \quad (2.46)$$

where the last equality follows from Eq. (2.45b). The decay length diverges ($\xi \rightarrow \infty$) when $m \rightarrow 0$, and vanishes ($\xi \rightarrow 0$) as $m \rightarrow 1$. This defines the two limits of weakly and strongly localized profiles to be discussed below. Note, however, that the leading order of the multiple-scale analysis is not strictly valid in the strongly localized limit. The crossover between these two limits, $\xi = L$, where the localization should become observable, occurs at $m \simeq 0.096$.

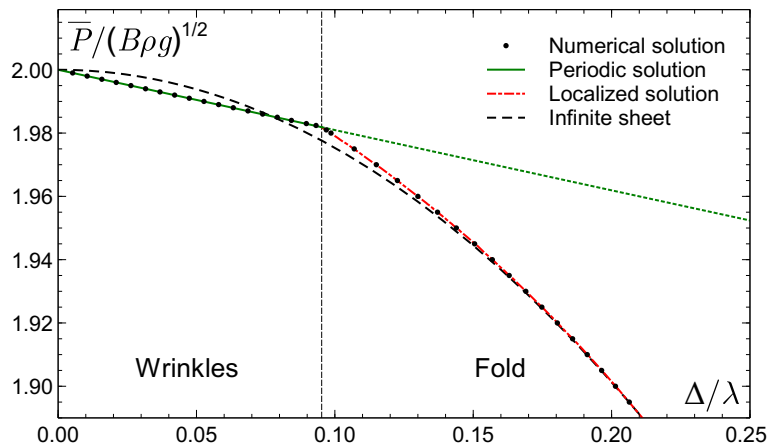


Figure 2.4: Pressure as a function of displacement for a sheet of length $L/\lambda = 10.5$, showing the second-order transition between the wrinkle state (exact solution, green solid line) and the fold state (multiple scale approximation, red dash-dotted line). \bar{P} is the physical dimensional pressure. Numerical solution (circles) of Eq. (2.8) indicates that the parametric equations (2.31) and (2.32) for the wrinkle state, and (2.47) and (2.50) for the fold state, provide the correct evolution of P as a function of Δ . The pressure-displacement relation for a confined infinite sheet, Eq. (2.58), is shown for comparison (exact solution, black dashed line).

2.4.2 Pressure, displacement, and amplitude

Using Eq. (2.44) together with Eq. (2.38), we obtain the expression for the pressure associated with the localized solution,

$$P(m) = 2 - \frac{16}{L^2}(2 - m)K(m)^2. \quad (2.47)$$

Since we know that for an infinite sheet the wrinkle state is always unstable against the localized state [40], we expect that this transition should occur at an arbitrarily small displacement for a sufficiently long sheet. Therefore, we expand the expression (2.12) of the displacement to the leading order in ϵ ,

$$\Delta \simeq \frac{1}{2} \int_{-L/2}^{L/2} ds \dot{h}^2. \quad (2.48)$$

Using the expression (2.45a) for h , averaging over the fast oscillations (short length scale), and performing the integral over the slow envelope (long length scale), we obtain

$$\Delta = 8\kappa\epsilon \mathcal{E}(\kappa\epsilon L/2, m), \quad (2.49)$$

where $\mathcal{E}(x, m)$ is the Jacobi epsilon function, and κ is given as a function of m in Eq. (2.43).

Using Eq. (2.44), the displacement associated with the localized solution reads,

$$\Delta(m) = 8\kappa\epsilon \mathcal{E}(K(m), m) = \frac{16}{L}K(m)E(m), \quad (2.50)$$

where $E(m)$ is the complete elliptic integral of the second kind [124]. Since both Δ , given by Eq. (2.50), and P , given by Eq. (2.47), are functions of m , the evolution of the pressure as a function of the displacement is given by the parametric form $(\Delta(m), P(m))$. This evolution is demonstrated in Fig. 2.4.

Weakly localized limit

As m grows from zero the profile ceases to be purely periodic and begins to localize. In the weakly localized limit, $m \ll 1$, the symmetry has already been broken, but the localization length is still larger than the system size, $\xi > L$. In this limit, therefore, the deviation from the wrinkle state will be hard to resolve experimentally. Nevertheless, as mentioned above, $m \simeq 0.1$ is sufficient to reach $\xi \simeq L$.

The displacement given by Eq. (2.50) is an increasing function of m . We notice that, in the limit $m \rightarrow 0$, the displacement takes a finite value,

$$\Delta_{\text{F}} \equiv \Delta(0) = 4\pi^2/L = \lambda^2/L. \quad (2.51)$$

This means that the localized solution emerges only beyond this finite displacement in the case of sheets of finite length. For a confinement smaller than Δ_{F} , the shape of the sheet is described by the periodic solution constructed in Sec. 2.3. In Appendix A.3 we obtain the critical wrinkle-to-fold confinement, up to a constant prefactor, $\Delta_{\text{F}} \sim \lambda^2/L$, from a simple scaling analysis.

For small m we have

$$\Delta(m) = \Delta_{\text{F}} + \frac{\pi^2 m^2}{8L} + \mathcal{O}(m^3), \quad (2.52)$$

$$P(m) = 2 - \frac{8\pi^2}{L^2} - \frac{3\pi^2 m^2}{4L^2} + \mathcal{O}(m^3). \quad (2.53)$$

The parameter m can be eliminated to obtain

$$P \simeq 2 - \frac{2\Delta_{\text{F}}}{L} - 6 \left(\frac{\Delta - \Delta_{\text{F}}}{L} \right). \quad (2.54)$$

The profile for $m = 0$ is obtained from Eq. (2.45b),

$$h(s) = \frac{4\pi}{L} \cos s, \quad m = 0. \quad (2.55)$$

Although this profile describes periodic wrinkles, it has a finite amplitude since it is obtained for a finite displacement, $\Delta = \Delta_{\text{F}}$.

Once $m > 0$, the profile is no longer periodic and its extrema have different heights. The height of the central fold, $A_0 = |h(0)|$, and that of the extremum next to it, $A_1 \simeq |h(\pi)|$, are of special interest since they are used to experimentally characterize the evolution of the localized profile [39]; see also Sec. 2.6 and Fig. 2.7. (The localization makes the second extremum shift slightly from $s = \pi$, but this shift is of higher order than our present approximation.) From Eqs. (2.45b) and (2.52) we get

$$A_0 \simeq \frac{4\pi}{L} + 2\sqrt{2} \left(\frac{\Delta - \Delta_F}{L} \right)^{1/2}, \quad (2.56a)$$

$$A_1 \simeq \frac{4\pi}{L} + 2\sqrt{2} \cos \left(\frac{2\pi^2}{L} \right) \left(\frac{\Delta - \Delta_F}{L} \right)^{1/2}, \quad (2.56b)$$

which are valid for $\Delta \gtrsim \Delta_F$. The slopes of both A_0 and A_1 diverge at Δ_F , with an exponent of $1/2$, as is typical for a mean-field second-order transition.

Strongly localized limit

In this limit of $m \rightarrow 1$ we have

$$\Delta(m) \simeq \frac{16}{L} K(m), \quad (2.57a)$$

$$P(m) \simeq 2 - \frac{16}{L^2} K(m)^2. \quad (2.57b)$$

Eliminating the parameter m between these two last relations leads to

$$P = 2 - \frac{\Delta^2}{16} = 2 - \frac{\pi^2}{4} \left(\frac{\Delta}{\lambda} \right)^2, \quad (2.58)$$

which coincides with the exact pressure-displacement relation for infinite sheets [41]. In this limit, we also have $\text{dn}(u, m) \rightarrow 1/\cosh(u)$ [124], such that the profile (2.45b) becomes

$$h(s) = \frac{\Delta}{2} \frac{\cos(s)}{\cosh(s/\xi)}, \quad \xi = 8/\Delta, \quad (2.59)$$

which coincides with the approximate localized fold for an infinite sheet [40, 49]. The amplitude A_0 is thus given by the following simple relation,

$$A_0 = \Delta/2, \quad (2.60)$$

which again is identical to the exact result for an infinite sheet [41].

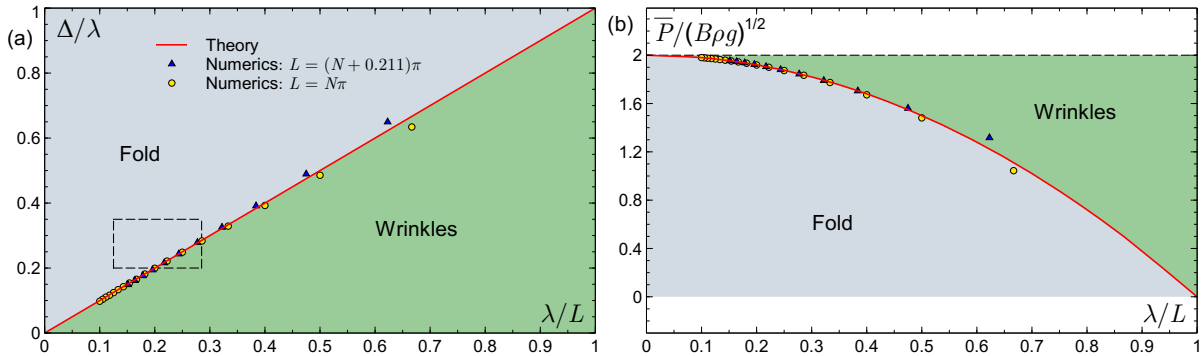


Figure 2.5: Phase diagrams of an incompressible fluid-supported sheet. (a) Phase diagram on the displacement–length plane. For $0 < \Delta < \lambda^2/L$ the sheet forms extended wrinkles, and for $\Delta > \lambda^2/L$ a localized fold is formed. The rectangle shows the range of the experimentally determined phase boundary [39] (see also Fig. 2.7). (b) Phase diagram on the pressure–length plane. \bar{P} is the physical dimensional pressure. Wrinkles are stable for $2 - 2\lambda^2/L^2 < P < 2$, and a fold is stable for $P < 2 - 2\lambda^2/L^2$. The wrinkle-fold line is a second-order transition. Note how the region of stable wrinkles in both diagrams vanishes in the limit of an infinite sheet. In both diagrams, the theoretical transition curves are compared to the numerical transition obtained by solving Eq. (2.8) and analyzing the periodicity of the numerical solution from the relative height of its extrema. Numerical results for both commensurate (L being an integer or half-integer multiple of λ) and incommensurate sheets are presented, showing a negligible discrepancy between these two and the theoretical prediction for $L \gtrsim 2\lambda$.

2.5 Wrinkle-to-fold transition

Below a critical value of $\epsilon L = \epsilon_F L = 2^{3/2}\pi$, Eq. (2.44) has no solution for m . Thus, below this critical confinement, the localized solution does not exist, and the only possible envelope is the trivial constant one, corresponding to wrinkles. At $\epsilon_F L$ itself Eq. (2.44) admits $m = 0$ as a unique solution, and for larger values of ϵL , with $m > 0$ as a unique solution, the envelope grows continuously, corresponding to increasingly localized patterns. Accordingly, we define the order parameter of the wrinkle-to-fold transition as m , and its control parameter as

$$\tau \equiv \epsilon L, \quad \tau_F = \epsilon_F L = 2^{3/2}\pi. \quad (2.61)$$

2.5.1 Landau expansion

A clear way to present the continuous transition is through a Landau expansion of the energy, G , in small order parameter. The Landau expansion is to be performed on the energy *prior to minimization*. For this purpose, we use the following form for the envelope:

$$H_1^*(S) = \frac{2}{\sqrt{2-m}} \operatorname{dn} \left(\frac{2K(m)}{\tau} S, m \right), \quad (2.62)$$

where we have substituted the boundary condition (2.44) in the argument of the profile given by Eq. (2.43), but not in its amplitude. Therefore, $H_1^*(S)$ satisfies the boundary conditions but does not yet minimize the energy.

Substituting Eq. (2.62) in Eq. (2.40) and expanding to fourth order in small m , yields

$$\Delta G \simeq (\tau_F^2 - \tau^2)(m^2 + m^3) + \frac{3}{128}(35\tau_F^2 - 33\tau^2)m^4, \quad (2.63)$$

where $\Delta G = 32L(G - G_W)/\epsilon^2$, and $G_W = L\epsilon^4/4$ is the energy of the wrinkles. The appearance of the m^3 term has no significance for the transition because of its vanishing prefactor. Upon minimization of ΔG with respect to m we obtain,

$$m \simeq 8[(\tau - \tau_F)/3\tau_F]^{1/2}, \quad (2.64)$$

with a critical exponent, $\beta = 1/2$, as usual for a mean-field second-order transition.

Using the expression (2.61) of τ_F in Eqs. (2.33) and (2.38) for P and Δ , we recover the critical values derived in Sec. 2.4.2 from the analysis of weakly localized folds. We repeat here these central results:

$$P_F = P_W - \tau_F^2/L^2 = 2 - 8\pi^2/L^2, \quad (2.65)$$

$$\Delta_F = \tau_F^2/(2L) = 4\pi^2/L. \quad (2.66)$$

The value of $\Delta_F \simeq 39.5/L$ corrects an earlier, higher estimate of $\Delta_F = 48/L$, which was obtained by using an Ansatz profile that was not an energy minimizer [49]. Equations (2.65) and (2.66) confirm that the wrinkle-to-fold transition can be made arbitrarily close to the flat-to-wrinkle one with increasing size of the sheet. Consequently, this separate second-order transition appears only in finite systems.

In Fig. 2.5 we summarize the phase diagrams of the incompressible fluid-supported sheet on the Δ - L and P - L planes. Note that these scaled diagrams are parameter-free.

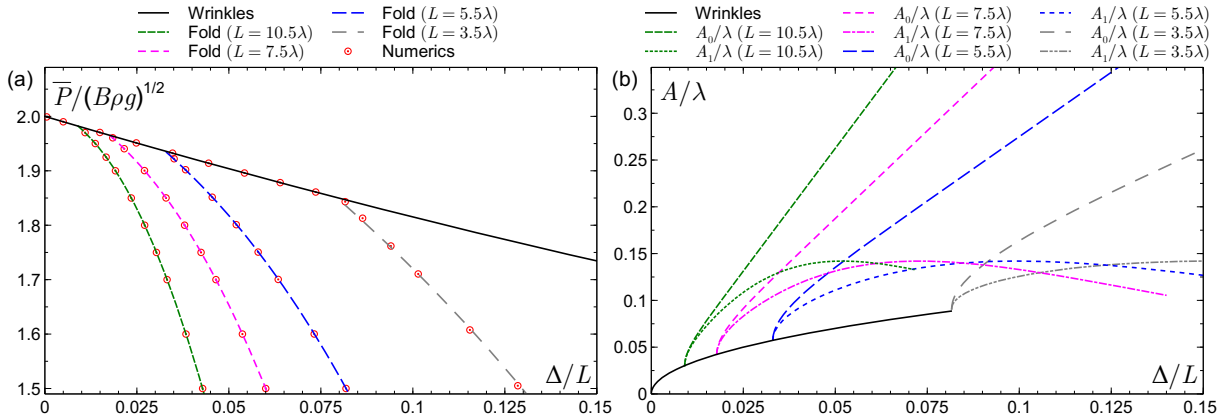


Figure 2.6: (a) Evolution of the rescaled pressure as a function of the relative displacement for various sheet lengths L . \bar{P} is the physical dimensional pressure. The graphs show the evolution of the pressure for the periodic state (wrinkles) together with the bifurcations toward the localized state (fold) at $\Delta/L = \Delta_F/L = \lambda^2/L^2$ and $P = 2 - 2\Delta_F/L$. These bifurcations decrease the energy of the system compared to the periodic state. (b) Evolution of the amplitudes of the pattern, rescaled by the wrinkles wavelength, as a function of the relative displacement for the same sheet lengths as those used in panel (a). The wrinkles amplitude grows as $(\Delta/L)^{1/2}$ until the point $\Delta/L = \lambda^2/L^2$ and $A/\lambda = \lambda/L\pi$ is reached, where the localized state emerges. The evolution of the amplitude of the central fold, A_0 , and of the fold next to it, A_1 , are shown.

2.5.2 Matching at the transition

Below the wrinkle-to-fold transition and considering small wrinkles (to first order in Δ/L), we have found in Sec. 2.3.3,

$$P = 2 \left(1 - \frac{\Delta}{L}\right), \quad A_0 = 2\sqrt{\frac{\Delta}{L}}, \quad h(s) = A_0 \cos(s). \quad (2.67)$$

At the wrinkle-to-fold-transition, we have shown that $\Delta = \Delta_F = \lambda^2/L$ and $P = P_F = 2 - 2\lambda^2/L^2$. Slightly above the transition, the weakly localized solution is characterized by (see Sec. 2.4.2),

$$\begin{aligned} P &= 2 \left(1 - \frac{\Delta_F}{L}\right) - 6 \left(\frac{\Delta - \Delta_F}{L}\right), \\ A_0 &= \frac{2\lambda}{L} + 2\sqrt{2} \left(\frac{\Delta - \Delta_F}{L}\right)^{1/2}, \\ h(s) &= \frac{2\lambda}{L} \cos(s), \quad \text{at the transition.} \end{aligned} \quad (2.68)$$

Comparing Eqs. (2.67) and (2.68), we see that the transition is continuous. The discontinuity appears in the pressure derivative, with $(dP/d\Delta)_{\Delta \rightarrow \Delta_F^-} = -2/L$ and $(dP/d\Delta)_{\Delta \rightarrow \Delta_F^+} = -6/L$. Hence, the continuous transition is of second order (discontinuity in the second derivative of E with respect to Δ). The pressure associated with the localized solution is smaller than the one associated with the periodic solution once $\Delta > \Delta_F$, as illustrated in Fig 2.6a. Since $P = dE/d\Delta$, the localized state has a smaller energy compared to the energy of the periodic state. The latter is thus unstable once $\Delta > \Delta_F$. The evolution of the amplitudes of the wrinkle and localized states as the displacement increases is shown in Fig 2.6b.

2.6 Discussion

2.6.1 Experimental consequences

The system parameters are the length L and bending modulus B of the thin elastic sheet, and the density ρ of the liquid. The experimental control parameter is either the displacement Δ or the force per unit length P . The measured quantity is the height profile, including the wrinkles wavelength, λ , and height extrema [39].

The order parameter m , which we have defined here, characterizes the decay of the envelope away from the center of the fold. Experimentally, one may look instead at the height difference

between two consecutive local extrema A_0 and A_1 [39]. These two definitions of the order parameter are equivalent close to the transition. Indeed, from Eqs. (2.52) and (2.56) we find

$$M_{\text{exp}} \equiv 1 - \frac{A_1}{A_0} = \frac{1}{2} [\sin(\lambda\pi/2L)]^2 m + \mathcal{O}(m^2) = \frac{\pi^2 \lambda^2}{8L^2} m + \mathcal{O}(m^2, \lambda^4/L^4). \quad (2.69)$$

Using Eq. (2.52), or equivalently Eq. (2.64), this result is written as a function of the experimental control parameter Δ :

$$M_{\text{exp}} = \frac{\pi^2 \lambda}{\sqrt{2} L} \left(\frac{\Delta - \Delta_{\text{F}}}{L} \right)^{1/2}, \quad (2.70)$$

where Δ_{F} is given by Eq. (2.51).

The evolution of the pattern amplitude as a function of the displacement can also be measured. Such data are available in Ref. [39], whose main purpose was to show the universality of the folding state where all the data collapsed onto a master curve for large enough confinement. Indeed, in the large-confinement regime, the sheet deformation is localized in a small region, comparable to the wrinkle wavelength λ , and does not depend significantly on the sheet length L , provided that L is sufficiently large compared to λ . The data of Ref. [39] are reproduced in Fig. 2.7 together with the evolution of the amplitudes predicted by the present theory. (Note that, to comply with the presentation of the experimental data, the amplitude in Fig. 2.7 is drawn as a function of Δ/λ rather than Δ/L as in Fig. 2.6b.)

Our theory is valid for large enough sheets and consequently for a sufficiently small relative confinement $\Delta/L \ll 1$. See, for example, the deviation of the amplitude A_1 at large Δ/L for a small system with $L/\lambda = 3.5$ (Fig. 2.7). On the other hand, at large Δ/λ , as the localization length becomes significantly smaller than L , the exact predictions for an infinite sheet [41] become accurate for finite sheets as well (see Fig. 2.7). Finally, for the localized state we have assumed a commensurate sheet (L being an integer or half-integer multiple of λ). Yet, as shown in Fig. 2.5, the effect of incommensurability becomes negligible already for sheets larger than 2λ , making it inconsequential experimentally.

The authors of Ref. [39] inferred from their experiments that the wrinkle-to-fold transition occurred at a value of $\Delta \simeq 0.3\lambda$ for all sheet lengths L , whereas our theory gives an L -dependent critical displacement (see Fig. 2.5a). As seen in Fig. 2.7, it was natural to draw that conclusion given the experimental error. The rectangle shown in the diagram of Fig. 2.5a, representing the range of the experimentally determined thresholds (Fig. 2.7), is consistent with the theoretical prediction. Clearly, accurate experimental data focusing on the transition region are still needed. For this purpose we summarize the predictions for the amplitude evolution below and above

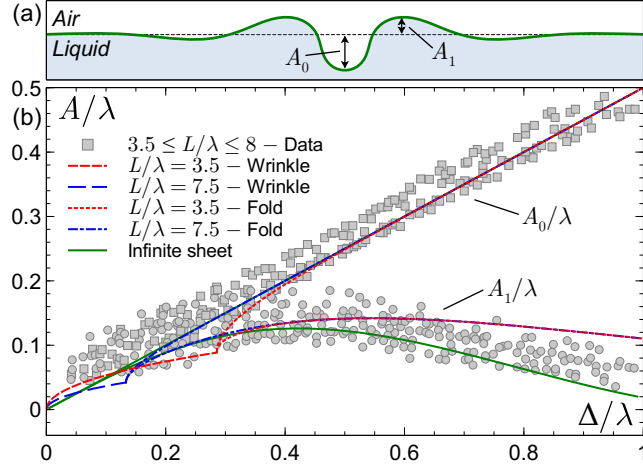


Figure 2.7: (a) Definitions of the amplitudes A_0 and A_1 for the localized state. (b) Comparison between the experimental evolution of A_0 and A_1 (rescaled by λ) with increasing confinement for finite sheets [39], and the prediction of Eq. (2.45b) where $A_0 = |h(0)|$ and $A_1 = |h(\pi)|$. The evolution of the amplitudes of the exact solution for an infinite sheet is also presented [41].

the transition:

For $\Delta < \Delta_F$:

$$\frac{A}{\lambda} = \frac{1}{\pi} \left(\frac{\Delta}{L} \right)^{1/2}, \quad (2.71a)$$

For $\Delta \gtrsim \Delta_F$:

$$\frac{A_0}{\lambda} = \frac{\lambda}{\pi L} + \frac{\sqrt{2}}{\pi} \left(\frac{\Delta - \Delta_F}{L} \right)^{1/2}, \quad (2.71b)$$

$$\frac{A_1}{\lambda} = \frac{\lambda}{\pi L} + \frac{\sqrt{2}}{\pi} \cos \left(\frac{2\pi^2}{L} \right) \left(\frac{\Delta - \Delta_F}{L} \right)^{1/2}. \quad (2.71c)$$

In Sec. 2.4, we derived the properties of the critical wrinkle-to-fold transition at which the localization length ξ diverges. As for critical phenomena in a finite system, the transition will be observable in practice only when the localization length becomes smaller than the system size, $\xi \lesssim L$. We find, however, that the displacement required to get $\xi \simeq L$ is larger than Δ_F by only 0.4%. Thus, the finite size of the system should have a negligible effect on the experimentally observed critical displacement.

2.6.2 Conclusion

In the present work we have derived an exact solution for the wrinkle state in a finite fluid-supported sheet. The theory developed for fold localization, however, is restricted to large sheets; it is correct to first order in λ/L . A higher-order theory (next order in ϵ of the multiple-scale expansion) would not change the main conclusions obtained above. It is expected to slightly modify some quantitative predictions such as the value of the critical wrinkle-to-fold confinement, Δ_F . The possibility to discriminate experimentally between the present theory of the transition and a higher-order one is doubtful.

Although we found exact localized solutions for the governing equation (2.8), these do not give the physical profile of the sheet (see Appendix A.1). Mathematically, the inability to derive physical localized profiles from these solutions may indicate that such profiles belong to a different branch of solutions to the non-linear governing equation. Such a branch is yet to be found. If it exists, it will probably coincide, in the limit $L \rightarrow \infty$, with the exact solution known for this limit [41].

An important extension to the present theory is the inclusion of finite compressibility of the sheet. This will allow us to treat the flat-to-wrinkle transition, and thus construct the complete “phase-diagram” of the floating sheet including the two transitions.

Chapter 3

Properties of extensible elastica from relativistic analogy¹

3.1 Introduction

Analogies to dynamical problems have been used to simplify the physics of various condensed-matter systems, ranging from the deformation of elastic bodies to the order-parameter profile across an interface between coexisting phases. A particularly well known example is Kirchhoff's kinetic analogy [22]. In this theory the three-dimensional (3D) deformation of a slender elastic rod is reduced to the bending deformation of an inextensible curve, representing the mid-axis of the rod. This problem, in turn, is analogous to the dynamics of a rigid body rotating about a fixed point, where the distance along the curve and its local curvature are analogous, respectively, to time and angular velocity. When the filament is confined to a two-dimensional (2D) plane (the celebrated Euler elastica [21], see Chapter 1 Sec. 1.2.1), the equation of equilibrium coincides with the equation of motion of a physical pendulum [22, 52], see discussion in Sec. 1.2.3.

In the examples above the elastic system was reduced to an indefinitely thin, inextensible body, whose equilibrium shape follows the trajectory of a classical dynamical system. In the present work we show that relaxing the inextensibility constraint introduces terms akin to relativistic corrections to classical dynamics. Within this analogy, the compression modulus,

¹The material presented in this Chapter was published in O. Oshri and H. Diamant, *Soft Matter (Communication)* **12**, 664-668 (2016) [32].

Y , plays the role of the relativistic particle's rest mass, and the bendability parameter $h^{-1} \equiv (Y/B)^{1/2}$, where B is the bending modulus, is analogous to the speed of light. The limit of an inextensible rod ($h \rightarrow 0$) corresponds to the nonrelativistic limit. . (The symbol h , having units of length and denoting here the quantity $(B/Y)^{1/2}$, should not be confused with the height variable used in Chapter 2.)

3.2 The elastic energy from a discrete model

Despite the relevance to real systems, including compressible fluid membranes [26], there have not been many studies of extensible elastica (see [28] and references therein). Following these works, we consider the 2D deformation of an extensible filament, represented by a planar curve of relaxed length L . The same model applies to thin elastic sheets, as well as fluid membranes [25], provided that they are deformed along a single direction. The deformation away from the flat, stress-free state is parametrized by the angle $\phi(s)$ and compressive strain $\gamma(s)$, as functions of the relaxed arclength s along the curve, $s \in [0, L]$; see Fig. 3.1(a). We denote the compressed arclength by \hat{s} , such that $\gamma = d\hat{s}/ds$ and the total deformed length is $\hat{L} = \int_0^{\hat{L}} d\hat{s} = \int_0^L \gamma(s) ds$.

To obtain the energy functional which keeps the bending and stretching contributions independent, it is instructive to start from a discrete model (see Fig. 3.1(b)). Consider a chain of N jointly connected extensible rigid bonds of rest length a . The chain's configuration is parametrized by a set of bond strains γ_n ($1 \leq n \leq N$) and a set of joint angles ϕ_n ($1 \leq n \leq N - 1$). The energy of a given configuration has a stretching contribution, $E_s = (Y/2a) \sum_{n=1}^N (\gamma_n a - a)^2$, and a bending contribution, $E_b = (B/2a) \sum_{n=1}^{N-1} (\phi_{n+1} - \phi_n)^2$. For the sake of the analogy we add a potential energy of the form, $E_p = a \sum_{n=1}^N \gamma_n V(\phi_n)$, where $V(\phi)$ is an angle-dependent potential. This choice of potential energy is not artificial. For example, if we include an external work on the chain, coupling the force P exerted on the boundaries with the chain's projected length, we have $E_p = Pa \sum_{n=1}^N \gamma_n \cos \phi_n$, i.e. $V(\phi) = P \cos \phi$. We now take the continuum limit, $N \rightarrow \infty$ and $a \rightarrow 0$ such that $Na \rightarrow L$ and $na \rightarrow s$, getting,

$$E[\phi(s), \gamma(s)] = E_b + E_s + E_p = \int_0^L ds \left[\frac{B}{2} \left(\frac{d\phi}{ds} \right)^2 + \frac{Y}{2} (\gamma - 1)^2 + \gamma V(\phi) \right]. \quad (3.1)$$

To obtain the equations of equilibrium for the filament one should minimize E with respect

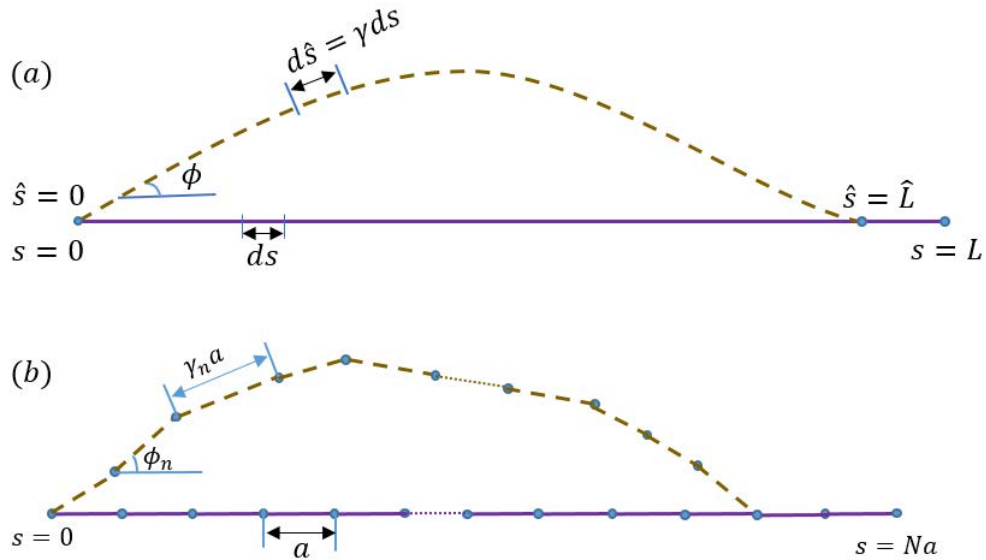


Figure 3.1: (a) Deformed and undeformed planar configurations. The straight line (solid, purple) represents a relaxed rod of initial length L , and the curved line (dashed, gold) represents a deformed rod of total length \hat{L} . Their arclength parameters are s and \hat{s} respectively. The local in-plane and out-of-plane deformations are respectively accounted for by the compression field $\gamma = d\hat{s}/ds$ and the angle $\phi(s)$. (b) An illustration of the discrete model. The initial, zero-energy configuration (solid, purple) consists of N rigid bonds of rest length a and zero joint angles. A higher-energy state (dashed, gold) is obtained by compression of each bond, $a \rightarrow \gamma_n a$, and/or a change of each joint angle, ϕ_n . The continuous limit of this model yields the picture presented in panel (a).

to $\gamma(s)$ and $\phi(s)$. This gives the two equations,

$$Y(\gamma - 1) + V = 0, \quad (3.2a)$$

$$B \frac{d^2 \phi}{ds^2} - \gamma \frac{dV}{d\phi} = 0. \quad (3.2b)$$

First integration yields,

$$\mathcal{H} = \frac{B}{2} \left(\frac{d\phi}{ds} \right)^2 - \frac{Y}{2} (\gamma - 1)^2 - \gamma V = \text{const}, \quad (3.3)$$

which depends on the boundary conditions at $s = 0, L$.

3.3 Analogy to relativistic dynamics

The mathematical analogy to relativistic dynamics is revealed once we transform from the relaxed arclength, s , to the compressed one, \hat{s} , and redefine the potential as $\bar{V} = -V$. Equations

tion (3.2b) then turns into

$$B \frac{d}{d\hat{s}} \left(\gamma \frac{d\phi}{d\hat{s}} \right) + \frac{d\bar{V}}{d\phi} = 0. \quad (3.4)$$

This equation is analogous to the Euler-Lagrange equation for the one-dimensional motion of a relativistic particle [125], provided that $\gamma(\hat{s})$ coincides with the Lorentz factor. To obtain γ we use Eq. (3.3) to eliminate V in Eq. (3.2a), and transform to \hat{s} , which gives,

$$\gamma = \frac{\sqrt{1 + 2\mathcal{H}/Y}}{\sqrt{1 + h^2(d\phi/d\hat{s})^2}}. \quad (3.5)$$

This expression indeed resembles the Lorentz factor up to the constant prefactor, $\gamma_0 \equiv \sqrt{1 + 2\mathcal{H}/Y}$. Absorbing this prefactor in the potential \bar{V} makes Eq. (3.4) identical to the relativistic one, with the correct Lorentz factor. This completes the analogy. The mapping between the variables and parameters of these two systems is summarized in Table 3.3.

| Elasticity | Relativity |
|---|---------------------------------------|
| relaxed arclength ² , s | proper time, τ |
| compressed arclength, \hat{s} | laboratory time, t |
| tangent angle, ϕ | angle coordinate, ϕ |
| curvature, $\kappa = d\phi/d\hat{s}$ | angular velocity, $\omega = d\phi/dt$ |
| compression field ² , $\gamma = d\hat{s}/ds$ | Lorentz factor, $\gamma = dt/d\tau$ |
| compression modulus, Y | minus the rest energy, $-mc^2$ |
| bending modulus, B | moment of inertia, $m\ell^2$ |
| bendability, $h^{-1} = \sqrt{Y/B}$ | speed of light, c |

Table 3.1: Mapping between the parameters of extensible elastica and relativistic dynamics

3.4 Symmetry of extensible elastica

We now use the mapping to identify a new symmetry of extensible elastica. First, recall that the equation of equilibrium of *inextensible* elastica is invariant to the addition of a constant curvature κ , making a flat configuration cylindrical. The kinetic analogue of this symmetry is the Galilean invariance of the equation of motion of a classical free particle to a boost by a constant velocity. We are after the corresponding symmetry for an *extensible* elastic filament. It is natural to try the analogue of a Lorentz boost. To make the connection to a free particle we first remove the potential energy from Eq. (3.4), $\bar{V}(\phi) = 0$, and then divide by $B\gamma_0$. The

² More accurately, the analogue of τ is $\gamma_0 s$, where γ_0 is a constant prefactor (see text).

resulting equation of elastic equilibrium,

$$\frac{d}{d\hat{s}} \left(\frac{1}{\sqrt{1+h^2(d\phi/d\hat{s})^2}} \frac{d\phi}{d\hat{s}} \right) = 0, \quad (3.6)$$

is identical to the equation of motion of a free relativistic particle. With the Lorentz boost in mind, we immediately identify the transformation of coordinates $(\hat{s}/h, \phi) \rightarrow (\hat{S}/h, \Phi)$, which leaves Eq. (3.6) unchanged:

$$\begin{pmatrix} \hat{s}/h \\ \phi \end{pmatrix} = \begin{pmatrix} \gamma & -\gamma h\kappa \\ \gamma h\kappa & \gamma \end{pmatrix} \begin{pmatrix} \hat{S}/h \\ \Phi \end{pmatrix}, \quad (3.7)$$

where $\kappa = \text{const}$, and $\gamma = 1/\sqrt{1+h^2\kappa^2}$. The transformation is a rotation of the material coordinates, $(\hat{s}/h, \phi)$, by an angle $\theta = \sin^{-1}(\gamma h\kappa)$, turning a flat, relaxed configuration into a cylindrical, compressed one; see Fig. 3.2. The rotation leaves the line element on the material-coordinates plane unchanged, $d\hat{s}^2/h^2 + d\phi^2 = d\hat{S}^2/h^2 + d\Phi^2$. This reparametrization invariance defines a continuous family of solutions to the equation of equilibrium, containing all the cylindrical, compressed configurations of the filament. These configurations satisfy local mechanical equilibrium but differ in their total energy. (Obviously, the flat relaxed configuration always has the lowest energy.) The actual equilibrium configuration for a given problem is selected by boundary conditions. To our knowledge, this symmetry of extensible filaments has not been recognized before.

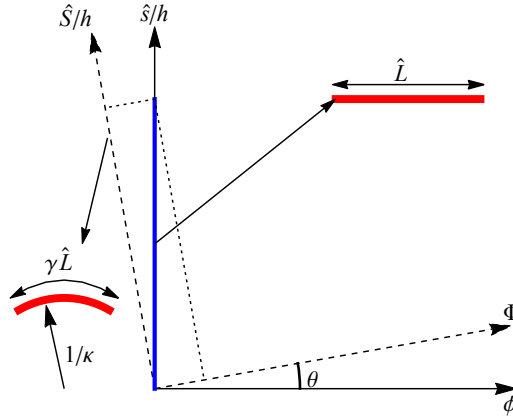


Figure 3.2: Rigid rotation of the coordinate system $(\hat{s}/h, \phi) \rightarrow (\hat{S}/h, \Phi)$ by an angle θ . A flat elastic filament of length \hat{L} is described by the blue line. As viewed from the new frame, the total length is compressed by a factor γ , and the angle coordinate, Φ , is linearly changing, resulting in a cylindrical compressed shape of radius $1/\kappa$ and length $\gamma\hat{L}$.

An important physical distinction should be made, however, between the two sides of the analogy. In the elastic problem one naturally specifies the length L and the boundary conditions

with respect to that relaxed state; the compressed length \hat{L} is determined by minimization. By contrast, in relativity the duration of the experiment and the boundary conditions are given in the laboratory frame, not the proper one. This difference leads to the extra prefactor γ_0 (see further discussion in Appendix B.1). Thanks to this prefactor the elastic strain can be either compressive or dilative, whereas the relativistic Lorentz factor must be dilative.³ Note that, because of the minus sign in the mapping $Y \rightarrow -mc^2$, time dilation corresponds to elastic compression.

Despite the physical difference, by absorbing the factor γ_0 in the potential, the two problems become mathematically equivalent. Thus, a known solution in one system can be readily transferred to the other.

3.5 Exact solution to the relativistic non-linear pendulum

We shall now use known results for the buckling of extensible elastica to write down an explicit solution to the equation of motion of a relativistic nonlinear pendulum. (A solution to this dynamical system was previously given only in implicit parametric form [126].)

To do so, we should specialize to the potential $V(\phi) = P \cos \phi$. Substitution of V in Eq. (3.2a) gives $\gamma = 1 - (P/Y) \cos \phi$. These expressions for V and γ turn Eq. (3.2b) into

$$B \frac{d^2 \phi}{ds^2} + P \sin \phi - \frac{P^2}{Y} \sin \phi \cos \phi = 0, \quad (3.8)$$

which is the equation of equilibrium for an extensible elastica under a uniaxial force P [28, 31]. The exact solution to Eq. (3.8) was derived in Ref. [28]. For hinged boundary conditions, $d\phi/ds = 0$ at $s = 0, L$, it is given by

$$\phi(s) = 2 \sin^{-1} \left[q \frac{(1 - (qkh)^2/\gamma_0)^{1/2} \text{cd}(\sqrt{\gamma_0}ks, m)}{[1 - (qkh)^2/\gamma_0 \text{cd}^2(\sqrt{\gamma_0}ks, m)]^{1/2}} \right]. \quad (3.9)$$

Hereafter we use the conventional symbols for the various elliptic functions, cd , am , K and Π , as defined in Ref. [124]. In addition, $k \equiv \sqrt{P/B}$ is the wavenumber of the buckled *linear* elastica. We have defined three additional parameters which depend on the boundary angle,

³If we formulated the elastic problem and its boundary conditions, unphysically, based on the ultimate deformed length \hat{L} , the information on the reference state would be lost, and the two problems, the elastic and relativistic, would become identical. This can be readily shown by transforming Eq. (3.1) to \hat{s} and minimizing with respect to γ (see Appendix B.1).

$\phi_0 \equiv \phi(s = 0)$:

$$\begin{aligned} q &\equiv \sin(\phi_0/2) \\ \gamma_0 &= 1 - (kh)^2 \cos \phi_0 \\ m &= q^2 [1 + (qkh)^2] / \gamma_0. \end{aligned} \quad (3.10)$$

The parameter $\gamma_0 = \gamma(s = 0)$ gives the boundary strain, which coincides with γ_0 as defined above. The actual wavelength (periodicity) λ of the nonlinear buckled elastica is

$$\lambda = 4K(m)/(\sqrt{\gamma_0}k). \quad (3.11)$$

The total rod length matches a half wavelength, $L = \lambda/2$. This expression relates ϕ_0 to the force P and the system parameters via Eq. (3.10). The total deformed length is given by $\hat{L} = \int_0^L [1 - (kh)^2 \cos \phi] ds$, yielding,

$$\hat{L}/L = 1 - (kh)^2 \left[2(1 - q^2) \frac{\Pi(q^2, m)}{K(m)} - 1 \right]. \quad (3.12)$$

It is readily shown that the three known solutions for inextensible nonlinear elastica ($h \rightarrow 0$) [22], extensible linear elastica ($\phi_0 \ll 1$) [28], and inextensible linear elastica ($h \rightarrow 0, \phi_0 \ll 1$) [22], are obtained from Eq. (3.9) in the respective limits.

To apply the analogy, we first transform Eq. (3.8) to the deformed arclength \hat{s} using Eqs. (3.2a), (3.3) and (3.5). This leads to

$$\frac{d}{d\hat{s}} \left(\frac{1}{\sqrt{1 + h^2(d\phi/d\hat{s})^2}} \frac{d\phi}{d\hat{s}} \right) + \frac{k^2}{\gamma_0} \sin \phi = 0. \quad (3.13)$$

Next, substituting

$$\{h^2, k^2/\gamma_0\} \rightarrow \{-\ell^2/c^2, \omega^2\},$$

where ω is the natural frequency of the corresponding linear pendulum and ℓ the pendulum length, the equation of motion for a relativistic pendulum [127] readily follows:

$$\frac{d}{dt} \left(\frac{1}{\sqrt{1 - (\ell^2/c^2)(d\phi/dt)^2}} \frac{d\phi}{dt} \right) + \omega^2 \sin \phi = 0. \quad (3.14)$$

From Eq. (3.9) we then immediately write down the explicit solution for the pendulum motion in terms of its proper time,

$$\phi(\tau) = 2 \sin^{-1} \left[q \frac{[1 + (q\omega\ell/c)^2]^{1/2} \text{cd}(\omega\tau, m)}{[1 + (q\omega\ell/c)^2 \text{cd}^2(\omega\tau, m)]^{1/2}} \right], \quad (3.15)$$

where, from Eq. (3.10), $q = \sin(\phi_0/2)$ is related to the initial angle of the pendulum, and $m = q^2[1 - (\omega\ell/c)^2(1 - q^2)]$. Similarly, the proper period of the pendulum is obtained by analogy to $\gamma_0\lambda$ of Eq. (3.11),

$$T_\tau = 4K(m)/\omega, \quad (3.16)$$

and the laboratory period from $\hat{L}/(\gamma_0 L)$ of Eq. (3.12),

$$T_t/T_\tau = 1 + 2(\omega\ell/c)^2(1 - q^2) \left[\frac{\Pi(q^2, m)}{K(m)} - 1 \right]. \quad (3.17)$$

Finally, we can transform the solution (3.15) to laboratory time through

$$t = \tau + \frac{2(1 - q^2)}{\omega} (\omega\ell/c)^2 [\Pi(q^2, \text{am}(\omega\tau, m), m) - \omega\tau]. \quad (3.18)$$

In Fig. 3.3 we show the resulting motion of the pendulum in both proper and laboratory times. The dilation of the period of the relativistic pendulum (solid curve), compared to the nonrelativistic one (dash-dotted), illustrates the compression of the buckling wavelength in the extensible elastica compared to the inextensible case.

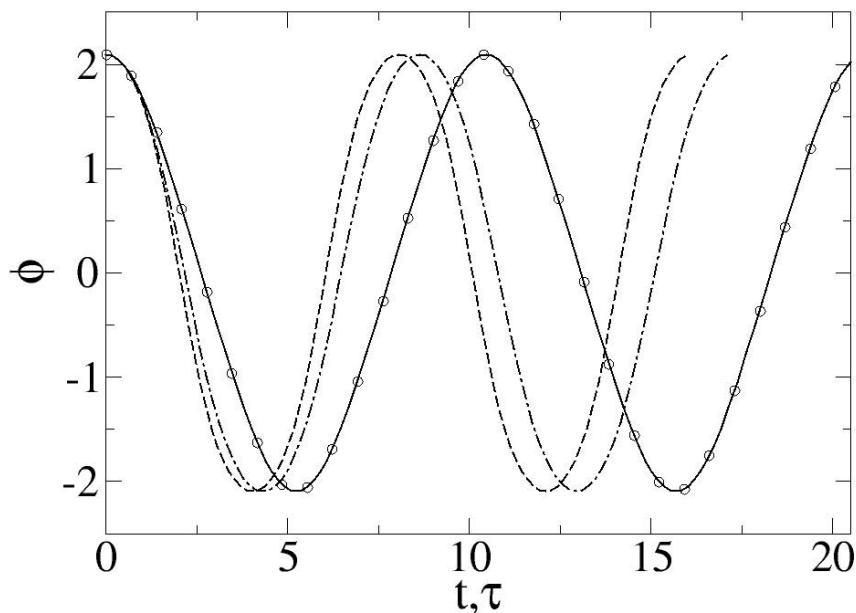


Figure 3.3: Pendulum angle as a function of proper time (Eq. (3.15), dashed line) and laboratory time (Eqs. (3.15) and (3.18), solid line). The chosen parameters, $\phi_0 = 2\pi/3$, $\omega = 1$, $(\omega\ell/c)^2 = 0.5$, correspond to a highly relativistic pendulum resulting in a significant time dilation. Numerical solution of the equation of motion (Eq. (3.14), circles) and the case of a nonrelativistic pendulum ($c \rightarrow \infty$, dash-dotted) are plotted for comparison.

3.6 Discussion

We begin with two additional short comments concerning the analogous systems. First, a similar factor to the elastic γ_0 is encountered in certain relativistic scenarios [126, 128]. Second, we note that the usage of the original strain field to derive the elastic γ looks similar in spirit to the “einbein” used to simplify the analysis of actions in different physical contexts [129]. Unlike those analyses, however, γ here is an actual physical strain, the choice of which is not free but dictated by elasticity.

The extended Kirchhoff analogy presented in this work should be useful for studying various soft matter systems. In principle, extensibility corrections are negligible for sufficiently slender (and therefore bendable) objects. There are several indications, however, that the extensible-elastica model may be qualitatively predictive beyond its strict limits of validity. For example, it produces negative compressibility (decrease of the force P with increasing confinement) for bendability h^{-1} of order 1 [28]. Although the model is invalid for such values of h^{-1} , this result is in qualitative agreement with recent experimental and numerical results for buckled beams [130]. In Ref. [26] Diggins *et al.* studied the buckling of fluid membranes under uniaxial confinement using molecular dynamics simulations. To improve the analysis of the simulation data beyond the inextensible Euler elastica, they used, on purely empirical grounds, expressions which are very similar to the ones presented here, obtaining good fits to the numerical results. The reason for the unexpected success of the extensible-elastica model in these two examples is unclear at present. Extensibility is essential in the case of two-dimensional deformations with non-zero Gaussian curvature. The present 1D model, as far as we know, has no applicability in such cases. It is relevant, however, to deformations with cylindrical [61, 131] or conical [13] symmetries.

Lastly, the analogy can be extended to three dimensions, where the deformation of an extensible filament in 3D becomes analogous to a relativistic rotor, as outlined in Appendix B.2.

Chapter 4

Strain tensor selection and the elastic theory of incompatible thin sheets¹

4.1 Introduction

In the past two decades there has been a renewed interest in the elasticity of thin solid sheets in view of the wealth of surface patterns and three-dimensional (3D) shapes that they exhibit under stress [7, 11, 13, 40, 42, 43, 62, 111, 133]; see Chapter 1, Sec. 1.3. In addition, experiments and models have been devised for *incompatible* sheets, which contain internal residual stresses even in the absence of external forces [68–71, 76–78, 134–146]. The study of such sheets has been motivated by their relevance to morphologies in nature [76, 79, 134, 136, 138] and frustrated self-assembly [79, 85]. Incompatible sheets form nontrivial 3D shapes *spontaneously*. They can also be “programmed” to develop a desired 3D shape [70, 72, 75, 140, 147, 148], see discussion in Sec. 1.3.2.

We first recall the fundamental points introduced in Sec. 1.3.2. The necessary existence of sheets with unremovable internal stresses is rationalized as follows. When treating a thin solid sheet as a mathematical surface, its relaxed state is characterized by a 2D reference metric tensor, $\bar{g}_{\alpha\beta}$, associated with the relaxed in-plane configuration, and a reference second fundamental form, $\bar{b}_{\alpha\beta}$, related to the relaxed out-of-plane configuration (curvature) [68]. (We shall use Latin

¹The material presented in this Chapter has been submitted for publication. A preprint can be found in [132].

indices (i, j, \dots) for 3D coordinates and Greek indices (α, β, \dots) for 2D ones.) However, not any $\bar{g}_{\alpha\beta}$ and $\bar{b}_{\alpha\beta}$ correspond to a physical surface. For the surface to be embeddable in 3D Euclidean space, these forms must satisfy a set of geometrical constraints [20, p. 203]. Thus, in general, an actual sheet will be incompatible—its actual metric and second fundamental form, $a_{\alpha\beta}$ and $b_{\alpha\beta}$, will not coincide with their reference counterparts—leading to unavoidable intrinsic stresses.

A covariant theory for incompatible elastic bodies has been presented by Efrati, Sharon, and Kupferman (referred to hereafter as ESK) [68] and successfully applied to several experimental systems [79, 82, 85] (for specific examples, see again Sec. 1.3.2). Their elastic energy for a 3D body reads,

$$E_{3D} = \int_{\mathcal{V}} \mathcal{A}^{ijkl} \tilde{\epsilon}_{ij} \tilde{\epsilon}_{kl} \sqrt{|\bar{g}|} dV, \\ \tilde{\epsilon}_{ij} = \frac{1}{2}(g_{ij} - \bar{g}_{ij}), \quad (4.1)$$

where the integration is over the unstrained volume, \mathcal{V} , g_{ij} and \bar{g}_{ij} are the metric and reference metric, \bar{g} is the determinant of the reference metric and \mathcal{A}^{ijkl} is the elastic tensor. To explicitly distinguish the strain used by ESK we mark it with a tilde. ESK also presented a dimensional reduction of this energy to 2D for incompatible thin elastic sheets, resulting in a sum of stretching and bending contributions,

$$\text{ESK: } E_{2D} = E_s + E_b = \frac{t}{2} \int_A \mathcal{A}^{\alpha\beta\gamma\delta} \tilde{\epsilon}_{\alpha\beta} \tilde{\epsilon}_{\gamma\delta} \sqrt{|\bar{g}|} dA + \frac{t^3}{24} \int_A \mathcal{A}^{\alpha\beta\gamma\delta} b_{\alpha\beta} b_{\gamma\delta} \sqrt{|\bar{g}|} dA, \\ \tilde{\epsilon}_{\alpha\beta} = \frac{1}{2}(a_{\alpha\beta} - \bar{g}_{\alpha\beta}), \quad (4.2)$$

where t is the sheet thickness, the integral is over the unstrained area, and $\tilde{\epsilon}_{\alpha\beta}$ is the ESK two-dimensional strain tensor.

Arguably, the functional in Eq. (4.1) represents the simplest covariant theory of incompatible elasticity. It makes a certain choice of strain tensor, which is based on the relative deviations of the distances *squared* from their rest values (the so-called Green–St. Venant strain tensor [68, 149, 150]). In elasticity theory the strain measure is regarded as a parametrization freedom—so long as the stress tensor (and resulting energy functional) is appropriately defined, different definitions of the strain tensor will lead to the same equilibrium deformation of the elastic body [150, Sec. 2.5]. Indeed, other choices of strain have been made in compatible elasticity, such as the Biot strain tensor [151], which expresses the spring-like deviations of distances within the body. Generally, one can write a dimensionless deviation of a certain variable ℓ from its reference ℓ_0 as $\Delta = \frac{1}{m\ell_0^m} (\ell^m - \ell_0^m)$, where m is an arbitrary number [149, p. 6]. In the limit of

small deviations, $\Delta \ll 1$, one always gets $\Delta \simeq (\ell - \ell_0)/\ell_0$ for any m . Thus, it seems that within linear elasticity of infinitesimal strains the choice of m is immaterial.

Dimensional reduction of 3D linear elasticity to 2D thin sheets introduces non-quadratic terms in the reduced energy functional. As we shall see below, a different selection of the strain tensor for the 3D body—the incompatible analogue of Biot’s strain—leads to non-quadratic terms in 2D which differ from those obtained from Eq. (4.2). Thus, the resulting theory is not equivalent to the ESK one. This holds even in the case of a compatible sheet with a flat reference metric [17, 152]. The differences between the two formulations are quantitatively small but have a qualitative effect on the structure of the theory and the simplicity of its application. We note that the present work is not the first to indicate the effect of strain-tensor selection. Similar observations were made in the context of compatible beam theory [29].

We begin in Sec. 4.2 by presenting the alternative formulation based on Biot’s selection of 3D strain. We perform a reduction to 2D, which is limited to axisymmetric surface deformations along the principal axes of stress. In Sec. 4.3 we apply the formulation to the simple example of a compatible sheet that is uniaxially bent by boundary moments. We show that it coincides in this case with the extensible elastica, yielding a bent, unstrained, cylindrical shape, whereas the choice made in Eq. (4.2) gives a cylinder with non-zero in-plane strain. Section 4.4 presents further applications to several examples of incompatible flat discs. We derive linear equations of equilibrium, and obtain their analytical solutions, for problems which are described by nonlinear equations in the ESK theory. Section 4.5 presents a self-consistency criterion, based on the alternative formulation, for the stability of axisymmetric strain-free configurations (isometric immersions) of such discs with respect to internal bending moments. We apply the criterion to the case of a reference metric with constant positive Gaussian curvature, whose isometric immersion is a spherical cap. In Sec. 4.6 we conclude and discuss future extensions of this work.

4.2 Alternative two-dimensional formulation for simple deformations

We impose three requirements on the alternative formulation for 2D incompatible sheets: (a) It should be invariant under rigid transformations (rotations and translations). (b) In the limit of incompressible compatible sheets it should converge to the known Willmore functional [68]. (c) In the small-slope approximation it should converge to the Föppl-von Kàrmàn (FvK) theory

(see Sec. 1.3.1) [19].

The formulation presented here holds for a small subset of problems which we can treat exactly. We consider a disc-like thin sheet of radius R , and parametrize it by the in-plane polar coordinates (r, θ) . The relaxed length, squared, of a line element on the sheet is given by the following reference metric,

$$\bar{g}_{\alpha\beta} = \begin{pmatrix} 1 & 0 \\ 0 & \Phi^2(r) \end{pmatrix}, \quad ds^2 = dr^2 + \Phi^2(r)d\theta^2, \quad (4.3)$$

where dr is the relaxed arclength element along the radial direction and $2\pi\Phi(r)$ is the relaxed perimeter of a circle of radius r around the disc center. Once $\Phi(r) \neq r$ the flat configuration contains internal strains. While such a sheet may have a complicated equilibrium deformation, we restrict ourselves to surfaces of revolution. The 3D position of a displaced point on the surface is given by

$$\mathbf{f}(r, \theta) = [r + u_r(r)]\hat{\mathbf{r}} + \zeta(r)\hat{\mathbf{z}}, \quad (4.4)$$

where u_r is the radial displacement, ζ is the height function, $\hat{\mathbf{r}}$ is a unit vector tangent to the sheet in the radial direction, and $\hat{\mathbf{z}}$ is a unit vector in the perpendicular direction to the flat disc. Note that, for an incompatible sheet, the case of $u_r(r) = \zeta(r) = 0$ does not correspond to a stress-free configuration.

The 2D energy functional of this system can be derived out of a 3D formulation using the Kirchhoff-Love hypothesis [15, 17, 22, 33, 68, 140]; see Chapter 1, Sec. 1.1.2. For this purpose we identify the 2D sheet defined above with the mid-surface of a 3D slab. Under the Kirchhoff-Love set of assumptions the configuration of the 3D body is given by,

$$\mathbf{f}^*(r, \theta, x_3) = \mathbf{f}(r, \theta) + x_3\hat{\mathbf{n}}(r, \theta), \quad (4.5)$$

where $x_3 \in [-t/2, t/2]$ is a coordinate in the direction $\hat{\mathbf{n}}$ normal to the mid-surface,

$$\hat{\mathbf{n}} = \frac{\partial_r \mathbf{f} \times \partial_\theta \mathbf{f}}{|\partial_r \mathbf{f} \times \partial_\theta \mathbf{f}|} = \frac{(1 + \partial_r u_r)\hat{\mathbf{z}} - \partial_r \zeta \hat{\mathbf{r}}}{\sqrt{(1 + \partial_r u_r)^2 + (\partial_r \zeta)^2}}. \quad (4.6)$$

On a surface of constant x_3 , the length squared of an infinitesimal line element is found, after some algebra, to be,

$$d\mathbf{f}^{*2} = [a_{rr} - 2x_3 b_{rr} + x_3^2 c_{rr}] dr^2 + [a_{\theta\theta} - 2x_3 b_{\theta\theta} + x_3^2 c_{\theta\theta}] d\theta^2, \quad (4.7)$$

where $a_{\alpha\beta} = \partial_\alpha \mathbf{f} \cdot \partial_\beta \mathbf{f}$, $b_{\alpha\beta} = -\partial_\alpha \mathbf{f} \cdot \partial_\beta \hat{\mathbf{n}}$, and $c_{\alpha\beta} = \partial_\alpha \hat{\mathbf{n}} \cdot \partial_\beta \hat{\mathbf{n}}$, are the first, second, and third fundamental forms.

On the other hand, following Biot's approach [151, p. 17], a pure deformation of that surface is represented by the symmetric transformation matrix,

$$\begin{pmatrix} dr' \\ \Phi d\theta' \end{pmatrix} = \begin{pmatrix} 1 + \epsilon_{rr}^* & \epsilon_{r\theta}^* \\ \epsilon_{r\theta}^* & 1 + \epsilon_{\theta\theta}^* \end{pmatrix} \begin{pmatrix} dr \\ \Phi d\theta \end{pmatrix}, \quad (4.8)$$

where $\epsilon_{\alpha\beta}^*$ is the in-plane strain tensor of the constant- x_3 surface. Note that this definition of the strain corresponds to changes in length (not length squared). Thus,

$$\begin{aligned} d\mathbf{f}^{*2} &= dr'^2 + (\Phi d\theta')^2 \\ &= [(1 + \epsilon_{rr}^*)^2 + (\epsilon_{r\theta}^*)^2] dr^2 + [(1 + \epsilon_{\theta\theta}^*)^2 + (\epsilon_{r\theta}^*)^2] (\Phi d\theta)^2 + 2\epsilon_{r\theta}^*(2 + \epsilon_{rr}^* + \epsilon_{\theta\theta}^*)\Phi d\theta dr. \end{aligned} \quad (4.9)$$

Comparing Eqs. (4.7) and (4.9), we identify,

$$\epsilon_{rr}^* = \sqrt{(1 + \epsilon_{rr})^2 - 2x_3 b_{rr} + x_3^2 c_{rr}} - 1, \quad (4.10a)$$

$$\epsilon_{\theta\theta}^* = \sqrt{(1 + \epsilon_{\theta\theta})^2 - 2x_3 b_{\theta\theta}/\Phi^2 + x_3^2 c_{\theta\theta}/\Phi^2} - 1, \quad (4.10b)$$

$$\epsilon_{r\theta}^* = 0, \quad (4.10c)$$

where

$$\epsilon_{rr} = \sqrt{a_{rr}} - 1 = \sqrt{(1 + \partial_r u_r)^2 + (\partial_r \zeta)^2} - 1, \quad (4.11a)$$

$$\epsilon_{\theta\theta} = \sqrt{a_{\theta\theta}}/\Phi - 1 = \frac{r}{\Phi} - 1 + \frac{u_r}{\Phi}. \quad (4.11b)$$

We have reached a definition of the mid-surface in-plane strains in terms of the actual and reference metrics, based on the spring-like deformed length rather than length squared.

The geometrical interpretation of these strains is illustrated in Fig. 4.1. The fact that the strains describe deformed lengths [15, p. 41] leads at this stage to two simplifications. First, the fundamental forms satisfy the simple relations, $c_{rr} = b_{rr}^2/(1 + \epsilon_{rr})^2$ and $\Phi^2 c_{\theta\theta} = b_{\theta\theta}^2/(1 + \epsilon_{\theta\theta})^2$. Second, once these expressions are substituted in Eqs. (4.10), we can rewrite the strains at constant x_3 as,

$$\epsilon_{rr}^* = \epsilon_{rr} - x_3 \phi_{rr}, \quad (4.12a)$$

$$\epsilon_{\theta\theta}^* = \epsilon_{\theta\theta} - x_3 \phi_{\theta\theta}. \quad (4.12b)$$

(See Fig. 4.1c for the geometrical meaning of these strains.) Here we have defined the out-of-plane strains,

$$\phi_{rr} = \sqrt{c_{rr}} = \frac{(1 + \partial_r u_r) \partial_{rr} \zeta - \partial_{rr} u_r \partial_r \zeta}{(1 + \partial_r u_r)^2 + (\partial_r \zeta)^2}, \quad (4.13a)$$

$$\phi_{\theta\theta} = \sqrt{c_{\theta\theta}}/\Phi = \frac{1}{\Phi} \frac{\partial_r \zeta}{\sqrt{(1 + \partial_r u_r)^2 + (\partial_r \zeta)^2}}. \quad (4.13b)$$

Defining further ϕ^r and ϕ^θ as the tangent angles in the radial and azimuthal directions of the surface of revolution, we find $\phi_{rr} = \partial_r \phi^r$ and $\phi_{\theta\theta} = (1/\Phi)\partial_\theta \phi^\theta$ (see Fig. 4.1(a) and the explanation in its caption). This clarifies the geometrical meaning of the “bending-strains”, ϕ_{rr} and $\phi_{\theta\theta}$.

In the framework of linear elasticity the energy functional of the 3D slab is given by [19],

$$E_{3D} = \frac{E}{2(1-\nu^2)} \int_{-t/2}^{t/2} \int_0^R \int_0^{2\pi} [(\epsilon_{rr}^*)^2 + (\epsilon_{\theta\theta}^*)^2 + 2\nu\epsilon_{rr}^*\epsilon_{\theta\theta}^*] \Phi d\theta dr dx_3, \quad (4.14)$$

where E is Young’s modulus and ν the Poisson ratio. Substituting Eqs. (4.12) in (4.14) and integrating over x_3 gives,

$$E_{2D} = \frac{Y}{2} \int_0^R \int_0^{2\pi} [\epsilon_{rr}^2 + \epsilon_{\theta\theta}^2 + 2\nu\epsilon_{rr}\epsilon_{\theta\theta}] \Phi d\theta dr + \frac{B}{2} \int_0^R \int_0^{2\pi} [\phi_{rr}^2 + \phi_{\theta\theta}^2 + 2\nu\phi_{rr}\phi_{\theta\theta}] \Phi d\theta dr, \quad (4.15)$$

where $Y = Et/(1-\nu^2)$ is the stretching modulus and $B = Et^3/12(1-\nu^2)$ is the bending modulus. The first integral in Eq. (4.15) is the stretching energy,

$$E_s = \frac{1}{2} \int_0^R \int_0^{2\pi} [\sigma_{rr}\epsilon_{rr} + \sigma_{\theta\theta}\epsilon_{\theta\theta}] \Phi d\theta dr, \quad (4.16)$$

where the stress components $\sigma_{\alpha\beta} = \delta E/\delta\epsilon_{\alpha\beta}$ are given by,

$$\sigma_{rr} = Y(\epsilon_{rr} + \nu\epsilon_{\theta\theta}), \quad (4.17a)$$

$$\sigma_{\theta\theta} = Y(\epsilon_{\theta\theta} + \nu\epsilon_{rr}). \quad (4.17b)$$

Similarly, the second integral in Eq. (4.15) gives the bending energy,

$$E_b = \frac{1}{2} \int_0^R \int_0^{2\pi} [M_{rr}\phi_{rr} + M_{\theta\theta}\phi_{\theta\theta}] \Phi d\theta dr, \quad (4.18)$$

where the bending moments, $M_{\alpha\beta} = \delta E/\delta\phi_{\alpha\beta}$, in the radial and azimuthal directions are given by,

$$M_{rr} = B(\phi_{rr} + \nu\phi_{\theta\theta}), \quad (4.19a)$$

$$M_{\theta\theta} = B(\phi_{\theta\theta} + \nu\phi_{rr}). \quad (4.19b)$$

Looking back at the dimensional reduction just performed, we see why a generalization from axisymmetric deformations to general ones, although possible, is going to be much more cumbersome.

Let us now verify that the three requirements that we have imposed on the energy functional are fulfilled by Eq. (4.15). The first requirement, of invariance under rigid transformations, is

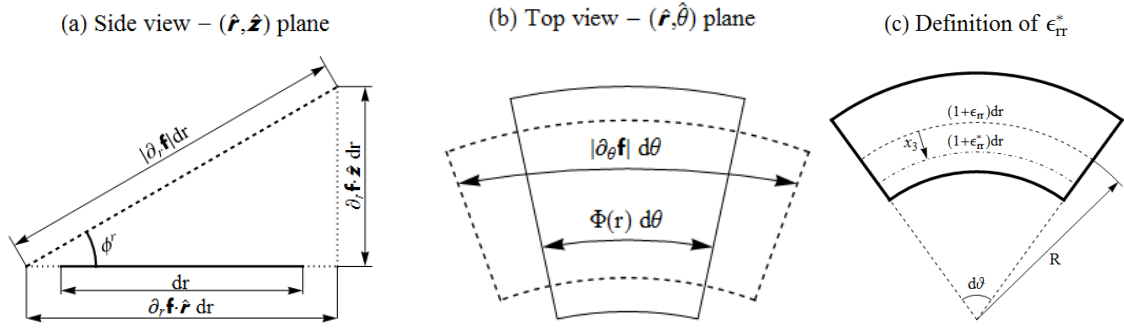


Figure 4.1: (a) Deformation of an infinitesimal element in the radial direction. The relaxed length of the element is dr (solid line), and the deformed length is $|\partial_r \mathbf{f}| dr$. The radial strain component is $\epsilon_{rr} = \frac{|\partial_r \mathbf{f}| dr - dr}{dr}$, as given by Eq. (4.11a). The angle ϕ^r satisfies $\sin \phi^r = \partial_r \mathbf{f} \cdot \hat{\mathbf{z}} / |\partial_r \mathbf{f}|$. Substituting $\mathbf{f}(r, \theta)$ from Eq. (4.4) in the latter relation and using Eq. (4.13b) gives $\phi_{\theta\theta} = \sin \phi^r / \Phi$. In addition, by direct differentiation it can be verified that $\phi_{rr} = \partial_r \phi^r$ as given by Eq. (4.13a). (b) Deformation of an infinitesimal sheet element in the azimuthal direction. The relaxed length in this direction is $\Phi d\theta$ (solid line) and the deformed length is $|\partial_\theta \mathbf{f}| d\theta$ (dashed line). Thus, the azimuthal strain is $\epsilon_{\theta\theta} = \frac{|\partial_\theta \mathbf{f}| d\theta - \Phi d\theta}{\Phi d\theta}$, as given by Eq. (4.11b). (c) Deformation of an infinitesimal line element in the radial direction at height x_3 below the mid-surface. By geometry, the shown angle $d\theta = (1 + \epsilon_{rr}) dr / R = (1 + \epsilon_{rr}^*) dr / (R - x_3)$. Using $1/R = (1 + \epsilon_{rr})^{-1} d\phi^r / dr$ and solving for ϵ_{rr}^* gives Eq. (4.12a).

satisfied, since the strains have been derived from a pure deformation matrix, Eq. (4.8), as discussed in the first chapter of Ref. [151]. Equivalently, Eqs. (4.16) and (4.18) can be rewritten in terms of the tensor invariants,

$$E_s = \frac{Y}{2} \int_0^R \int_0^{2\pi} [\text{tr}(\epsilon)^2 - 2(1 - \nu) \det(\epsilon)] \sqrt{|\bar{g}|} d\theta dr,$$

$$E_b = \frac{B}{2} \int_0^R \int_0^{2\pi} [\text{tr}(\bar{g}^{-1}c) + 2\nu \sqrt{\det(\bar{g}^{-1}c)}] \sqrt{|\bar{g}|} d\theta dr,$$

which is manifestly invariant to rigid transformations.

To verify the second requirement, we take the incompressible limit, $a_{\alpha\beta} \rightarrow \bar{g}_{\alpha\beta}$, and obtain $E_s = 0$, $\phi_{rr}^2 \rightarrow \kappa_{rr}^2$ and $\phi_{\theta\theta}^2 \rightarrow \kappa_{\theta\theta}^2$, where κ_{rr} and $\kappa_{\theta\theta}$ are the two principal curvatures on the surface in the radial and azimuthal directions. Substituting the latter relations in the second integral of Eq. (4.15), we obtain,

$$\text{Incompressible sheet: } E_b = \frac{B}{2} \int_0^R \int_0^{2\pi} ((\kappa_{rr} + \kappa_{\theta\theta})^2 - 2(1 - \nu) \kappa_{rr} \kappa_{\theta\theta}) \Phi dr d\theta, \quad (4.20)$$

which coincides with the known Willmore functional [68].

Lastly, we verify the third requirement, that for compatible sheets in the small-slope ap-

proximation our model converges to the FvK theory (cf. Sec. 1.3.1) [19]. Setting $\Phi = r$ and expanding the in-plane strain, Eqs. (4.11), to linear order in u_r and quadratic order in ζ , we have $\epsilon_{rr} \simeq \partial_r u_r + \frac{1}{2}(\partial_r \zeta)^2$ and $\epsilon_{\theta\theta} = u_r/r$. The latter strains along with Eq. (4.16) yield the stretching energy in the FvK approximation [153]. Similarly, the “bending strains”, Eqs. (4.13), are approximated by $\phi_{rr} \simeq \partial_{rr} \zeta$ and $\phi_{\theta\theta} \simeq \partial_r \zeta/r$. Substituting these in Eq. (4.18), we obtain the FvK bending energy,

$$\text{Small slope: } E_b \simeq \frac{B}{2} \int_0^R \int_0^{2\pi} [(\nabla_r^2 \zeta)^2 - 2(1-\nu)[\zeta, \zeta]] r dr d\theta, \quad (4.21)$$

where $\nabla_r^2 \zeta \equiv \frac{1}{r} \partial_r (r \partial_r \zeta)$ and $[\zeta, \zeta] \equiv \frac{1}{r} \partial_r \zeta \partial_{rr} \zeta$ are the small-slope approximations of the mean and Gaussian curvatures.

4.3 Uniaxial deformation by bending

We would like to demonstrate the difference between the ESK model and the one presented in the preceding section, using the simplest example possible. Consider the uniaxial deformation of a compatible sheet by bending moments applied at its edges. Alternatively, we can replace the moments by purely geometrical boundary conditions on the configuration at the edges, as given below. Since no in-plane axial forces are applied, a particularly simple possibility is a purely bent cylindrical deformation of the sheet’s midplane—an isometry which contains no stretching energy (Fig. 4.2). Indeed, this is the deformation obtained in this case from the theory of extensible elastica [28, 31, 32, 34], as we recall below.

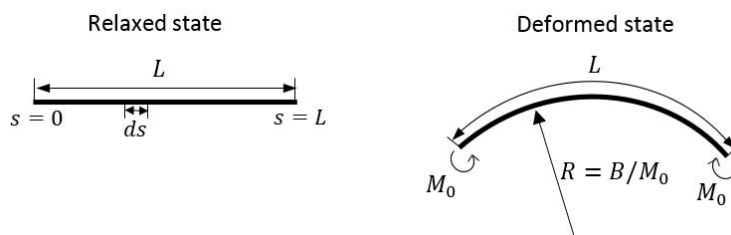


Figure 4.2: A flat thin sheet is deformed into a cylinder of constant radius without stretching of its midplane. This deformation is obtained for the extensible elastica by applying bending moments, M_0 , on the sheet edges or by imposing $d\phi/ds$ at the boundaries.

To apply the formulation to this simple problem we should reduce the 2D energy, Eq. (4.15), to 1D. Consider a radial cut of a θ -independent deformation as a planar compatible filament ($\Phi(r) = 1$). Identify $r \rightarrow s$, where $s \in [0, L]$ is the undeformed arclength along the filament, and $\phi^r(r) \rightarrow \phi(s)$, the angle between the tangent to the filament and the flat reference plane. We

then have $\phi_{rr}^2 \rightarrow \phi_{ss}^2 = (d\phi/ds)^2$, $\epsilon_{rr} \rightarrow \epsilon_{ss}$, and $\phi_{\theta\theta} = \epsilon_{\theta\theta} = 0$. Substitution of these relations in Eq. (4.15) gives,

$$E_{1D} = E_s + E_b = \int_0^L \left[\frac{Y}{2} \epsilon_{ss}^2 + \frac{B}{2} \left(\frac{d\phi}{ds} \right)^2 \right] ds. \quad (4.22)$$

This functional coincides with the energy of an extensible elastic filament in a planar deformation as given by the theory of extensible elastica [28, 31, 32, 34], see also Eq. (1.9) in Sec. 1.2.1.

Alternatively, we could reduce the sheet into a filament through an azimuthal cut along a narrow annulus of large radius ρ , in which case $d\theta \rightarrow ds$, $\phi_{\theta\theta}^2 \rightarrow \phi_{ss} = (d\phi/(\Phi ds))^2$, and $\phi_{rr} = \epsilon_{rr} = 0$. We then obtain

$$E_{1D} = E_s + E_b = \int_0^{L'} \left[\frac{Y}{2} \epsilon_{ss}^2 + \frac{B}{2} \left(\frac{d\phi}{\Phi ds} \right)^2 \right] \Phi ds. \quad (4.23)$$

The parameter s now runs between 0 and L' , such that $L = \int_0^{L'} \Phi ds$ is the total relaxed length. In addition, ϵ_{ss} now measures the in-plane strain with respect to the prescribed metric. The energy of Eq. (4.23) is the extension of the extensible elastica theory to the case of a nontrivial reference metric.

Returning to the ordinary extensible elastica, we note that Eq. (4.22) can be derived from a discrete model of springs and joints [32] while enforcing from the outset the decoupling between the stretching and bending contributions [33, p. 77]; see Chapter 3, Sec. 3.2. In Eq. (4.22) this decoupling is manifest in the independence of E_s on ϕ , $\frac{\delta E_s}{\delta \phi} = 0$, while E_b is independent of ϵ_{ss} , $\frac{\delta E_b}{\delta \epsilon_{ss}} = 0$. In the absence of boundary axial forces, the equations of equilibrium are obtained from minimization of Eq. (4.22). Defining the in-plane stress (acting to only locally stretch the filament) and bending moment (acting only to change its local angle) as,

$$\sigma_{ss} \equiv \frac{\delta E_{1D}}{\delta \epsilon_{ss}} = Y \epsilon_{ss}, \quad (4.24a)$$

$$M_{ss} \equiv \frac{\delta E_{1D}}{\delta \left(\frac{d\phi}{ds} \right)} = B \frac{d\phi}{ds}, \quad (4.24b)$$

those equations of equilibrium are,

$$\sigma_{ss} = 0, \quad (4.25a)$$

$$\frac{dM_{ss}}{ds} = 0. \quad (4.25b)$$

When a constant moment, M_0 , is applied at the boundaries (Fig. 4.2), Eqs. (4.24)–(4.25) yield $\epsilon_{ss} = 0$ and $\phi(s) = \phi(0) + (M_0/B)s$. This solution corresponds to a circular arc of radius B/M_0 and total length L . Alternatively, if we impose $(d\phi/ds)|_{s=0} = c$, we get $\phi(s) =$

$\phi(0) + cs$, corresponding to a circular arc of radius $1/c$. The energy of this configuration is $E_{1D} = (B/2)c^2L$.

The strain-free cylindrical shape is preserved also in the more complicated case of a nonuniform reference metric, Eq. (4.23). Variation of this energy with respect to ϵ_{ss} and ϕ gives, as before, Eqs. (4.25), where the in-plane stress is given again by Eq. (4.24a). The bending moment is modified to,

$$M_{ss} = \frac{\delta E_{1D}}{\delta \left(\frac{1}{\Phi} \frac{d\phi}{ds} \right)} = \frac{B}{\Phi} \frac{d\phi}{ds}, \quad (4.26)$$

which replaces Eq. (4.24b). The in-plane strain (with respect to the reference metric) vanishes. When we apply a moment M_0 at the boundaries, or impose $(d\phi/(\Phi ds))|_{s=0} = c$, we find again a strain-free cylindrical shape with radius B/M_0 , or $1/c$.

We now show that the ESK functional gives a different result. We specialize Eq. (4.2) to the case of a compatible sheet under uniaxial deformation. Since the deformation has zero Gaussian curvature, we set $\bar{g}_{ss} = 1$ and, from Eq. (4.2), obtain $a_{ss} = 1 + 2\tilde{\epsilon}_{ss}$. In addition, we have $\sqrt{|\bar{g}|}dA \rightarrow ds$, $t\mathcal{A}^{ssss} \rightarrow Y$, and $\frac{t^3}{12}\mathcal{A}^{ssss} \rightarrow B$. Substituting these relations in Eq. (4.2) gives

$$\text{ESK: } E_{1D} = \int_0^L \left(\frac{Y}{2} \tilde{\epsilon}_{ss}^2 + \frac{B}{2} b_{ss}^2 \right) ds. \quad (4.27)$$

The relations between the variables appearing in the ESK Eq. (4.27) and the ones in Eq. (4.22) are $\tilde{\epsilon}_{ss} = \epsilon_{ss}(1 + \epsilon_{ss}/2)$, and $b_{ss} = \partial_s(\sqrt{a_{ss}}\hat{\mathbf{t}}) \cdot \hat{\mathbf{n}} = (1 + 2\tilde{\epsilon}_{ss})^{1/2} \frac{d\phi}{ds}$.

Naively, if we set the variations of the energy (4.27) with respect to $\tilde{\epsilon}_{ss}$ and b_{ss} to zero, we will get the same result as above, i.e., a strain-free circular configuration with $\tilde{\epsilon}_{ss} = 0$, $b_{ss} = (d\phi/ds)_{s=0} = c$, and energy $E_{1D} = (B/2)c^2L$. Thus, the coupling between $\tilde{\epsilon}_{ss}$ and $d\phi/ds$ appearing in $b_{ss} = (1 + 2\tilde{\epsilon}_{ss})^{1/2} \frac{d\phi}{ds}$ would not have an effect on the configuration. However, the correct minimization is with respect to the filament's trajectory $\mathbf{f}(s)$. As shown in Appendix C.1, this is equivalent to the minimization with respect to ϵ_{ss} and ϕ . In terms of these variables, Eq. (4.27) becomes

$$\text{ESK: } E_{1D} = \int_0^L \left[\frac{Y}{2} [\epsilon_{ss}(1 + \epsilon_{ss}/2)]^2 + \frac{B}{2} [1 + 2\epsilon_{ss}(1 + \epsilon_{ss}/2)] \left(\frac{d\phi}{ds} \right)^2 \right] ds. \quad (4.28)$$

The bending contribution to this energy depends on ϵ_{ss} , which results in a strained configuration under the boundary conditions given above. Specifically, minimization of the energy in Eq. (4.28) with respect to ϵ_{ss} and ϕ , under the boundary condition $(d\phi/ds)_{s=0} = c$, yields a circular arc, $\phi(s) = \phi(0) + cs$, which nonetheless contains non-zero strain, $\epsilon_{ss} = \sqrt{1 - 2Bc^2/Y} - 1$.

The energy of this configuration is $E_{1D} = (B/2)c^2L[1 - (B/Y)c^2]$, slightly deviating from the energy of the extensible elastica obtained above.

Two comments should be added concerning the difference between the two models. (a) As demonstrated by the case of a geometrical boundary condition on $d\phi/ds$, the difference does not arise from different definitions of the boundary bending moment. (This remains correct if we impose the condition on the *apparent* curvature, $[d\phi/d(1 + \epsilon_{ss})s]_{s=0}$.) (b) In Ref. [68] a term proportional to $\tilde{\epsilon}_{ss}(d\phi/ds)^2$ was neglected in the final step. Clearly, its inclusion merely changes the numerical coefficient in the second term of Eq. (4.28).

In summary, unlike the formulation of Sec. 4.2, the ESK model does not strictly reduce to the extensible elastica. Under uniaxial bending at the boundaries it produces a small in-plane strain, while our formulation and the extensible elastica predict a strain-free cylindrical shape. The discrepancy is small and vanishes in the incompressible limit of $B/Y \rightarrow 0$. Moreover, the correction terms are of order $(B/Y)c^2 \sim (tc)^2$, which must always be small in any elasticity theory of sheets of finite thickness. Nevertheless, the effect of the coupling between stress and bending moments goes beyond this simple 1D example and profoundly affects the structure of the theory, as will be shown in the following sections.

4.4 Exact solutions for planar deformations of incompatible sheets

We now demonstrate the advantage of the alternative formulation in simple examples of flat configurations. In the flat state the bending energy is zero and the equation of equilibrium is obtained by minimizing the stretching energy alone. To do so we first set $\zeta = 0$ in Eqs. (4.11),

$$\epsilon_{rr} = \partial_r u_r, \quad (4.29a)$$

$$\epsilon_{\theta\theta} = \frac{r}{\Phi} - 1 + \frac{u_r}{\Phi}, \quad (4.29b)$$

and then substitute Eqs. (4.29) in (4.16), obtaining,

$$E_s = \frac{1}{2} \int_0^R \int_0^{2\pi} \left[\sigma_{rr} \partial_r u_r + \sigma_{\theta\theta} \left(\frac{r}{\Phi} - 1 + \frac{u_r}{\Phi} \right) \right] \Phi d\theta dr. \quad (4.30)$$

Minimization of E_s with respect to u_r gives the equation of equilibrium,

$$\partial_r(\Phi \sigma_{rr}) - \sigma_{\theta\theta} = 0, \quad (4.31)$$

which expresses balance of forces in the radial direction (see Fig. 4.3). Substituting the in-plane strains, Eqs. (4.29), in the stress components, Eqs. (4.17), and then in (4.31), we obtain the

equation of equilibrium in terms of u_r alone,

$$\Phi \partial_r (\Phi \partial_r u_r) - u_r = r - \Phi - \nu \Phi (1 - \partial_r \Phi). \quad (4.32)$$

This second-order equation for u_r is supplemented by two boundary conditions: vanishing stress at the free edge, $\sigma_{rr}|_{r=R} = 0$ and vanishing displacement at the origin. The resulting conditions are

$$[\Phi \partial_r u_r + \nu u_r + \nu (r - \Phi)]_{r=R} = 0, \quad (4.33a)$$

$$u_r|_{r=0} = 0. \quad (4.33b)$$

Importantly, unlike earlier analysis of the same problem [78], Eqs. (4.32) and (4.33) are *linear* and therefore solvable. To demonstrate this key advantage we now derive exact solutions of Eq. (4.32) for three types of reference metrics: flat, elliptic, and hyperbolic (see Fig. 4.4). In

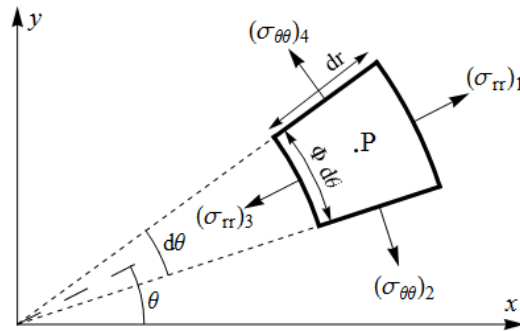


Figure 4.3: Radial force balance on an infinitesimal element of a flat sheet [154, p. 65]. At the point P we have contributions from the two radial stresses, $(\sigma_{rr})_1 \Phi d\theta$ and $-(\sigma_{rr})_3 \Phi d\theta$, and from the two azimuthal stresses $-(\sigma_{\theta\theta})_2 dr \sin(d\theta/2)$ and $-(\sigma_{\theta\theta})_4 dr \sin(d\theta/2)$. Balancing these terms gives Eq. (4.31).

the following subsections we compare the results obtained from analytical solutions of our model for the different reference metrics with those obtained from the ESK nonlinear equations. To assure a meaningful comparison we examine the following: (a) the radial displacement u_r , which is an unambiguous experimental observable; (b) the stress components obtained by variation of the energy with respect to the strain ϵ (not the metric-based one, $\tilde{\epsilon}$) for *both* models. In Appendix C.4 we elaborate on the relations between these stress tensors in the two theories.

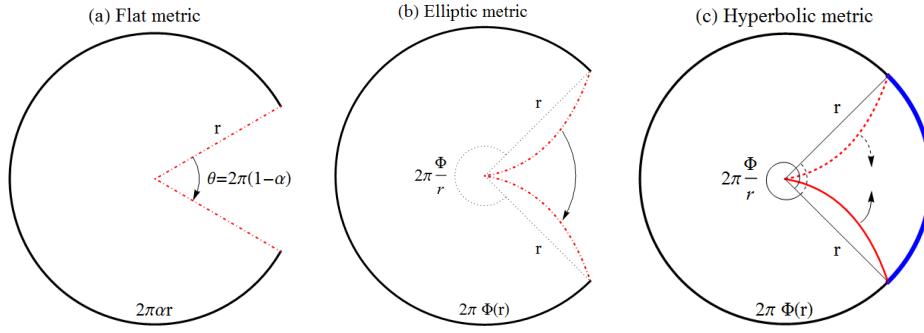


Figure 4.4: Layouts of the three considered reference metrics. (a) Flat metric, Eq. (4.34). When the two radii (dash-dotted red lines) are held together, the rest length of concentric circles on the closed disc become $2\pi\alpha r < 2\pi r$. (b) Elliptic metric, Eq. (4.40). Gluing together the two curved dash-dotted red lines creates a frustrated disc, where concentric circles have rest length of $2\pi\Phi(r) < 2\pi r$. (c) Hyperbolic metric, Eq. (4.47). In this panel dashing represents unseen lines; concentric circles have rest length $2\pi\Phi(r) > 2\pi r$, causing pieces of the disc to be placed in the relaxed configuration one over the other (marked in blue). Attaching together the lower (hidden) red-dashed line with the upper solid red line results in a disc with a hyperbolic metric.

4.4.1 Flat metric

A flat reference metric is given by,

$$\Phi(r) = \alpha r, \quad (4.34)$$

where $\alpha < 1$. Substituting Eq. (4.34) in (4.32) and (4.33a) gives,

$$\alpha^2 r \partial_r (r \partial_r u_r) - u_r = (1 - \alpha)(1 - \nu\alpha)r, \quad (4.35a)$$

$$[\alpha r \partial_r u_r + \nu u_r + \nu(1 - \alpha)r]_{r=R} = 0. \quad (4.35b)$$

Equation (4.35a) replaces the nonlinear Eq. (10) of Ref. [78] which could be solved only numerically. The solution to Eq. (4.35a) is given by,

$$u_r(r) = A_0 r^{1/\alpha} + B_0 r^{-1/\alpha} - \frac{1 - \alpha\nu}{1 + \alpha} r, \quad (4.36)$$

where A_0 and B_0 are constants to be determined by boundary conditions. The vanishing displacement at the disc center, Eq. (4.33b), is satisfied for $B_0 = 0$. The value of A_0 is determined by the second boundary condition, (4.35b). This gives,

$$u_r(r) = -\frac{1 - \alpha\nu}{1 + \alpha} \left[1 - \frac{(1 - \nu)\alpha}{1 - \alpha\nu} \left(\frac{r}{R} \right)^{\frac{1}{\alpha} - 1} \right] r. \quad (4.37)$$

Substituting Eq. (4.37) in Eqs. (4.29) and then in Eqs. (4.17), we obtain the radial and

azimuthal stress components,

$$\sigma_{rr}(r) = -\frac{Et}{1+\alpha} \left[1 - \left(\frac{r}{R} \right)^{\frac{1}{\alpha}-1} \right], \quad (4.38a)$$

$$\sigma_{\theta\theta}(r) = -\frac{Et}{1+\alpha} \left[\alpha - \left(\frac{r}{R} \right)^{\frac{1}{\alpha}-1} \right]. \quad (4.38b)$$

Note that the stress components do not depend on ν . Note also that the azimuthal stress becomes positive at $r_{cr} = \alpha^{\alpha/(1-\alpha)}R$, whereas the radial one is always negative. The problem can be solved for other boundary conditions, e.g., for an annulus with inner radius R_i and outer radius R_o , and with free boundary conditions at its two rims. The solution reads,

$$u_r = \frac{\alpha(1-\nu)}{1+\alpha} \left[\frac{1-\rho^{\frac{1}{\alpha}+1}}{1-\rho^{2/\alpha}} \left(\frac{r}{R_o} \right)^{\frac{1}{\alpha}-1} - \frac{1+\nu}{1-\nu} \frac{1-\rho^{\frac{1}{\alpha}-1}}{1-\rho^{2/\alpha}} \left(\frac{R_i}{r} \right)^{\frac{1}{\alpha}+1} - \frac{1-\nu\alpha}{\alpha(1-\nu)} \right] r, \quad (4.39a)$$

$$\sigma_{rr} = -\frac{Et}{1+\alpha} \left[1 - \frac{1-\rho^{\frac{1}{\alpha}+1}}{1-\rho^{2/\alpha}} \left(\frac{r}{R_o} \right)^{\frac{1}{\alpha}-1} - \frac{1-\rho^{\frac{1}{\alpha}-1}}{1-\rho^{2/\alpha}} \left(\frac{R_i}{r} \right)^{\frac{1}{\alpha}+1} \right], \quad (4.39b)$$

$$\sigma_{\theta\theta} = -\frac{Et}{1+\alpha} \left[\alpha - \frac{1-\rho^{\frac{1}{\alpha}+1}}{1-\rho^{2/\alpha}} \left(\frac{r}{R_o} \right)^{\frac{1}{\alpha}-1} + \frac{1-\rho^{\frac{1}{\alpha}-1}}{1-\rho^{2/\alpha}} \left(\frac{R_i}{r} \right)^{\frac{1}{\alpha}+1} \right], \quad (4.39c)$$

where $\rho \equiv R_i/R_o$. In Fig. 4.5 we compare the exact analytical solution for the radial displacement, Eq. (4.39a), with the numerical solution of the formalism given in Ref. [78]. The two theories converge to the same solution as $\alpha \rightarrow 1$. However, away from this nearly Euclidean regime there are significant differences in the resultant displacements. Since the displacement is an unambiguous observable, these differences underline the fact that the two formulations are not equivalent. Figure 4.6 presents a similar comparison of the plane stresses obtained from the two theories.

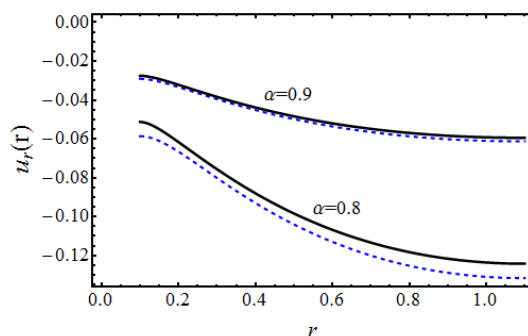


Figure 4.5: Comparison between the exact solution for the radial displacement (Eq. (4.39a); black, solid line) and the numerical solution of Eq. (10) in Ref. [78] (dashed, blue line) for a flat reference metric. We consider an annulus with inner and outer radii $R_i = 0.1$ and $R_o = 1.1$. In accordance with the example in Ref. [78], we use $\nu = 0$. The units of length are arbitrary so long as the same units are used for r and u_r (see Eqs. 4.39).

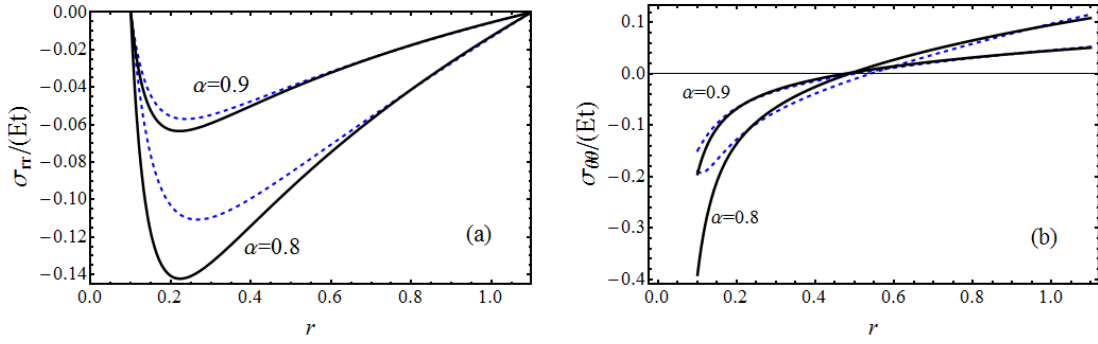


Figure 4.6: Comparison between the exact plane-stress solutions (Eqs. (4.39), black solid line) and the numerical solution of Eq. (10) in Ref. [78] (dashed blue line) for a flat reference metric. Parameters are as in Fig. 4.5.

4.4.2 Elliptic metric

An elliptic reference metric is given by,

$$\Phi(r) = \frac{1}{\sqrt{K}} \sin(\sqrt{K}r), \quad (4.40)$$

where K is a constant positive reference Gaussian curvature. Substituting Eq. (4.40) in Eqs. (4.32) and (4.33a) gives,

$$\sin(r)\partial_r(\sin(r)\partial_r u_r) - u_r = r - \sin(r) - \nu \sin(r)(1 - \cos(r)), \quad (4.41a)$$

$$[\sin(r)\partial_r u_r + \nu u_r + \nu(r - \sin(r))]_{r=R} = 0, \quad (4.41b)$$

where we have rescaled the lengths r and u_r by $K^{-1/2}$. The following expression is verified to be the general solution by direct substitution in Eq. (4.41a),

$$u_r(r) = A_0 \tan(r/2) + B_0 \cot(r/2) - r - 2(1 + \nu) \cot(r/2) \ln[\cos(r/2)]. \quad (4.42)$$

We set $B_0 = 0$ to satisfy the vanishing displacement at the disc center, Eq. (4.33b), and determine A_0 by the boundary condition (4.41b), obtaining,

$$u_r(r) = -r - 2(1 - \nu) \ln[\cos(R/2)] \cot^2(R/2) \left(1 + \frac{1 + \nu \cot^2(r/2) \ln[\cos(r/2)]}{1 - \nu \cot^2(R/2) \ln[\cos(R/2)]} \right) \tan(r/2). \quad (4.43)$$

Note that the solution diverges for $r = r_n = n\pi$ where n is a positive integer. At such points the reference metric, Eq. (4.40), vanishes, i.e., these divergencies correspond to unphysical cases where the rest length shrinks to zero. Substituting Eq. (4.43) in Eqs. (4.17), we obtain the

distributed stress on the disc,

$$\sigma_{rr}(r) = -Et \left(1 - \frac{\cot^2(r/2) \ln[\cos(r/2)]}{\cot^2(R/2) \ln[\cos(R/2)]} \right) \frac{\ln[\cos(R/2)] \cot^2(R/2)}{\cos^2(r/2)}, \quad (4.44a)$$

$$\sigma_{\theta\theta}(r) = -Et \left(1 + \frac{\ln[\cos(r/2)]}{\sin^2(r/2)} + \cot^2(R/2) \frac{\ln[\cos(R/2)]}{\cos^2(r/2)} \right). \quad (4.44b)$$

Once again, the solution is independent of the Poisson ratio.

In order to compare our exact solution to the numerical one obtained in Ref. [78], we also derive the displacement and the planar stress in an annulus with free boundary conditions. In this case the constants A_0 and B_0 in Eq. (4.42) are

$$A_0 = \frac{4(1-\nu)}{\cos(R_i) - \cos(R_o)} \cos^2(R_i/2) \cos^2(R_o/2) (\ln[\cos(R_i/2)] - \ln[\cos(R_o/2)]), \quad (4.45a)$$

$$B_0 = \frac{1+\nu}{\cos(R_i) - \cos(R_o)} \{ (1 + \cos(R_i))(1 - \cos(R_o)) \ln[\cos(R_i/2)] - (1 - \cos(R_i))(1 + \cos(R_o)) \ln[\cos(R_o/2)] \}, \quad (4.45b)$$

and the stress components become

$$\begin{aligned} \sigma_{rr} &= -2Et \left[1 + \left(1 - \frac{\cos(R_i) - \cos(R_o)}{\cos(r) - \cos(R_o)} \frac{\cos^2(r/2)}{\cos^2(R_i/2)} \frac{\ln[\cos(r/2)]}{\ln[\cos(R_i/2)]} \right) \right. \\ &\times \left. \frac{1 + \cos(R_i)}{1 + \cos(R_o)} \frac{\cos(r) - \cos(R_o)}{\cos(R_i) - \cos(r)} \frac{\ln[\cos(R_i/2)]}{\ln[\cos(R_o/2)]} \right] \frac{1 + \cos(R_o)}{\sin^2(r)} \frac{\cos(R_i) - \cos(r)}{\cos(R_i) - \cos(R_o)} \ln[\cos(R_o/2)], \end{aligned} \quad (4.46a)$$

$$\begin{aligned} \sigma_{\theta\theta} &= -Et \left[1 + \frac{\ln[\cos(r/2)]}{\sin^2(r/2)} + 4 \left(1 - \frac{\cos^2(R_i/2)}{\cos^2(R_o/2)} \frac{1 - \cos(R_o)}{1 - \cos(R_i)} \frac{\cos(r) \ln[\cos(R_i/2)]}{\ln[\cos(R_o/2)]} \right) \right. \\ &\times \left. \frac{\cos^2(R_o/2)}{\sin^2(r)} \frac{1 - \cos(R_i)}{\cos(R_i) - \cos(R_o)} \frac{\cos(r)}{\ln[\cos(R_o/2)]} \right]. \end{aligned} \quad (4.46b)$$

In Fig. 4.7 we compare the radial displacement obtained from this exact solution, Eqs. (4.42) and (4.45), to the numerical solution of Eq. (10) in Ref. [78]. In addition, Fig. 4.8 compares the radial and azimuthal stress components of the two models. The two solutions converge for a narrow annulus and differ significantly as the annulus becomes wider. (Note that increasing R_o is equivalent to increasing K .)

4.4.3 Hyperbolic metric

A hyperbolic reference metric is given by,

$$\Phi(r) = \frac{1}{\sqrt{K}} \sinh(\sqrt{K}r). \quad (4.47)$$

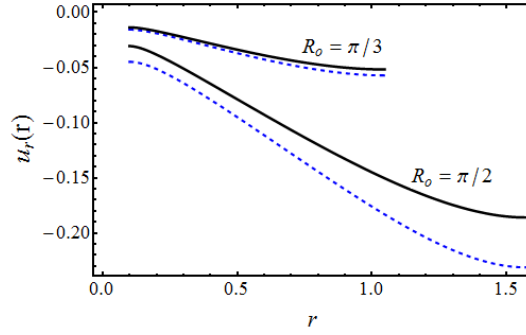


Figure 4.7: The exact solution for the radial displacement (Eqs. (4.42) and (4.45); black solid line) is plotted alongside the numerical solution of Eq. (10) in Ref. [78] (dashed blue line) for an elliptic reference metric. We consider an annulus with an inner radius $R_i = 0.1$, $\nu = 0$, and two different values of R_o as indicated. Lengths are normalized by $K^{-1/2}$.

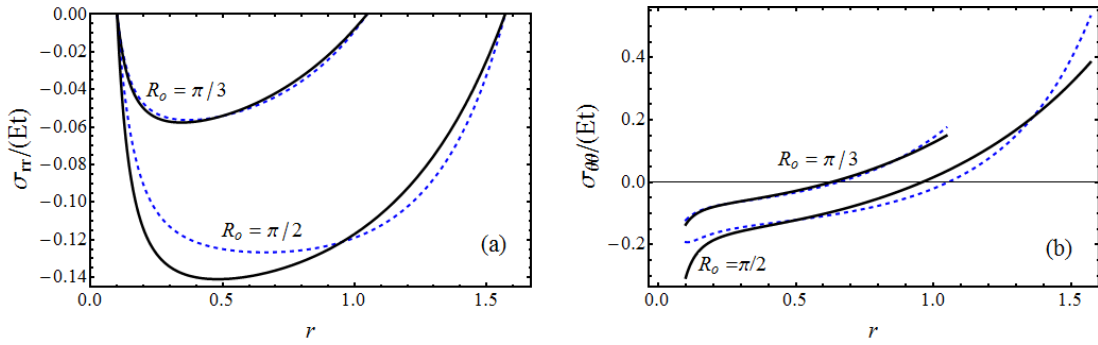


Figure 4.8: Comparison between the exact plane-stress solutions, Eqs. (4.46) (black solid line), and the numerical results based on Ref. [78] (dashed blue line) for an elliptic reference metric. Parameters as in Fig. 4.7.

The equation of equilibrium and the boundary condition are obtained by substituting Eq. (4.47) in Eq. (4.32) and (4.33a),

$$\sinh(r)\partial_r(\sinh(r)\partial_r u_r) - u_r = r - \sinh(r) + \nu \sinh(r)(1 - \cosh(r)), \quad (4.48a)$$

$$[\sinh(r)\partial_r u_r + \nu u_r + \nu(r - \sinh(r)) = 0]_{r=R}, \quad (4.48b)$$

where again we have rescaled r and u_r by $K^{-1/2}$. Since Eq. (4.48a) is obtained from (4.41a) by a Wick transformation,

$$r \rightarrow ir, \quad u_r \rightarrow iu_r, \quad (4.49)$$

we immediately obtain from Eqs. (4.43) and (4.44) the solution,

$$u_r(r) = -r + 2(1 - \nu) \coth^2(R/2) \ln[\cosh(R/2)] \times \left(1 + \frac{1 + \nu}{1 - \nu} \frac{\coth^2(r/2) \ln[\cosh(r/2)]}{\coth^2(R/2) \ln[\cosh(R/2)]} \right) \tanh(r/2), \quad (4.50a)$$

$$\sigma_{rr}(r) = Et \left(1 - \frac{\coth^2(r/2) \ln[\cosh(r/2)]}{\coth^2(R/2) \ln[\cosh(R/2)]} \right) \frac{\ln[\cosh(R/2)] \coth^2(R/2)}{\cosh^2(r/2)}, \quad (4.50b)$$

$$\sigma_{\theta\theta}(r) = -Et \left(1 - \frac{\ln[\cosh(r/2)]}{\sinh^2(r/2)} - \cosh^2(R/2) \frac{\ln[\cosh(R/2)]}{\cosh^2(r/2)} \right). \quad (4.50c)$$

It is readily verified that this solution satisfies the boundary condition (4.48b).

Similarly, the radial displacement and the stress distribution in an annulus with hyperbolic reference metric is obtained from Eqs. (4.46) via a Wick transformation, Eq. (4.49). In Figs. 4.9 and 4.10 we compare these solutions to the one obtained in Ref. [78].

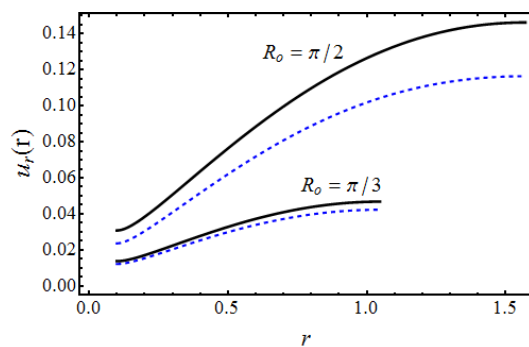


Figure 4.9: The exact solution for the radial displacement (black solid line) is plotted alongside the numerical solution of Eq. (10) in Ref. [78] (dashed blue line) for a hyperbolic reference metric. We consider an annulus with an inner radius $R_i = 0.1$, $\nu = 0$, and two different values of R_o as indicated. Lengths are normalized by $K^{-1/2}$.

4.5 Stability criterion for isometric immersions

An isometric immersion refers to a strain-free configuration, $\epsilon_{\alpha\beta} \equiv 0$, leading to $E_s = 0$. It is obviously the minimizer of the elastic energy for $B = 0$. In this section we do not directly seek the minimizer of the total energy, Eq. (4.15), but check whether the isometric immersion happens to be a minimizer also for $B > 0$. Since this configuration already minimizes E_s , we need to check only whether it also minimizes E_b . Note, however, that there are two different routes for such minimization: (a) set $\epsilon_{\alpha\beta} = 0$ in E_b and then minimize with respect to curvature alone; (b) minimize E_b with respect to both strain and curvature and only then set the strain

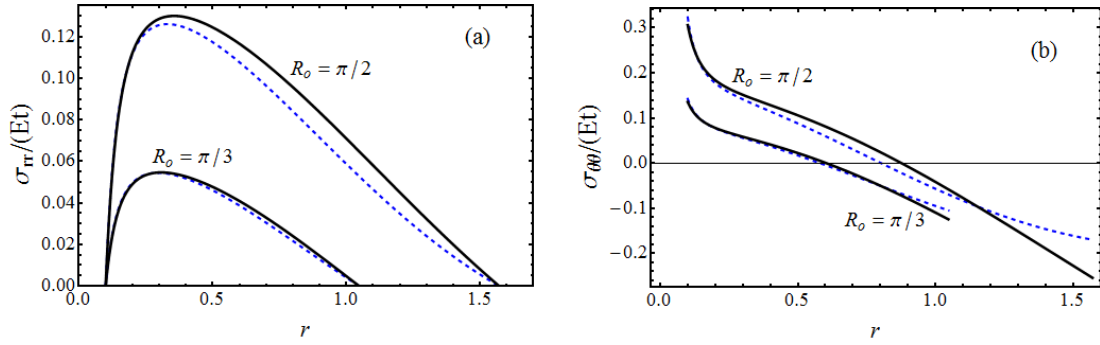


Figure 4.10: The exact radial and azimuthal plane-stress solutions for a flat annulus with a hyperbolic reference metric (solid black line) are compared with the numerical solution of Eq. (10) in Ref. [78] (dashed blue line). Parameters are as in Fig. 4.9.

to zero, which is the appropriate route. It is straightforward to show that in our model the two routes are equivalent. This is because the strain appears only quadratically in the energy (see, for example, Eq. (4.22)) and, therefore, setting the strain to zero, either before or after minimization, eliminates the same terms. However, in the ESK model the additional coupling term in the bending energy is linear in the strain (compare, for example, to Eq. (4.27)), leading to different results of the two routes. Hence, we conclude that the two theories should give the same results in case (a) but may differ in the appropriate minimization, case (b).

For a given reference metric of the form of Eq. (4.3), i.e., for a given $\Phi(r)$, the requirement of vanishing strain uniquely determines the configuration of the sheet up to rigid transformations. Indeed, setting Eqs. (4.11) to zero, we obtain,

$$u_r(r) = \Phi - r, \quad (4.51a)$$

$$\partial_r \zeta = \sqrt{1 - (\partial_r \Phi)^2}. \quad (4.51b)$$

We can now check whether this configuration satisfies local mechanical equilibrium of bending moments.

We substitute in Eq. (4.18) $\phi_{rr} = \partial_r \phi^r$ and $\phi_{\theta\theta} = \sin \phi^r / \Phi$ (see Fig. 4.1(a)),

$$E_b = \frac{1}{2} \int_0^R \int_0^{2\pi} [M_{rr} \partial_r \phi^r + M_{\theta\theta} \sin \phi^r / \Phi] \Phi d\theta dr, \quad (4.52)$$

and minimize with respect to ϕ^r ,

$$\partial_r (\Phi M_{rr}) - \cos \phi^r M_{\theta\theta} = 0, \quad (4.53a)$$

$$M_{rr}|_{r=R} = 0. \quad (4.53b)$$

(As has been done for the uniaxial bending case (Appendix C.1), one can show here as well that this minimization is equivalent to the appropriate one with respect to the spatial configuration; see Appendix C.4.) Equation (4.53a) expresses balance of moments on an infinitesimal sheet element in the radial direction [33, 155]. The boundary condition, Eq. (4.53b), imposes the vanishing of radial bending moment at the free edge.

Our aim now is to check whether the displacements given by Eqs. (4.51) also satisfy Eqs. (4.53). To this end we first express ϕ_{rr} and $\phi_{\theta\theta}$ in terms of $\Phi(r)$ using Eqs. (4.13) and (4.51),

$$\phi_{rr} = -\partial_{rr}\Phi/\sqrt{1 - (\partial_r\Phi)^2}, \quad (4.54a)$$

$$\phi_{\theta\theta} = \sqrt{1 - (\partial_r\Phi)^2}/\Phi. \quad (4.54b)$$

In addition, we have (see the relation between $\phi_{\theta\theta}$ and the angle ϕ^r in Fig. 4.1(a) and its caption),

$$\cos \phi^r = \partial_r\Phi. \quad (4.55)$$

Substituting Eqs. (4.54) in Eqs. (4.19), and the result, along with Eq. (4.55), in Eqs. (4.53), we obtain an equation and a boundary condition for $\Phi(r)$ alone,

$$\partial_r(\Phi\partial_{rr}\Phi/\sqrt{1 - (\partial_r\Phi)^2}) + \partial_r\Phi\sqrt{1 - (\partial_r\Phi)^2}/\Phi = 0, \quad (4.56a)$$

$$\left[\partial_{rr}\Phi/\sqrt{1 - (\partial_r\Phi)^2} - \nu\sqrt{1 - (\partial_r\Phi)^2}/\Phi\right]_{r=R} = 0. \quad (4.56b)$$

Equations (4.56) are a self-consistency condition for the reference metric, which must be satisfied for the isometric immersion to be an equilibrium configuration of the total energy. (It should be stressed that, if a certain isometric immersion does not satisfy this condition, it can still become the equilibrium configuration asymptotically, in the limit of vanishing B/Y [156].)

The displacements, Eqs. (4.51), and the bulk equilibrium equation, Eq. (4.56a), do not depend on ν . Hence, any solution but the trivial flat configuration, $\Phi(r) = r$, will violate, in general, the boundary condition (4.56b), which does depend on ν explicitly. In Ref. [78] it was shown that such boundary conditions may be taken care of by boundary layers. Thus, up to a small correction at the boundary (which vanishes in the limit of zero thickness), an isometry that satisfies the bulk condition, Eq. (4.56a), may be in mechanical equilibrium even if the boundary condition (4.56b) is not satisfied.

Let us now check the stability condition, Eq. (4.56a), for the examples of flat and elliptic reference metrics. In the case of a hyperbolic one, Eq. (4.47), the isometric immersion is not a surface of revolution [75], and therefore lies outside the scope of this work. (Substituting Eq. (4.47) in the height function, Eq. (4.51b), produces an imaginary result.)

Considering a flat reference metric, $\Phi(r) = \alpha r$, we immediately find that the self-consistency condition, Eq. (4.56a), is violated, and conclude that any isometric immersion of this metric will be unstable for $B > 0$. The isometric immersion of the flat metric is a cone with an opening angle $\vartheta = 2 \tan^{-1}(\alpha/\sqrt{1-\alpha^2})$,

$$\mathbf{f}(r, \theta) = r \left[\alpha \hat{\mathbf{r}} + \sqrt{1-\alpha^2} \hat{\mathbf{z}} \right]. \quad (4.57)$$

Note again that this does not preclude the possibility that the actual minimizer approaches a cone asymptotically for a vanishingly small B/Y [156].

In the example of an elliptic reference metric we substitute Eq. (4.40) in (4.56a) and find that the self-consistency condition is satisfied in the bulk. The isometric immersion of an elliptic reference metric is a spherical cap of radius $1/\sqrt{K}$,

$$\mathbf{f}(r, \theta) = \frac{1}{\sqrt{K}} \left(\sin(\sqrt{K}r) \hat{\mathbf{r}} + \cos(\sqrt{K}r) \hat{\mathbf{z}} \right). \quad (4.58)$$

When we substitute this configuration in the formalism of Ref. [68] (the first of Eqs. (3.10) in Ref. [68]), we find that it does not satisfy balance of normal forces (see Appendix C.4). This procedure corresponds to route (b) described above, i.e., substitution of the isometric immersion in the full equations of equilibrium rather than eliminating the strain from the beginning. Thus, as anticipated above, the two theories disagree. A spherical cap satisfies our stability condition but is found to be unstable for $B > 0$ by the ESK theory. (Recall that the two theories do coincide if one wrongly follows the other route in the ESK model.) The spherical cap configuration of a sheet with elliptic reference metric was found to be stable in experiments [75]. We note that the criterion at the boundary, Eq. (4.56b), is not satisfied by the elliptic $\Phi(r)$. This can be mended by a thin boundary layer of width $\propto t^{1/2}$ [78]. In Appendix C.2 we give an alternative, more complete derivation of this result within the FvK approximation.

In Appendix C.3 we add a similar stability criterion for two examples of surfaces of revolution whose reference metric is slightly more general than the ones assumed so far.

4.6 Discussion

We have presented an alternative formulation for the elasticity of incompatible thin sheets, which is restricted to axisymmetric deformations. This formulation and the existing ESK theory [78] are not equivalent. The lack of equivalence has been demonstrated in three systems—the

existence or absence of in-plane strain in a uniaxially bent sheet (Sec. 4.3); the strains forming in flat incompatible sheets (Sec. 4.4, see Figs. 4.5 – 4.7); and the stability of the spherical-cap isometry for a sheet with an elliptic reference metric (Sec. 4.5).

The key ingredient that sets the two models apart is a coupling between stretching and bending, which appears in the ESK model upon dimensional reduction, and is removed in the present formulation by using distance deviations, rather than metric deviations, to define strain. (Recall, for example, Eq. (4.22) vs. Eq. (4.27).) Let us pinpoint the stage at which this difference emerges. If the derivation of Eqs. (4.5)–(4.12) in the dimensional reduction is repeated for the Green-St. Venant strain, Eq. (4.1), then Eqs. (4.12) are replaced by $\tilde{\epsilon}_{rr}^* = \tilde{\epsilon}_{rr} - 2x_3 b_{rr} + x_3^2 c_{rr}$, and $\tilde{\epsilon}_{\theta\theta}^* = \tilde{\epsilon}_{\theta\theta} - 2x_3 b_{\theta\theta}/\Phi^2 + x_3^2 c_{\theta\theta}/\Phi^2$. The different dependence on the x_3 coordinate perpendicular to the mid-surface, inevitably leads to additional terms upon integration of the energy over x_3 .

Quantitatively, the differences caused by the coupling terms are small and indeed may lie outside the strict limits of the infinitesimal-strain theory. They seem negligible experimentally. The removal of these terms, however, leads to a much simpler analysis, as demonstrated by the exact solutions in Sec. 4.4. (A similar observation was made in the context of beam theory [29].) Since, at least for the problems considered in this manuscript, the differences can be neglected, there is freedom, and clear benefit, in choosing a more tractable formulation when it is available.

The two models become equivalent in the incompressible limit, $B/Y = 0$. The problems treated in Secs. 4.3 and 4.5 reveal an essential difference in the way the two models *depart* from this limit. Both problems—the uniaxially bent sheet and the sheet with elliptic reference metric—possess a strain-free configuration (isometric immersion) as the energy minimizer for $B/Y = 0$. According to the ESK model this configuration ceases to be the minimizer for an arbitrarily small but finite B/Y ; according to the model presented here it remains the energy minimizer to leading order in B/Y . In other words, as B/Y tends to zero, the equilibrium configuration reaches the isometry with nonzero slope in the former, and with zero slope in the latter. In a sheet made of a 3D material both Y and B emanate from the same elastic modulus. Then, it may well be that a stretching-bending coupling exists even in the absence of Gaussian curvature, leading with decreasing thickness to the “nonzero slope” behavior. In a genuinely 2D sheet, such as a monomolecular layer or a 2D polymer network, Y and B can be independent (e.g., arising from the rigidities of bonds and bond angles, respectively). In such cases, for example, it may well be that stretching and bending should be decoupled,

leading to the “zero slope” case—i.e., an isometry (no stretched bonds) remaining the energy minimizer for $B/Y > 0$ (finite joint rigidity). These delicate issues might be checked in discrete simulations. While being conceptually interesting, they may have (at least according to the problems considered here) little practical significance.

The exact solutions presented in Sec. 4.4 for the strains and stresses in flat incompatible sheets can be used as the base solutions for a perturbative (near-threshold) treatment of buckling instabilities in these systems, which can then be studied experimentally. Our formulation can be applied to additional examples beyond those addressed in Secs. 4.4 and 4.5, where the reference metric is axisymmetric. An interesting problem, for instance, might be the case of a highly localized (delta-function) $\Phi(r)$. In addition, the theory might be useful for analyzing stress fields around two-dimensional defects [82, 83].

The most important extension of this work, however, would be to obtain a similarly tractable formulation for sheets of any two-dimensional deformation. The discussion above suggests two possible routes. One is to generalize the formulation presented in Sec. 4.2 beyond axisymmetric deformations. The other is to modify the ESK energy functional such that the two choices of strain measures lead to equivalent theories.

Chapter 5

Concluding remarks and future directions

This thesis highlights the complexity and rich behavior of strongly deformed elastic sheets. Below, for each of the three parts of the thesis, we briefly summarize the results and indicate possible directions for future study.

5.1 The problem of floating elastica

In this thesis we extended the elastic theory of a thin sheet lying on a fluid substrate and uniaxially compressed, to accommodate finite size effects (see Chapter 2). We obtained the exact solution for the wrinkled state and an approximate solution for the folded state. We predicted that at the critical confinement $\Delta_F = \lambda^2/L$ the wrinkles state becomes unstable against the localized pattern. This result has not yet been confirmed experimentally.

Future extensions to this work can be divided into static and dynamic applications. Here are four suggestions for the static, time-independent, case: (i) Extending the theory to include extensibility corrections. This modification will allow to treat both the flat-to-wrinkle and the wrinkles-to-fold transitions, and to construct the complete “phase-diagram” of the system. (ii) Solving the equilibrium equations for different boundary conditions. In this study only hinged conditions have been considered, Eq. (2.37). However, other conditions, such as clamped, are frequently used in experimental systems [157, 158]. (iii) Considering the effect of different sub-

strates [43]. For example, when the fluid is replaced with an elastic foundation [108], wrinkles become unstable against multiple-length-scale patterns at a critical confinement. The characteristics of this transition are yet to be determined. (iv) We have not been able to find the exact localized solution for a finite sheet. Looking for such a solution may justify additional effort, because it should probably belong to a different branch of solutions of the governing nonlinear equation, which has not been considered so far.

A floating sheet can also be perturbed dynamically if, for example, one of the external forces is oscillating in time. One possible setup for such study is a liquid, vibrated from below, whose upper surface is covered by a thin elastic sheet. At a critical excitation mode the upper surface is expected to become unstable against periodic undulations, a phenomenon known (without the elastic layer) as Faraday waves.

Within the context of this interesting Faraday-Elastica system we suggest two possible problems to explore. (i) The study of pattern selection. Classical experiments on Faraday systems find stripes (wrinkles), squares, hexagons, and even quasicrystalline point symmetries on the free surface of the vibrated vessel [159]. When the upper surface is covered with a thin sheet the interplay between stretching and bending is expected to play a crucial roll in the selection of a specific pattern, especially when non-zero Gaussian curvature (beyond wrinkles) is formed. (ii) The study of solitary waves. Localized waves in Faraday systems have been experimentally observed [160–162] and theoretically analyzed [163–166]. These studies, however, required either special geometric configuration of the fluid vessel, such as Hele-Shaw cells, or a special configuration in the vibrating forces, such as simultaneous vibrations of the vertical and horizontal directions. Given our results for the static system (Chapter 2), we would expect to have localized patterns in the modified Faraday-elastica system even without the above-mentioned modifications.

5.2 Elastic-kinetic analogies

In this project we extended the analogy between inextensible thin rods and the classical dynamics of rigid bodies, see Chapter 3. We showed that if the inextensibility assumption is relaxed, the corrections to the elastic model are akin to relativistic corrections in the dynamic system.

On a broader perspective, the extended analogy suggests an alternative derivation of special-

relativistic mechanics. In this approach the two postulates of relativity are naturally obtained from minimization of a more primitive action, e.g., the Lorentz invariance and the limiting speed result from an action variation. Deriving the theory from a more fundamental starting point allows one to ask more elementary questions on the origin of the two traditional postulates. For example, in Appendix B.1 we showed that Galilean or Lorentz invariance of the elastic energy depends on the given information prior to the minimization. Analogously, we concluded that Lorentz invariance is selected in the dynamic problem since the boundary conditions and the duration of the experiment are given in the laboratory frame, not the proper one. We were not able to provide a similar explanation for the limiting speed.

The extended analogy was utilized to reveal a new symmetry in the elastic problem and to derive an exact solution to the motion of the relativistic physical pendulum. Future extensions may address the following. The instability of a flat extensible rod or sheet toward curved configurations is connected to the emergence of oscillations from rest in the parametric resonance of a relativistic oscillator (see discussion in Sec. 1.2.3). A change in the compression modulus of an elastic system (e.g., as a result of a temperature change) might be studied in analogy to a change in a particle's rest mass.

5.3 The elastic theory of incompatible sheets

In this study we reconsidered the elastic theory of incompatible thin sheets [68], see Chapter 4. We showed that, if the strain tensor is redefined based on Biot's approach, the mathematical complexity of the existing theory is greatly reduced. Despite these important differences we found, qualitatively, only minor discrepancies between the minimizing configurations of the two models.

Naturally, one may still ask if these discrepancies are necessarily negligible in any system of incompatible thin sheets. Although we do not have a conclusive answer to this question, let us try to address it by classifying the elastic problems into two groups. The classification that we suggest here is based on our qualitative discussion in Sec. 4.6 on the slope of convergence towards the isometric shapes. Quantitatively, denoting the energy of the configuration $\mathbf{f}(\mathbf{r})$ by $E[\mathbf{f}] = \int e[\mathbf{f}]dA$, one way to define this slope is,

$$m \equiv \frac{1}{E[\mathbf{f}_{\text{iso}}]} \int \left| \frac{e[\mathbf{f}_{\text{iso}} + \delta\mathbf{f}] - e[\mathbf{f}_{\text{iso}}]}{\delta\mathbf{f}} \right| dA \simeq \frac{1}{E[\mathbf{f}_{\text{iso}}]} \int \left| \frac{\delta e}{\delta\mathbf{f}} \right|_{\mathbf{f}=\mathbf{f}_{\text{iso}}} dA, \quad (5.1)$$

where \mathbf{f}_{iso} is the isometric configuration, $\delta\mathbf{f}$ is a general perturbation and $|\mathbf{x}|$ is the norm of the vector \mathbf{x} . In the limit of small thickness, Eq. (5.1) measures how the energy of the isometric immersion changes when it is slightly distorted, e.g., as m increases the convergence towards the isometry is slower. Practically, to calculate the slope one needs to obtain the equilibrium equations, $\delta e/\delta\mathbf{f} = 0$, substitute the strain-free configuration inside them, perform the integration and normalize by $E[\mathbf{f}_{\text{iso}}]$ ¹.

Obviously, the value of m must be one of the following: (i) zero, (ii) finite constant, or (iii) infinity. The slope is zero if \mathbf{f}_{iso} satisfies the equilibrium equations, $\delta e/\delta\mathbf{f} = 0$; as, for example, it happens in the spherical cap case using our model (see Sec. 4.5). The slope is a constant if \mathbf{f}_{iso} violates the equilibrium equations and $\delta e/\delta\mathbf{f} \sim t^3$. (The non-zero terms that remain after the substitution of the isometric shape in the equations scale as t^3). See for example the cone in Sec. 4.5 and the spherical cap in the ESK theory, Appendix C.4.2. Lastly, the slope diverges if \mathbf{f}_{iso} does not satisfy the equilibrium equations and $\delta e/\delta\mathbf{f} \rightarrow \infty$. Such problems have not been considered in the present work.

We identify the first class of elastic problems with cases (i) and (ii). In this class an elastic configuration converges to a strain-free shape in the limit of vanishing thickness. While in our theory the convergence can either be with a zero or a finite slope, in the ESK theory the convergence is always with a finite slope. Since in this class both models differ only slightly in their rate of convergence towards the isometry, we expect the experimental differences to be negligible. Nevertheless, if the slope of convergence is very high but finite, cases (i) and (ii) may behave differently. For the problems considered herein, this behavior was not encountered.

We identify the second class of problems with case (iii) where the slope diverges ($m \rightarrow \infty$). This class dominates, for example, when the isometric shapes include discontinuities [80, 81]. Physically, sharp corners in the elastic configuration correspond to discontinuous bending moments, which in return leads to divergences in the equilibrium equations, $\delta E/\delta\mathbf{f} \rightarrow \infty$. Typical problems in this class include multi-wave patterns (see Fig. 1.9a) and wrinkles cascades (Fig. 1.9c). Thus, it lies outside the scope of the formulation developed in Chapter 4 for axisymmetric shapes. We assess that this class, for some scenarios, should entail significantly different experimental predictions as obtained from the two models.

Recent experiments and theoretical studies on wrinkles in compatible sheets [10, 62], sug-

¹This definition neglects the effects of boundary conditions.

gested that these patterns emerge from stretching and bending competition at scales that are larger than t^3 . Based on these observations it seems reasonable to assume that this is also the mechanism in incompatible sheets, at least for some range of their parameters. Thus, we anticipate that the different stretching-bending coupling terms in the two models might have a stronger effect on the selected pattern in these systems as well.

Appendices

Appendix A

Wrinkles and folds in a fluid supported sheet - Appendices

A.1 Exact localized solutions to Eq. (2.8)

In this Appendix we derive exact localized solutions to Eq. (2.8), which are not physical solutions of our problem treated here, but may be of use in future research. Equation (2.8) is a member of the sine-Gordon-modified-Korteweg-de Vries hierarchy [122] in which the sine-Gordon equation is a lower member. Consequently, a solution of the sine-Gordon equation is also a solution of Eq. (2.8). Using the separation of variable proposed by Lamb [167], the following function

$$\phi(s, t) = 4 \arctan(F(s)/G(t)), \quad (\text{A.1})$$

is a solution of the sine-Gordon equation provided F and G satisfy the following differential equations [168]

$$(F')^2 = -\kappa F^4 + \mu F^2 + \lambda, \quad (\text{A.2a})$$

$$(G')^2 = \kappa G^4 + (\mu - 1)G^2 - \lambda, \quad (\text{A.2b})$$

where κ , μ and λ are arbitrary constants. The function (A.1) with $t = s$ is also a solution of Eq. (2.8) if F and G satisfy the relations (A.2) and provided that

$$\tilde{P} = 2 - 4\mu. \quad (\text{A.3})$$

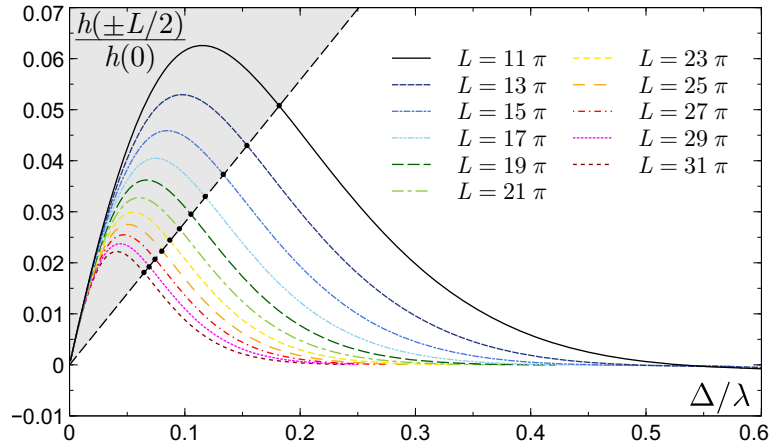


Figure A.1: Evolution of the normalized height of the exact solution (A.6a) at the boundaries as a function of the normalized displacement. The dots indicate the position of the threshold, Δ_F/λ , below which the profile is periodic. The shaded area corresponds thus to the wrinkle state. This area is delimited by the relation $h(\pm L/2)/h(0) = 0.279 \Delta_F/\lambda = 0.279 \lambda/L$.

Introducing some scaling parameters [169], $Af(\beta s) = F(s)$ and $g(\omega s) = 1/G(s)$, Eqs. (A.2) become

$$(f')^2 = \beta^{-2} [-\kappa A^2 f^4 + \mu f^2 + \lambda A^{-2}], \quad (\text{A.4a})$$

$$(g')^2 = \omega^{-2} [-\lambda g^4 + (\mu - 1)g^2 + \kappa]. \quad (\text{A.4b})$$

Solving Eqs. (A.4) allows to determine f and g and to obtain an exact solution of Eq. (2.8). Those equations are satisfied by the Jacobi elliptic functions with arguments βs and ωs and parameters k_f and k_g . The various parameters are fixed by comparison between Eqs. (A.4) and those satisfied by the Jacobi functions:

$$\text{sn}(s, k) : (y')^2 = k^2 y^4 - (1 + k^2)y^2 + 1 \quad (\text{A.5a})$$

$$\text{cn}(s, k) : (y')^2 = -k^2 y^4 + (2k^2 - 1)y^2 + 1 - k^2 \quad (\text{A.5b})$$

$$\text{dn}(s, k) : (y')^2 = -y^4 + (2 - k^2)y^2 - 1 + k^2 \quad (\text{A.5c})$$

Hinged sheets

We choose $f = \text{cn}(\beta s, k_f)$ and $g = \text{sn}(\omega^+ s, k_g^+)$ or $g = \text{cn}(\omega^- s, k_g^-)$ such that

$$\phi(s) = 4 \arctan[A \text{cn}(\beta s, k_f) \text{sn}(\omega^+ s, k_g^+)], \quad (\text{A.6a})$$

$$\phi(s) = 4 \arctan[A \text{cn}(\beta s, k_f) \text{cn}(\omega^- s, k_g^-)]. \quad (\text{A.6b})$$

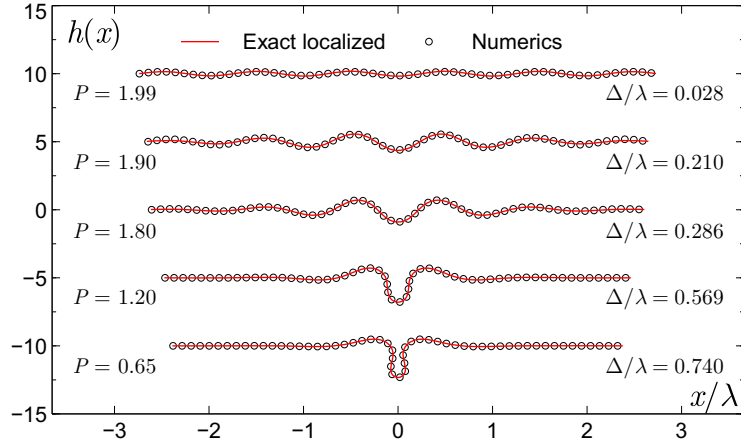


Figure A.2: (Color online) Evolution of the solution (A.6a) for different values of Δ/λ and $L/\lambda = 5.5$, where $x(s)$, $h(s)$ are given by Eqs. (2.1) and $\phi(s)$ is given by Eq. (A.6a). The corresponding evolution for the numerical solution of Eq. (2.8) is also shown. For $\Delta/\lambda < \Delta_F/\lambda = 0.182$, the numerical solution is periodic and coincides with the solution reported in Section 2.3.

Equations (A.6a) and (A.6b) lead to symmetric and antisymmetric solutions respectively. Comparison between Eqs. (A.4) and Eqs. (A.5) for that particular choices of f and g fixes six parameters (among eight parameters for each parity of ϕ) as a function of A and β as follows:

$$\omega^+ = \frac{[1 + (1 + A^2)\beta^2]^{1/2}}{1 + A^2}, \quad (\text{A.7a})$$

$$\omega^- = \left[\frac{2}{1 + A^2} + \beta^2 - 1 \right]^{1/2}, \quad (\text{A.7b})$$

$$k_g^+ = A \left[\frac{1 + A^2}{1 + (1 + A^2)\beta^2} - 1 \right]^{1/2}, \quad (\text{A.7c})$$

$$k_g^- = A \left[\frac{\beta^2 + A^2(\beta^2 - 1)}{1 - A^4 + (1 + A^2)^2\beta^2} \right]^{1/2}, \quad (\text{A.7d})$$

$$k_f = \frac{A}{1 + A^2} (1 + A^2 + \beta^{-2})^{1/2}, \quad (\text{A.7e})$$

$$\mu = \frac{2A^2 + (A^4 - 1)\beta^2}{(1 + A^2)^2}. \quad (\text{A.7f})$$

The expressions of κ and λ are not needed in the following and are not written. The amplitude A of the solutions (A.6) is related to the displacement Δ through Eq. (2.2) whereas β should be fixed to satisfy the boundary conditions.

For hinged boundary conditions both h and $\ddot{h} = \dot{\phi} \cos \phi$ vanish at $s = \pm L/2$. From Eq. (2.7), this is equivalent to $\dot{\phi}(\pm L/2) = \ddot{\phi}(\pm L/2) = 0$. The condition $\dot{\phi}(L/2) = 0$ for the symmetric

solution (A.6a) leads to the constraint

$$\frac{\operatorname{dn}(x, k_f) \operatorname{sn}(x, k_f) \operatorname{sn}(y, k_g^+)}{\operatorname{cn}(x, k_f) \operatorname{cn}(y, k_g^+) \operatorname{dn}(y, k_g^+)} = \frac{y}{x}, \quad (\text{A.8})$$

where $x = \beta L/2$ and $y = \omega^+ L/2$. Due to the definite parity of the solution, $\dot{\phi}(-L/2) = 0$ is automatically satisfied. A similar relation is easily obtained for the antisymmetric solution (A.6b) which is not written here. For a given amplitude, A , and a given sheet length, L , Eq. (A.8) fixes β . The displacement, Δ , and the pressure, \tilde{P} , are then computed from Eqs. (2.2) and (A.3) respectively. Finally, P is computed from Eq. (2.9).

It is however impossible to satisfy both boundary conditions with the solutions (A.6). For the exact periodic solution (2.18), both $\dot{\phi}(s)$ and $\ddot{\phi}(s)$ are proportional to $\operatorname{cn}(q(s + s_0), k)$ such that they can simultaneously vanish at the boundaries with a suitable choice of q (and s_0), see Eqs. (2.22). Here, $\dot{\phi}(L/2)$ and $\ddot{\phi}(L/2)$ cannot simultaneously vanish for the same value of β . Therefore, the height of the profile assumes a finite value at the boundaries as shown in Fig. A.1. Notice however that $h(\pm L/2)/h(0)$ decreases as L increases.

Nevertheless, despite the fact that it does not properly satisfy the boundary conditions, this solution is a very good approximation of the numerical solution satisfying both boundary conditions. Figure A.2 shows a comparison between this exact localized solution and the numerical solution of Eq. (2.8). The agreement is good especially near the central fold and for large enough confinement.

A.2 Accuracy of $\Delta_{\mathbf{F}}$ and $P_{\mathbf{F}}$

The critical displacement, $\Delta_{\mathbf{F}}$, and pressure, $P_{\mathbf{F}}$, at which the transition from wrinkles to fold occurs has been computed in Sections 2.4.2 and 2.5. These expressions are obtained from matching, at the first order in Δ/L , between the exact periodic and the approximate localized solutions, see Section 2.5.2, and converge toward the exact values in the limit $L \rightarrow \infty$. Although a rigorous derivation of the error on these two quantities is only possible if their exact expressions are known, an estimation of the rate of convergence can be obtained from the exact periodic solution.

Indeed, since at the transition $P(\Delta)$ coincides for both the periodic and the localized solutions, the exact expressions of $\Delta_{\mathbf{F}}$ and $P_{\mathbf{F}}$ should satisfy Eqs. (2.31) and (2.32) for the same

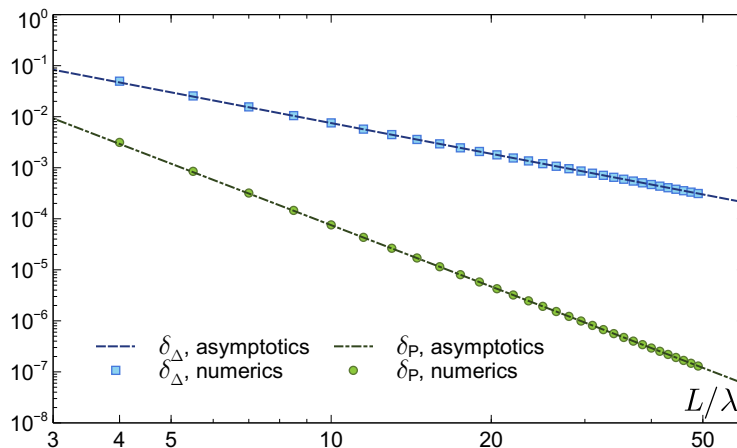


Figure A.3: (Color online) Evolution of δ_Δ and δ_P as a function of the sheet length (normalized by the wavelength) obtained by solving numerically Eqs. (A.9). The asymptotic behaviors (A.10) are also shown.

$k = k_c$. This is not the case with the approximate expressions we have obtained in this paper. Therefore, we define two quantities, δ_Δ and δ_P , as follows

$$\delta_\Delta = \frac{\Delta(\bar{k}_c) - \Delta_F}{\Delta(\bar{k}_c)} \quad \text{with} \quad P(\bar{k}_c) = P_F, \quad (\text{A.9a})$$

$$\delta_P = \frac{P(\tilde{k}_c) - P_F}{P(\tilde{k}_c)} \quad \text{with} \quad \Delta(\tilde{k}_c) = \Delta_F, \quad (\text{A.9b})$$

where $\Delta(k)$, $P(k)$, P_F and Δ_F are given by Eqs. (2.31), (2.32), (2.65) and (2.66) respectively. With the exact expressions of Δ_F and P_F , we have $\bar{k}_c = \tilde{k}_c$ and $\delta_\Delta = \delta_P = 0$. The quantities δ_Δ and δ_P are thus a measure of the error introduced and of the rate of convergence toward the exact expressions of the critical displacement and pressure.

Expanding both $\Delta(k)$ and $P(k)$ up to k^4 , we obtain at the leading order in λ/L :

$$\delta_\Delta = \frac{3\lambda^2}{4L^2} + \mathcal{O}\left[\frac{\lambda^4}{L^4}\right] \quad \text{and} \quad \delta_P = \frac{3\lambda^4}{4L^4} + \mathcal{O}\left[\frac{\lambda^6}{L^6}\right]. \quad (\text{A.10})$$

Figure A.3 shows that the evolution of δ_Δ and δ_P as a function of L/λ obtained by solving numerically Eqs. (A.9) agrees well with the asymptotic expression (A.10) even when L/λ is not so large. Therefore, the expressions of Δ_F and P_F derived in the paper converges toward the exact values as L^{-2} and L^{-4} respectively.

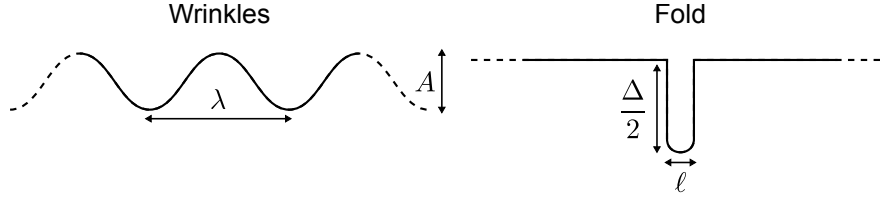


Figure A.4: Schematics for wrinkles and fold patterns.

A.3 Scaling approach

In this section, we show that some of the results obtained in the main text, and in particular the critical confinement at which a wrinkle-to-fold transition occurs, can be qualitatively recovered using a simple scaling approach. As formulated in Sec. 2.2, the bending energy of the sheet E_b and the deformation energy of the substrate E_s read

$$E_b = \frac{WB}{2} \int_{-L/2}^{L/2} \dot{\phi}^2 ds, \quad (\text{A.11})$$

$$E_s = \frac{W\rho g}{2} \int_{-L/2}^{L/2} h^2 \cos \phi ds, \quad (\text{A.12})$$

and the displacement along the direction of confinement is given by

$$\Delta = \int_{-L/2}^{L/2} (1 - \cos \phi) ds. \quad (\text{A.13})$$

Small displacement

For small displacement, leading to small sheet deformations ($\phi \ll 1$), wrinkles emerge with an amplitude A , wavelength λ and curvature $\dot{\phi} \sim A/\lambda^2$, see Fig. A.4. The energies thus scale as

$$E_b \sim BWLA^2/\lambda^4; \quad E_s \sim \rho gWLA^2. \quad (\text{A.14})$$

The balance of these two energies leads to

$$\lambda \sim (B/\rho g)^{1/4}. \quad (\text{A.15})$$

In the limit $\phi \ll 1$, the relation between the amplitude and the displacement is given by

$$\Delta \sim \int_{-L/2}^{L/2} \phi^2 ds \sim \int_{-L/2}^{L/2} (dh/ds)^2 ds \sim L(A/\lambda)^2. \quad (\text{A.16})$$

Large displacement

The total energy of the system can be written as

$$\frac{E}{W} = \frac{B}{2} \int_{-L/2}^{L/2} \dot{\phi}^2 ds + \frac{\rho g}{2} \int_{-L/2}^{L/2} h^2 ds - \frac{\rho g}{2} \int_{-L/2}^{L/2} h^2 (1 - \cos \phi) ds \quad (\text{A.17})$$

$$\sim B\Lambda\dot{\phi}^2 + \rho g\Lambda A^2 - \rho g A^2 \Delta \sim \rho g \left[\lambda^4 \Lambda \dot{\phi}^2 + \Lambda A^2 - A^2 \Delta \right], \quad (\text{A.18})$$

where Λ is the spatial extent of the localized pattern, $\dot{\phi}$ its typical curvature and A its amplitude.

For wrinkles, we have $\Lambda \sim L$, $\dot{\phi} \sim A/\lambda^2$ and $A \sim \lambda\sqrt{\Delta/L}$, see Eq. (A.16). The wrinkles energy can thus be written as

$$E_W/W = \rho g \lambda^3 \left[a \Delta/\lambda - b (\lambda/L)(\Delta/\lambda)^2 \right], \quad (\text{A.19})$$

where a and b are numerical constants. For a fold, we have $\Lambda \sim \ell$, the fold width, $\dot{\phi} \sim \ell^{-1}$, and $A \sim \Delta$, see Fig. A.4. The fold energy can thus be written as

$$E_F/W = \rho g \left[(c^2/4\bar{c})\lambda^4/\ell + \bar{c}\ell\Delta^2 - d\Delta^3 \right], \quad (\text{A.20})$$

where c , \bar{c} and d are numerical constants. A minimization of E_F with respect to ℓ gives $\ell = (c/2\bar{c})\lambda^2/\Delta$ and the energy becomes

$$E_F/W = \rho g \lambda^3 \left[c \Delta/\lambda - d(\Delta/\lambda)^3 \right]. \quad (\text{A.21})$$

Requiring that the wrinkles and fold energies match at $\Delta = \Delta_F$ gives a quadratic equation for Δ_F . Demanding that Δ_F vanishes when L diverges yields $a = c$. A wrinkle-to-fold transition occurs when $E_W > E_F$ or equivalently, using $a = c$, when $\Delta > \Delta_F = (b/d)\lambda^2/L$. Thus, this simple analysis has recovered the correct scaling of Δ_F with respect to λ and L . As shown in Sec. 2.5, the prefactor b/d turns out to be exactly 1.

Appendix B

Analogy between extensible elastica and relativistic dynamics — Appendices

B.1 On Galilean and Lorentz invariance of a free extensible filament

In this appendix we show that in the absence of external fields the energy of an extensible filament, Eq. (3.1), is invariant under an “elastic Galilean boost” if the given information prior to minimization is the total undeformed length of the filament, L (see Fig. B.1a). Contrary, under the same conditions Eq. (3.1) is invariant under an “elastic Lorentz boost” if the given information prior to minimization is the deformed length of the filament, \hat{L} (see Fig. B.1b). Hereafter we will refer to these boosts as just “Galilean” or “Lorentz”. In addition, let us emphasize that this is only a theoretical discussion, for the sake of getting more insight into the analogy. Of course, in elasticity the first direction is always the physical one — given the undeformed length, L , we minimize the energy to obtain \hat{L} .

In the following two subsections we explore these two directions of minimization and show that the elastic energy becomes *canonically* invariant to Galilean or Lorentz transformation once a certain direction is selected.

A transformation, $\{s, \phi\} \rightarrow \{S, \Phi\}$, is said to be canonical if the minimized configuration of

$E[\phi(s)]$, which we denote by $\phi(s)$, that is transformed into $\Phi(S)$, yields the same result as first transforming the energy, $E[\phi(s)]$, into the new coordinates, and then minimizing $E[\Phi(S)]$ with respect $\Phi(S)$. In other words, the following two routes

$$\text{route i: } E[\phi(s)] \rightarrow \phi(s) \rightarrow \Phi(S), \quad (\text{B.1a})$$

$$\text{route ii: } E[\phi(s)] \rightarrow E[\Phi(S)] \rightarrow \Phi(S), \quad (\text{B.1b})$$

must yields the same solution for $\Phi(S)$ in order for the energy to be canonically invariant under a given transformation.

B.1.1 Extensible Galilean filament

When the total relaxed length of the filament, L , is conserved we may minimize Eq. (3.1) as it is without further modifications (Fig. B.1a). In the absence of an external potential, $V = 0$, we have from Eq. (3.2a) that $\gamma = 1$, and the energy reduces to,

$$E[\phi(s)] = \frac{B}{2} \int_0^L \left(\frac{d\phi}{ds} \right)^2 ds. \quad (\text{B.2})$$

Equation (B.2) is analogous to the Lagrangian of a free, classical, particle (see Table 3.3 and Fig. B.1c). Despite its trivial form and obvious result upon minimization we proceed to show that it is invariant under a Galilean boost. This analysis will later be useful in comparison with the less-trivial, Lorentz case.

Considering the Galilean transformation,

$$ds = dS, \quad (\text{B.3a})$$

$$d\phi = d\Phi + \kappa dS, \quad (\text{B.3b})$$

we aim to show that Eq. (B.2) gives the same result for $\Phi(S)$ according to the two routes, Eqs. (B.1). Following the first route, Eq. (B.1a), we minimize Eq. (B.2) with respect to $\phi(s)$ obtaining $d\phi/ds = 0$. Galilean boost of this solution to the new coordinates, Eqs. (B.3), gives,

$$\frac{d\Phi}{dS} = -\kappa. \quad (\text{B.4})$$

Following the second route, Eq. (B.1b), we transform the energy, Eq. (B.2), to $\{\Phi, S\}$ ¹,

$$E[\Phi(S)] = \frac{B}{2} \int_0^L \left(\frac{d\Phi}{dS} \right)^2 dS + B\kappa \int_0^L d\Phi + \frac{B}{2} \kappa^2 \int_0^L dS, \quad (\text{B.5})$$

¹For simplicity of the following derivations we use the notation $\int_0^L d\Phi = \int_0^L \frac{d\Phi}{dS} dS$ to denote the integral of a total derivative. This term in the energy contributes only to the boundary condition.

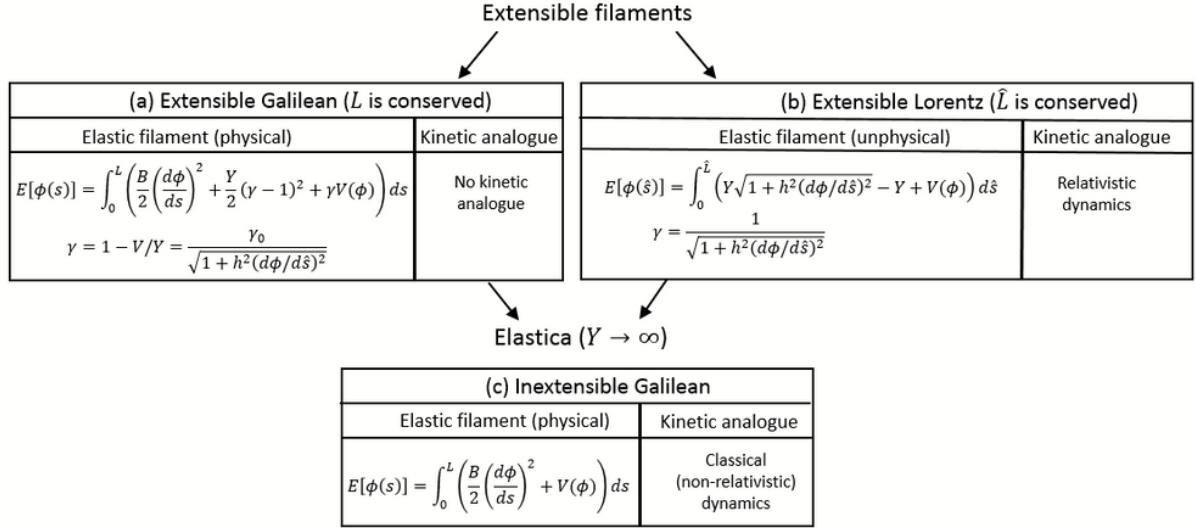


Figure B.1: The formulation of extensible filaments is divided into two groups according to the conserved length prior to minimization. (a) If the undeformed length, L , is conserved, the energy functional and the stretching field are given by Eqs. (3.1) and (3.5). This is the physical model of extensible elastica; see Chapter 1 Sec. 1.2.1 and Chapter 3 Sec. 3.2. In the absence of external fields, $V = 0$, the energy becomes invariant under the “elastic Galilean boost”, Eq. (B.3), and the stretching field is equal to unity, $\gamma = 1$. These filaments, strictly, do not have a kinetic analogue. However, their equilibrium equation, Eq. (3.4), becomes mathematically analogous to the relativistic one if the constant prefactor, γ_0 , is absorbed in the potential (see discussion in the main text, Chapter 3 Sec. 3.3). (b) If, unphysically, the deformed length, \hat{L} , is conserved the energy and the stretching field are given by Eqs. (B.11) and (B.12). If, in addition, $V = 0$ this energy becomes invariant under the “elastic Lorentz boost”, Eq. (B.14). Consequently, the formulation of extensible Lorentz filaments is analogous to relativistic mechanics (up to a sign difference in the denominator of γ). (c) In the limit of inextensibility ($Y \rightarrow \infty$) both panels, (a) and (b), converge to Euler’s elastica (see Sec. 1.2.1). In the absence of external forces this formulation becomes Galilean invariant (similar to panel (a)). The kinetic analogue of these filaments is the classical, non-relativistic, dynamics.

and minimize it with respect to $\Phi(S)$. This yields the following equilibrium equation and boundary condition,

$$d^2\Phi/dS^2 = 0, \quad (\text{B.6a})$$

$$[d\Phi/dS]_{s=0,L} = -\kappa. \quad (\text{B.6b})$$

Since the solution of these equations is given by Eq. (B.4), the energy is found to be canonically invariant under a Galilean boost. Furthermore, one can now verify from Eqs. (B.2) and (B.5) that $E[\phi(s)] = E[\Phi(S)] = 0$ upon substitution of their respective minimizing configurations.

This invariance property is preserved in the slightly more general case of a filament that is confined by pure bending moments, $M = B\bar{\kappa}$ (keeping in mind that $\gamma = 1$). In this case the energy, Eq. (B.2), is modified into,

$$E[\phi(s)] = \frac{B}{2} \int_0^L \left(\frac{d\phi}{ds} \right)^2 ds + M \int_0^L d\phi. \quad (\text{B.7})$$

Following the first route, Eq. (B.1a), and minimizing Eq. (B.7) with respect to $\phi(s)$ gives, $d\phi/ds = -\bar{\kappa}$. Galilean boost of this solution yields,

$$\frac{d\Phi}{dS} = -(\bar{\kappa} + \kappa). \quad (\text{B.8})$$

On the other hand, in the second route, Eq. (B.1b), we transform the energy, Eq. (B.7), to the new coordinates,

$$E[\Phi(S)] = \frac{B}{2} \int_0^L \left(\frac{d\Phi}{dS} \right)^2 dS + B(\bar{\kappa} + \kappa) \int_0^L d\Phi + B(\kappa^2/2 + \kappa\bar{\kappa}) \int_0^L dS, \quad (\text{B.9})$$

and minimize with respect to $\Phi(S)$. This gives the equilibrium equation, Eq. (B.6a), and the boundary condition,

$$[d\Phi/dS]_{S=0,L} = -(\bar{\kappa} + \kappa). \quad (\text{B.10})$$

Thus, the solutions from the first and second routes are equivalent and the energy, Eq. (B.7), keeps the canonical invariant property. As in the previous case, it may readily be verified from Eqs. (B.7) and (B.9) that $E[\phi(s)] = E[\Phi(S)] = -(B/2)\bar{\kappa}^2L$.

B.1.2 Extensible Lorentz filament

In order to conserve the total deformed length, \hat{L} , throughout the minimization process we first transform Eq. (3.1) from the relaxed arclength parameter, s , to the compressed one, \hat{s} ,

$$E[\phi(\hat{s}), \gamma(\hat{s})] = \int_0^{\hat{L}} \left[\frac{B}{2} \gamma \left(\frac{d\phi}{d\hat{s}} \right)^2 + \frac{Y}{2} \frac{(\gamma - 1)^2}{\gamma} + V(\phi) \right] d\hat{s}. \quad (\text{B.11})$$

Then, we minimize Eq. (B.11) with respect to \hat{s} ,

$$\gamma = \frac{1}{\sqrt{1 + h^2(d\phi/d\hat{s})^2}}, \quad (\text{B.12})$$

and substitute Eq. (B.12) and $V = 0$ back in Eq. (B.11). This gives,

$$E[\phi(\hat{s})] = Y \int_0^{\hat{L}} \sqrt{1 + h^2(d\phi/d\hat{s})^2} d\hat{s} - Y \int_0^{\hat{L}} d\hat{s}. \quad (\text{B.13})$$

Up to the second term, which is a constant, this energy is analogous to the Lagrangian of a free, relativistic, particle (see Fig. B.1b). As we shall now demonstrate, although this constant

does not affect the minimizing shape in the current coordinates, $\{\hat{s}, \phi\}$, it does have an effect in the new coordinates, $\{\hat{S}, \Phi\}$.

Considering the following Lorentz transformation,

$$d\hat{s}/h = \gamma(d\hat{S}/h) - \gamma h \kappa d\Phi, \quad (\text{B.14a})$$

$$d\phi = \gamma h \kappa (d\hat{S}/h) + \gamma d\Phi, \quad (\text{B.14b})$$

where $\gamma = 1/\sqrt{1 + h^2 \kappa^2}$, we aim to show that Eq. (B.13) is canonically invariant according to our requirement, Eq. (B.1).

Following the first route, Eq. (B.1a), we minimize Eq. (B.13) with respect to $\phi(\hat{s})$ obtaining $d\phi/d\hat{s} = 0$. Lorentz boost of this solution to the new coordinates, Eqs. (B.14), gives,

$$\frac{d\Phi}{d\hat{S}} = -\kappa. \quad (\text{B.15})$$

Following the second route, Eq. (B.1b), we first transform the energy, Eq. (B.13), to the new coordinates,

$$E[\Phi(\hat{S})] = Y \int_0^{\gamma \hat{L}} \sqrt{1 + h^2 (d\Phi/d\hat{S})^2} d\hat{S} + B\gamma\kappa \int_0^{\gamma \hat{L}} d\Phi - Y\gamma \int_0^{\gamma \hat{L}} d\hat{S}, \quad (\text{B.16})$$

and minimize it with respect to $\Phi(\hat{S})$. This yields the following equilibrium equation and boundary condition,

$$\text{equilibrium equation:} \quad \frac{d}{d\hat{S}} \left(\frac{B}{\sqrt{1 + h^2 (d\Phi/d\hat{S})^2}} \frac{d\Phi}{d\hat{S}} \right) = 0, \quad (\text{B.17a})$$

$$\text{boundary condition:} \quad \left[\frac{B}{\sqrt{1 + h^2 (d\Phi/d\hat{S})^2}} \frac{d\Phi}{d\hat{S}} = -B\gamma\kappa \right]_{\hat{S}=0, \gamma \hat{L}}. \quad (\text{B.17b})$$

It can readily be verified that the solution to Eqs. (B.17) is equivalent to Eq. (B.15). Thus, the energy, Eq. (B.13), is canonically invariant under the Lorentz transformation. As in previous cases, one can check that $E[\phi(s)] = E[\Phi(S)] = 0$ upon substitution of the minimizing configurations into Eq. (B.13) and (B.16).

Note the roll of the constant Y in keeping the energy, Eq. (B.13), canonically invariant. This term yields after the transformation the external bending moment, $-B\gamma\kappa$, in the boundary condition, Eq. (B.17b).

We now turn to examine the effect of pure bending moments on the invariance property. It can be shown that adding a constant bending term, $M = B\gamma_{\bar{\kappa}}\bar{\kappa}$ where $\gamma_{\bar{\kappa}} = 1/\sqrt{1 + h^2 \bar{\kappa}^2}$,

alone to Eq. (B.13) breaks the symmetry down. Nevertheless, as we shall now demonstrate, the invariance is preserved if in addition to M we shift the energy by the constant, $P = Y(1 - \gamma_{\bar{\kappa}})$. This constant plays the same roll as Y in Eq. (B.13), although it has no effect in the old coordinates it changes the boundary condition in the new coordinates.

Modifying Eq. (B.13) to include the bending moment, M , and the constant, P , we have,

$$E[\phi(\hat{s})] = Y \int_0^{\hat{L}} \sqrt{1 + h^2(d\phi/d\hat{s})^2} d\hat{s} - Y \int_0^{\hat{L}} d\hat{s} + M \int_0^{\hat{L}} d\phi + P \int_0^{\hat{L}} d\hat{s}, \quad (\text{B.18})$$

Following the first route, Eq. (B.1a), we minimize Eq. (B.18) with respect to $\phi(\hat{s})$ obtaining, $d\phi/d\hat{s} = -M/(B\gamma_{\bar{\kappa}}) = -\bar{\kappa}$. A Lorentz boost of this solution gives,

$$\frac{d\Phi}{d\hat{S}} = -\frac{\bar{\kappa} + \kappa}{1 - h^2\bar{\kappa}\kappa}. \quad (\text{B.19})$$

On the other hand, following the second route, Eq. (B.1b), we transform Eq. (B.18) to the new coordinates,

$$E[\Phi(\hat{S})] = Y \int_0^{\gamma\hat{L}} \sqrt{1 + h^2(d\Phi/d\hat{S})^2} d\hat{S} + (\bar{P} - Y\gamma) \int_0^{\gamma\hat{L}} d\hat{S} + (\bar{M} + B\gamma\kappa) \int_0^{\gamma\hat{L}} d\Phi, \quad (\text{B.20})$$

where $\{\bar{P}, \bar{M}\}$ are related to the $\{P, M\}$ by the following Lorentz-like transformation,

$$\begin{pmatrix} \bar{M}/h \\ \bar{P} \end{pmatrix} = \begin{pmatrix} \gamma & -\gamma h\kappa \\ \gamma h\kappa & \gamma \end{pmatrix} \begin{pmatrix} M/h \\ P \end{pmatrix}. \quad (\text{B.21})$$

Minimization of Eq. (B.20) with respect to $\Phi(\hat{S})$ yields the bulk equation, Eq. (B.17a), and the boundary condition,

$$\left[\frac{B}{\sqrt{1 + h^2(d\Phi/d\hat{S})^2}} \frac{d\Phi}{d\hat{S}} = -(\bar{M} + B\gamma\kappa) \right]_{\hat{S}=0, \gamma\hat{L}}. \quad (\text{B.22})$$

Note that the constant \bar{M} depends on both, M and P , according to the transformation, Eq. (B.21). Thus, the constant, P , which is insignificant in the old coordinates, Eq. (B.18), influence the boundary condition in the new coordinates, Eq. (B.20). As before, one can now check that the solution to this equation is given by Eq. (B.19). Thus, the energy, Eq. (B.18), is canonically invariant under the Lorentz transformation. In addition, we also have that $E[\phi(\hat{s})] = E[\Phi(\hat{S})] = 0$ upon substitution of the minimizing configurations in Eqs. (B.18) and (B.20).

B.1.3 Summary

Let us summarize this discussion with four comments. First, we have shown that both Galilean and Lorentz invariances emerge from Eq. (3.1) depending on the given information prior to

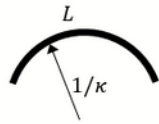
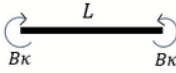
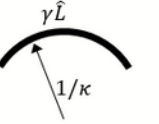
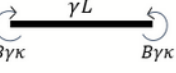
| | Relaxed state | Deformed state with straightening bending moment |
|----------------------------|---|--|
| Galilean invariant element |  |  |
| Lorentz invariant element |  |  |

Figure B.2: Schematic figures of Galilean and Lorentz invariant elements. A Galilean element is a filament that is bent to a constant radius of curvature, $1/\kappa$, at its natural configuration. It becomes equivalent to the flat, zero energy, state once it is subjected to a straightening bending moment, $M = B\kappa$. A Lorentz invariant element is a filament that is curved to a constant radius of curvature, $1/\kappa$, and at the same time compressed to $\gamma\hat{L}$ at its natural configuration. It becomes equivalent to the flat state once it is subjected to a straightening bending moment, $M = B\gamma\kappa$.

minimization. The group of Galilean invariant elements, Eq. (B.3), are filaments that are unstrained and bent to a constant curvature in their natural configuration. They become equivalent to a straight filament once a pure bending moment, $M = B\kappa$ (see Eq. (B.6b)), is acting to flatten them. Similarly, the Lorentz invariant elements, Eq. (B.14), are naturally strained and constantly bend filaments. When a constant bending moment, $M = B\gamma\kappa$ (see Eq. (B.17b)), is acting to straighten them, they become equivalent to a filament that is flat at its rest configuration, see Fig. B.2.

Second, while the Galilean functional, Eq. (B.2), is invariant under an arbitrary shift of the total energy by a constant, the Lorentz functional, Eq. (B.13), is not. This is because the arclength parameter is invariant under the Galilean transformation, Eq. (B.3a), but it is not invariant under the Lorentz transformation, Eq. (B.14a). Nevertheless, the energy, Eq. (B.13) preserves the Lorentz symmetry for a unique selection of the constant shift. The additional constant $-Y$ in Eq. (B.13) and the additional constant P in Eq. (B.18), are two examples for such a unique selection. These constants affect the boundary conditions after the transformation. They correspond to an additional bending moments on the filament edges. It is yet interesting to note that unlike the constant P , the constant $-Y$ is automatically obtained in the second

path of minimization.

Third, when the filament is confined by pure bending moments we find that the Galilean system, Eq. (B.7), preserves its canonical symmetry, while the Lorentz energy, Eq. (B.18), preserves the symmetry only if an additional constant term, P , is added (see discussion in the second comment). Confinement by pure bending moments is equivalent in the kinetic analogy to a constant shift of the particle's velocity. While a velocity addition in the Galilean framework is linear², Eq. (B.8), the Lorentz counterpart, Eq. (B.19), is non-linear.

Fourth, in this Appendix we have only considered free filaments since, in general, the inclusion of a potential term in the elastic energy, $V \neq 0$ in Eq. (3.1), breaks the symmetries down. Nevertheless, it is still intriguing to note that the equilibrium equations in both cases have the same mathematical structure (also see Eq. (3.4) in the main text),

$$\frac{d}{d\hat{s}} \left(\gamma \frac{d\phi}{d\hat{s}} \right) - \frac{dV}{d\phi} = 0. \quad (\text{B.23})$$

Equation (B.23) is the minimizer of the Galilean energy, Eq. (3.1), if γ is given by Eq. (3.5) and the boundary conditions of the problem are prescribed on the undeformed length, L . On the other hand, Eq. (B.23) is the minimizer in the Lorentz case, Eq. (B.11), if γ is given by Eq. (B.12) and the boundary conditions are prescribed on the ultimate deformed length, \hat{L} . Although the two formulas for γ , Eqs. (3.5) and (B.12), differ only by the constant prefactor, $\gamma_0 = \sqrt{1 + 2\mathcal{H}/Y}$, they are significantly different. In the Galilean picture stretching effects take place only when $V \neq 0$, by contrast, in the Lorentz case the stretching field, Eq. (B.12), may differ from unity even in the absence of external fields.

²Since it is linear we can first apply a straightening bending moment, $M = B\kappa$, on the naturally curved filament and once it is straight, add the moment, $M = B\bar{\kappa}$ [21, p. 112].

B.2 Analogy between extensible 3D Kirchhoff's rod and relativistic rotor

In this appendix we derive the equations of equilibrium for a 3D extensible elastic rod under the assumptions of Kirchhoff's model[52, 150]. It is shown that these equations are mathematically analogous to the 3D Euler's equations of rigid-body rotation, where the non-relativistic angular momentum, \mathbf{L} , is replaced by, $\gamma\mathbf{L}$, γ being the Lorentz factor. This analogy is derived while keeping in mind the known difficulties in the latter, relativistic problem [170, 171].

Following the formulation in Ref. [38], we consider a space curve described by the position vector, $\mathbf{f}(s)$, where s is the arclength parameter of the relaxed configuration. Defining \hat{s} as the arclength parameter of the deformed configuration, the unit tangent vector to $\mathbf{f}(s)$ is given by, $\mathbf{d}_3 = d\mathbf{f}/d\hat{s}$. In addition, let $\{\mathbf{d}_1, \mathbf{d}_2\}$ be a pair of unit vectors perpendicular to \mathbf{d}_3 and parallel to the principal axes of the filament's cross-section. The triad $\{\mathbf{d}_1, \mathbf{d}_2, \mathbf{d}_3\}$ form a co-moving coordinate frame attached to the rod's mid-axis. These vectors satisfy the relations,

$$\frac{d\mathbf{d}_i}{ds} = \gamma\boldsymbol{\kappa} \times \mathbf{d}_i, \quad (\text{B.24})$$

where $i = 1, 2, 3$, $\gamma = d\hat{s}/ds$ is the strain field, and $\boldsymbol{\kappa} = \kappa_1\mathbf{d}_1 + \kappa_2\mathbf{d}_2 + \kappa_3\mathbf{d}_3$ is the curvature vector. The local bending moment is given by,

$$\mathbf{M}(s) = B_1(\gamma\kappa_1)\mathbf{d}_1 + B_2(\gamma\kappa_2)\mathbf{d}_2 + B_3(\gamma\kappa_3)\mathbf{d}_3, \quad (\text{B.25})$$

where B_i are bending rigidities.

In correspondence with Eq. (3.1) of the main text, the energy functional of a 3D elastic filament, confined by a boundary constant force \mathbf{P} , is given by $E = \int_0^L e[\boldsymbol{\kappa}(s), \gamma(s)]ds$, where

$$e[\boldsymbol{\kappa}(s), \gamma(s)] = \frac{1}{2}\mathbf{M} \cdot (\gamma\boldsymbol{\kappa}) + \frac{Y}{2}(\gamma - 1)^2 + \gamma\mathbf{d}_3 \cdot \mathbf{P}. \quad (\text{B.26})$$

The appearance of the $\gamma\boldsymbol{\kappa}$ term in the bending energy is a consequence of the requirement to keep bending and stretching contributions independent. Minimizing Eq. (B.26) with respect to γ and κ_i (see Appendix B.3) gives [38],

$$\frac{d\mathbf{M}}{d\hat{s}} - \mathbf{d}_3 \times \mathbf{P} = 0, \quad (\text{B.27a})$$

$$Y(\gamma - 1) + \mathbf{d}_3 \cdot \mathbf{P} = 0. \quad (\text{B.27b})$$

In the inextensible limit Eq. (B.27b) is redundant and Eqs. (B.27a) become analogous to the non-relativistic Euler equations of a 3D rigid body, fixed at one point and rotating under

the influence of an external force (such as gravity) [172, p. 200]. In this analogy, the bending moment takes the role of angular momentum, $\mathbf{M} \leftrightarrow \mathbf{L}$, and the boundary force is analogous to an external torque, $\mathbf{d}_3 \times \mathbf{P} \leftrightarrow \mathbf{N}$. Turning on extensibility effects, we have by Eq. (B.25) that $\mathbf{M} \rightarrow \gamma \mathbf{M}$. Thus, it is left to show that γ coincides with the Lorentz factor. First integration of Eqs. (B.27a) and (B.27b) gives,

$$\mathcal{H} = \frac{1}{2} \mathbf{M} \cdot (\gamma \boldsymbol{\kappa}) - \frac{Y}{2} (\gamma - 1)^2 - \gamma \mathbf{d}_3 \cdot \mathbf{P} = \text{const.} \quad (\text{B.28})$$

Eliminating $\mathbf{d}_3 \cdot \mathbf{P}$ from Eq. (B.28) and substituting in Eq. (B.27b) gives,

$$\gamma = \frac{\sqrt{1 + 2\mathcal{H}/Y}}{\sqrt{1 + \frac{B_1}{Y} \kappa_1^2 + \frac{B_2}{Y} \kappa_2^2 + \frac{B_3}{Y} \kappa_3^2}}. \quad (\text{B.29})$$

This expression extend Eq. (3.5) of the main text to 3D. It indeed resembles the Lorentz factor up to the constant prefactor, $\gamma_0 \equiv \sqrt{1 + 2\mathcal{H}/Y}$, which appears also in the 2D problem, and which can be absorbed in the force \mathbf{P} , (see discussion in the main text).

B.3 Minimization of Eq. (B.26)

In this appendix we minimize Eq. (B.26) with respect to spatial configurations of the elastic filament and show that the equilibrium equations are equivalent to the one considered in (B.27).

Following our formulation in Appendix B.2, a general variation over the spatial configuration, $\mathbf{f}(s)$, is given by,

$$\tilde{\mathbf{f}}(s) = \mathbf{f}(s) + \delta\mathbf{f}(s) = \mathbf{f}(s) + \psi_1(s)\mathbf{d}_1 + \psi_2(s)\mathbf{d}_2 + \psi_3(s)\mathbf{d}_3, \quad (\text{B.30})$$

where $\{\mathbf{d}_1, \mathbf{d}_2, \mathbf{d}_3\}$ is the co-moving coordinate frame and $\{\psi_1, \psi_2, \psi_3\}$ are arbitrary perturbation functions. In this appendix we will denote by a tilde, \tilde{x} , all the components that are calculated in the perturbed configuration, $\tilde{\mathbf{f}}(s)$. Equivalently, up to a shift of the origin, we can represent the variation of the configuration by its derivative, $d\tilde{\mathbf{f}}/ds = d\mathbf{f}/ds + d\delta\mathbf{f}/ds$. Then, the variation of the energy is written as,

$$\delta E = \int (\mathcal{E}_1\mathbf{d}_1 + \mathcal{E}_2\mathbf{d}_2 + \mathcal{E}_3\mathbf{d}_3) \cdot \frac{d\delta\mathbf{f}}{ds} ds, \quad (\text{B.31})$$

where $\mathcal{E}_i = 0$ are the equilibrium equations. In a similar way to our derivations in the case of a planar filament (see Appendix C.1 Eq. (C.8)), it can be shown that the derivative of the perturbation vector is given by,

$$\frac{d\delta\mathbf{f}}{ds} = \gamma\delta\phi_1\mathbf{d}_1 + \gamma\delta\phi_2\mathbf{d}_2 + \delta\gamma\mathbf{d}_3, \quad (\text{B.32})$$

where ϕ_1 and ϕ_2 are two out-of-plane angles.

In our case, the variation of the elastic energy in Kirchhoff's model, Eq. (B.26), reads,

$$\delta e = \mathbf{M} \cdot (\boldsymbol{\kappa}\delta\gamma + \gamma\delta\boldsymbol{\kappa}) + Y(\gamma - 1)\delta\gamma + \delta\gamma\mathbf{d}_3 \cdot \mathbf{P} + \gamma\delta\mathbf{d}_3 \cdot \mathbf{P}. \quad (\text{B.33})$$

where $\delta\boldsymbol{\kappa}$ is the variation of the curvature vector³ and $\delta\mathbf{d}_3 = \tilde{\mathbf{d}}_3 - \mathbf{d}_3$ is the variation of the tangent vector. Thus, in order to find the equilibrium equations, \mathcal{E}_i in Eq. (B.31), we need to express $\delta\boldsymbol{\kappa}$ and $\delta\mathbf{d}_3$ in terms of $\{\gamma\delta\phi_1, \gamma\delta\phi_2, \delta\gamma\}$ (see Eq. (B.32)).

The variation of the tangent vector, \mathbf{d}_3 , can straightforwardly be calculated by,

$$\tilde{\mathbf{d}}_3 = \frac{d\tilde{\mathbf{f}}/ds}{|d\tilde{\mathbf{f}}/ds|} = \mathbf{d}_3 + \delta\phi_1\mathbf{d}_1 + \delta\phi_2\mathbf{d}_2. \quad (\text{B.34})$$

³The components of this vector are $\delta\boldsymbol{\kappa} = (\tilde{\kappa}_1 - \kappa_1, \tilde{\kappa}_2 - \kappa_2, \tilde{\kappa}_3 - \kappa_3)$, where $\tilde{\kappa}_i$ are the components of the curvature vector in the perturbed configuration, $\tilde{\mathbf{f}}(s)$.

In addition to Eq. (B.34), the triad $\{\tilde{\mathbf{d}}_1, \tilde{\mathbf{d}}_2, \tilde{\mathbf{d}}_3\}$ form an orthonormal set if $\tilde{\mathbf{d}}_1$ and $\tilde{\mathbf{d}}_2$ are given by⁴,

$$\tilde{\mathbf{d}}_1 = \mathbf{d}_1 + \xi(s)\mathbf{d}_2 - \delta\phi_1\mathbf{d}_3, \quad (\text{B.35a})$$

$$\tilde{\mathbf{d}}_2 = \mathbf{d}_2 - \xi(s)\mathbf{d}_1 - \delta\phi_2\mathbf{d}_3, \quad (\text{B.35b})$$

where $\xi(s)$ is related to the perturbation functions in a way that is yet to be determined.

Differentiating Eq. (B.34) with respect to s and using Eqs. (B.24) and (B.35), it can be shown that $\tilde{\kappa}_1$ and $\tilde{\kappa}_2$ are given by,

$$\tilde{\kappa}_1 = \kappa_1 - \frac{\kappa_1}{\gamma}\delta\gamma - \frac{1}{\gamma}\frac{d\delta\phi_2}{ds} - \kappa_3\delta\phi_1 + \xi(s)\kappa_2, \quad (\text{B.36})$$

$$\tilde{\kappa}_2 = \kappa_2 - \frac{\kappa_2}{\gamma}\delta\gamma + \frac{1}{\gamma}\frac{d\delta\phi_1}{ds} - \kappa_3\delta\phi_2 - \xi(s)\kappa_1. \quad (\text{B.37})$$

Similarly, differentiating Eq. (B.35a) with respect to s , dotting the resulting equations with $\tilde{\mathbf{d}}_2$, and using Eqs. (B.34) and (B.35b) gives,

$$\tilde{\kappa}_3 = \kappa_3 - \frac{\kappa_3}{\gamma}\delta\gamma + \frac{1}{\gamma}\frac{d\xi}{ds} + \kappa_1\delta\phi_1 + \kappa_2\delta\phi_2. \quad (\text{B.38})$$

Lastly, in Kirchhoff's model the ratio between the two lateral curvatures, κ_1 and κ_2 , is a constant of variation [22]. Thus, $\kappa_1/\kappa_2 = \tilde{\kappa}_1/\tilde{\kappa}_2$ form an equation for the function $\xi(s)$. Its solution reads,

$$\xi(s) = \frac{1}{\kappa_1^2 + \kappa_2^2} \left(\frac{\kappa_1}{\gamma} \frac{d\delta\phi_1}{ds} + \frac{\kappa_2}{\gamma} \frac{d\delta\phi_2}{ds} + \kappa_2\kappa_3\delta\phi_1 - \kappa_1\kappa_3\delta\phi_2 \right). \quad (\text{B.39})$$

Substituting Eqs. (B.34), (B.36), (B.38) and (B.39) in the variation of the energy, Eq. (B.33), we can obtain the minimizing equations, \mathcal{E}_i . Collecting terms that are proportional to $\delta\gamma$ immediately yields Eq. (B.27b). Similarly, collecting terms that are proportional to $\delta\phi_1$ and $\delta\phi_2$ yield, after integration by parts, the two other equations,

$$0 = B_2 \frac{d(\gamma\kappa_2)}{ds} + (B_1 - B_3)\gamma^2\kappa_1\kappa_3 - \gamma\mathbf{d}_1 \cdot \mathbf{P} + \Gamma \frac{\kappa_2\kappa_3}{\kappa_1^2 + \kappa_2^2} - \frac{d}{ds} \left(\Gamma \frac{\kappa_1}{\gamma(\kappa_1^2 + \kappa_2^2)} \right), \quad (\text{B.40a})$$

$$0 = B_1 \frac{d(\gamma\kappa_1)}{ds} + (B_3 - B_2)\gamma^2\kappa_2\kappa_3 + \gamma\mathbf{d}_2 \cdot \mathbf{P} + \Gamma \frac{\kappa_1\kappa_3}{\kappa_1^2 + \kappa_2^2} + \frac{d}{ds} \left(\Gamma \frac{\kappa_2}{\gamma(\kappa_1^2 + \kappa_2^2)} \right), \quad (\text{B.40b})$$

where we have defined,

$$\Gamma \equiv B_3 \frac{d(\gamma\kappa_3)}{ds} + (B_2 - B_1)\gamma^2\kappa_1\kappa_2. \quad (\text{B.41})$$

Equations (B.40) and (B.41) recover the three equations for balance of bending moments, Eqs. (B.27a), once we set $\Gamma = 0$.

⁴We require that to leading order in the perturbation functions $\tilde{\mathbf{d}}_i \cdot \tilde{\mathbf{d}}_j = \delta_{ij}$ where δ_{ij} is the Kronecker delta.

Appendix C

Strain tensor selection - Appendices

C.1 Consistent energy minimization for a uniaxially deformed sheet

In this Appendix we show that minimization of E_{1D} with respect to ϵ_{ss} and ϕ yields equations of equilibrium which are identical to the ones obtained by the appropriate minimization with respect to the spatial configuration, $\mathbf{f}(s)$.

We first define the perturbed configuration, $\tilde{\mathbf{f}}(s)$, by

$$\tilde{\mathbf{f}}(s) = \mathbf{f}(s) + \delta\mathbf{f}(s) = \mathbf{f}(s) + \psi_t(s)\hat{\mathbf{t}} + \psi_n(s)\hat{\mathbf{n}}, \quad (\text{C.1})$$

where $\{\hat{\mathbf{t}}(s), \hat{\mathbf{n}}(s)\}$ are the unit vectors tangent and normal to the sheet along the deformation axis, and ψ_t and ψ_n are arbitrary perturbation functions. Equivalently (up to a shift of the origin), we can represent the configuration by $d\mathbf{f}/ds$, i.e., $d\tilde{\mathbf{f}}/ds = d\mathbf{f}/ds + d\delta\mathbf{f}/ds$. Then, the variation of the energy is written as

$$\delta E_{1D} = \int (\mathcal{E}_t \hat{\mathbf{t}} + \mathcal{E}_n \hat{\mathbf{n}}) \cdot \frac{d\delta\mathbf{f}}{ds} ds, \quad (\text{C.2})$$

where \mathcal{E}_t and \mathcal{E}_n are some functions of ϵ_{ss} and ϕ yet to be determined. We wish to relate the variation $d\delta\mathbf{f}/ds$ with the variations $\delta\epsilon_{ss}$ and $\delta\phi$.

The vectors $\{\hat{\mathbf{t}}(s), \hat{\mathbf{n}}(s)\}$ satisfy the Frenet-Serret formulas [20],

$$\frac{d\hat{\mathbf{t}}}{ds} = (1 + \epsilon_{ss})\kappa\hat{\mathbf{n}} = \frac{d\phi}{ds}\hat{\mathbf{n}}, \quad (\text{C.3a})$$

$$\frac{d\hat{\mathbf{n}}}{ds} = -(1 + \epsilon_{ss})\kappa\hat{\mathbf{t}} = -\frac{d\phi}{ds}\hat{\mathbf{t}}, \quad (\text{C.3b})$$

where $\kappa = d\phi/d\hat{s}$ is the curvature and \hat{s} is the arclength of the deformed configuration, $d\hat{s}/ds = 1 + \epsilon_{ss}$. With the help of Eqs. (C.3), differentiating $\delta\mathbf{f}$ of Eq. (C.1) with respect to s gives

$$\frac{d\delta\mathbf{f}}{ds} = \left(\frac{d\psi_t}{ds} - \frac{d\phi}{ds}\psi_n \right) \hat{\mathbf{t}} + \left(\frac{d\psi_n}{ds} + \frac{d\phi}{ds}\psi_t \right) \hat{\mathbf{n}}. \quad (\text{C.4})$$

Next, we examine the in-plane variation $\delta\epsilon_{ss}$ to leading order in the perturbation functions,

$$\delta\epsilon_{ss} = \left| \frac{d\tilde{\mathbf{f}}}{ds} \right| - \left| \frac{d\mathbf{f}}{ds} \right| \simeq \frac{d\psi_t}{ds} - \frac{d\phi}{ds}\psi_n, \quad (\text{C.5})$$

To do the same for the $\delta\phi$ we start by writing $\cos\phi = \hat{\mathbf{t}} \cdot \hat{\mathbf{x}}$, where $\hat{\mathbf{x}}$ is a constant unit vector along the horizontal direction. Upon variation we have, $-\sin\phi\delta\phi = \delta\hat{\mathbf{t}} \cdot \hat{\mathbf{x}}$. In turn, the variation of the tangent vector is given by,

$$\delta\hat{\mathbf{t}} = \frac{d\tilde{\mathbf{f}}/ds}{|d\tilde{\mathbf{f}}/ds|} - \frac{d\mathbf{f}/ds}{|d\mathbf{f}/ds|} \simeq \frac{1}{1 + \epsilon_{ss}} \left(\frac{d\psi_n}{ds} + \frac{d\phi}{ds}\psi_t \right) \hat{\mathbf{n}}, \quad (\text{C.6})$$

and, since $\hat{\mathbf{n}} \cdot \hat{\mathbf{x}} = -\sin\phi$, we get

$$(1 + \epsilon_{ss})\delta\phi = \frac{d\psi_n}{ds} + \frac{d\phi}{ds}\psi_t. \quad (\text{C.7})$$

Collecting the results for $\delta\epsilon_{ss}$ and $\delta\phi$ (Eqs. (C.5) and (C.7)) and substituting in Eq. (C.4), we obtain the desired relation,

$$\frac{d\delta\mathbf{f}}{ds} = \delta\epsilon_{ss}\hat{\mathbf{t}} + (1 + \epsilon_{ss})\delta\phi\hat{\mathbf{n}}. \quad (\text{C.8})$$

This proves that the variation with respect to the spatial configuration is equivalent to the variation with respect to $\delta\epsilon_{ss}$ and $\delta\phi$.

We can proceed to rewrite the variation of the energy, Eq. (C.2), as

$$\delta E_{1D} = \int [\mathcal{E}_t\delta\epsilon_{ss} + (1 + \epsilon_{ss})\mathcal{E}_n\delta\phi] ds. \quad (\text{C.9})$$

The straightforward way to get the equations of equilibrium is to set this functional to zero for arbitrary $\delta\epsilon_{ss}$ and $\delta\phi$, i.e., $\mathcal{E}_t = 0$ and $\mathcal{E}_n = 0$. This is what has been done in Sec. 4.3, where

$$\mathcal{E}_t = Y\epsilon_{ss} = \sigma_{ss} = 0, \quad (\text{C.10a})$$

$$\mathcal{E}_n = -\frac{B}{1 + \epsilon_{ss}} \frac{d^2\phi}{ds^2} = -\frac{dM_{ss}}{d\hat{s}} = 0. \quad (\text{C.10b})$$

(See Eqs. (4.24) and (4.25).)

Alternatively, we can rewrite the energy variation, Eq. (C.2), in terms of $\delta\mathbf{f}$ rather than $d\delta\mathbf{f}/ds$, using intergration by parts. This yields the equations of equilibrium in the different form,

$$\frac{d\mathcal{E}_t}{ds} - \frac{d\phi}{ds}\mathcal{E}_n = 0, \quad (\text{C.11a})$$

$$\frac{d\mathcal{E}_n}{ds} + \frac{d\phi}{ds}\mathcal{E}_t = 0. \quad (\text{C.11b})$$

Substituting Eqs. (C.10), this gives

$$\frac{d\sigma_{ss}}{d\hat{s}} - \kappa\sigma_{sn} = 0, \quad (\text{C.12a})$$

$$\frac{d\sigma_{sn}}{d\hat{s}} + \kappa\sigma_{ss} = 0, \quad (\text{C.12b})$$

where $\sigma_{sn} = -dM_{ss}/d\hat{s}$ is the normal force at a cross section [22, p. 387].

The difference between the two equivalent sets of equilibrium equations is explained in Fig. C.1. While Eqs. (C.10) represent balance of forces and moments across a finite segment of the sheet, Eqs. (C.12) represent the balance for an infinitesimal segment.

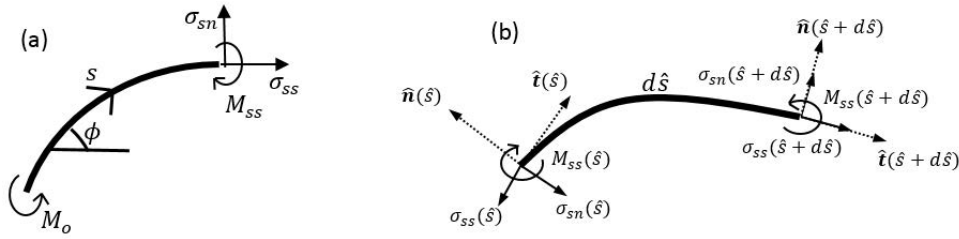


Figure C.1: (a) Schematic force balance on a finite sheet segment. A bending moment, M_o , applied at the boundary, is balanced by the reaction forces, σ_{ss} and σ_{sn} , and the reaction bending moment, M_{ss} . Under these conditions $\sigma_{ss} = \sigma_{sn} = 0$ and $M_{ss} = M_o$, consistently with Eqs. (C.10). (b) Schematic force balance on an infinitesimal sheet segment of length $d\hat{s}$. Balance of forces in the tangential direction, $\hat{\mathbf{t}}(\hat{s})$, is given by, $-\sigma_{ss}(\hat{s}) + \sigma_{ss}(\hat{s} + d\hat{s})\hat{\mathbf{t}}(\hat{s} + d\hat{s}) \cdot \hat{\mathbf{t}}(\hat{s}) + \sigma_{sn}(\hat{s} + d\hat{s})\hat{\mathbf{n}}(\hat{s} + d\hat{s}) \cdot \hat{\mathbf{t}}(\hat{s}) = 0$. Expanding this equation to leading order in the differential $d\hat{s}$ (using Eqs. (C.3)) we obtain $d\sigma_{ss}/d\hat{s} - \kappa\sigma_{sn} = 0$. Similarly, force balance in the normal direction and balance of bending moments gives: $d\sigma_{sn}/d\hat{s} + \kappa\sigma_{ss} = 0$ and $dM_{ss}/d\hat{s} + \sigma_{ns} = 0$, consistently with Eqs. (C.12).

C.2 Boundary layer in a sheet with elliptic reference metric

In this Appendix we show that the energy of the isometric spherical cap, Eq. (4.58), is reduced when a boundary layer is formed (i) near the outer radius of a complete disc, and (ii) near the outer and inner radii of an annulus. The existence of these boundary layers and the scaling of their width with the thickness t were found in Ref. [78]. Here we derive these results based on a variational Ansatz within the FvK approximation, thus obtaining full expressions including prefactors.

Considering the elliptic reference metric, Eq. (4.40), and employing the small-slope approximation, we obtain for the in-plane strains, Eqs. (4.11),

$$\epsilon_{rr} \simeq \partial_r u_r + \frac{1}{2}(\partial_r \zeta)^2, \quad (\text{C.13a})$$

$$\epsilon_{\theta\theta} \simeq \frac{Kr^2}{6} + \frac{u_r}{r}. \quad (\text{C.13b})$$

For the isometric immersion these strains vanish, yielding the height function $\zeta_{iso} \simeq \sqrt{K}r^2/2$. The total energy of the spherical cap is obtained by substituting this function in Eq. (4.21), giving,

$$E_{iso} = \pi(1 + \nu)(KR^2)B. \quad (\text{C.14})$$

Let us try to reduce the total energy below E_{iso} through the following variational Ansatz:

$$\zeta(r) = \zeta_{iso} + \zeta_{bl} = \frac{\sqrt{K}r^2}{2} - \frac{(1 + \nu)}{\alpha(\alpha + \nu - 1)}\sqrt{K}R^2 \left(\frac{r}{R}\right)^\alpha, \quad (\text{C.15})$$

where α serves as a variational parameter. The coefficient of the second term in Eq. (C.15) has been chosen so as to satisfy the boundary condition of zero radial bending moment at the outer radius, $M_{rr}|_{r=R} \simeq B [\partial_{rr}\zeta + \frac{r}{r}\partial_r\zeta]_{r=R} = 0$. When $\alpha \gg 1$ the additional term is negligible everywhere except close to the edge, as expected from a boundary layer. As shown below, the minimizing configuration has $\alpha \sim t^{-1/2}$.

Since our Ansatz, Eq. (C.15), is not an isometry, it contains in-plane stress. To calculate this stress we first minimize the stretching energy, Eq. (4.16), with respect to u_r . In the FvK approximation the resulting equation reads,

$$\partial_r(r\sigma_{rr}) - \sigma_{\theta\theta} = 0. \quad (\text{C.16})$$

Substituting, Eq. (C.15) in the strains, Eqs. (C.13), and then in the stress-strain relations, Eqs. (4.17), we obtain from Eq. (C.16),

$$r\partial_r(r\partial_r u_r) - u_r = -\frac{4}{3}Kr^3 + (1 + \nu)\frac{\alpha - \nu + 1}{\alpha + \nu - 1}KR^3 \left(\frac{r}{R}\right)^{\alpha+1} + \frac{1}{2}(1 + \nu)^2 \frac{\nu - 2\alpha + 1}{(\alpha + \nu - 1)^2}KR^3 \left(\frac{r}{R}\right)^{2\alpha-1}. \quad (\text{C.17})$$

Two boundary conditions are necessary: one is a vanishing stress at the free edge, $\sigma_{rr}|_{r=R} = 0$, and the other is a vanishing displacement at the origin, $u_r|_{r=0} = 0$. The solution of Eq. (C.17) subject to these conditions is,

$$u_r(r) = A_0 r - \frac{K}{6}r^3 + \frac{(1 + \nu)(\alpha - \nu + 1)}{\alpha(\alpha + 2)(\alpha + \nu - 1)}KR^3 \left(\frac{r}{R}\right)^{\alpha+1} + \frac{1}{8} \frac{(1 + \nu)^2(\nu - 2\alpha + 1)}{\alpha(\alpha - 1)(\alpha + \nu - 1)^2}KR^3 \left(\frac{r}{R}\right)^{2\alpha-1}, \quad (\text{C.18})$$

where A_0 is determined by the first boundary condition.

Substituting u_r and ζ from Eqs. (C.15) and (C.18), in Eqs. (4.16) and (4.21), and expanding to leading order in $1/\alpha$, gives,

$$E \simeq \frac{\pi}{2} Y R^2 (K R^2)^2 (1 - \nu)(1 + \nu)^3 \alpha^{-5} + \pi(1 + \nu)(K R^2) B - \frac{3\pi}{2} (1 + \nu)^2 (K R^2) B \alpha^{-1}, \quad (\text{C.19})$$

where the first term comes from stretching and the last two are bending contributions. Minimization of Eq. (C.19) with respect to α yields,

$$\alpha = (5/3)^{1/4} (1 - \nu^2)^{1/4} (K R^2)^{1/4} (Y R^2 / B)^{1/4} = (20)^{1/4} (1 - \nu^2)^{1/4} (K R^2)^{1/4} (t/R)^{-1/2}. \quad (\text{C.20})$$

Substituting this result in Eq. (C.19) we finally obtain,

$$E \simeq E_{iso} - \frac{6\pi}{5} \left(\frac{3}{5}\right)^{1/4} \frac{(1 + \nu)^2}{(1 - \nu^2)^{1/4}} (K R^2)^{3/4} \left(\frac{B}{Y R^2}\right)^{1/4} B, \quad (\text{C.21})$$

where E_{iso} is given by Eq. (C.14). Thus, the energy of the isometric immersion is reduced by the introduction of a boundary layer. The reduction scales as $t^{7/2}$ whereas $E_{iso} \sim t^3$. In the limit of small thickness we can write $\zeta_{bl}(r) \simeq -\frac{(1+\nu)\sqrt{K}R^2}{\alpha^2} e^{-(R-r)/w}$ with the width of the boundary layer being,

$$w = R/\alpha = (20)^{-1/4} (1 - \nu^2)^{-1/4} (K R^2)^{-1/4} (t/R)^{1/2} R. \quad (\text{C.22})$$

This derivation can straightforwardly be extended to the more general case of an annulus with inner radius R_i and outer radius R_o . In this case the energy of the isometric immersion, ζ_{iso} , is given by,

$$E_{iso} = \pi(1 + \nu) K (R_o^2 - R_i^2) B. \quad (\text{C.23})$$

This energy can be reduced below E_{iso} if two boundary layers are formed near the outer and inner radii, as indicated by the following Ansatz,

$$\zeta(r) = \zeta_{iso} + \zeta_{bl} = \frac{\sqrt{K} r^2}{2} + A_o \left(\frac{r}{R_o}\right)^\alpha + B_o \left(\frac{R_i}{r}\right)^\alpha. \quad (\text{C.24})$$

As in the case of a disc, A_o and B_o are chosen such that the radial bending moment is zero at the two boundaries, $M_{rr}|_{r=R_i, R_o} = 0$. This gives,

$$A_o = -\sqrt{K} R_o^2 \frac{1 + \nu}{\alpha(\alpha + \nu - 1)} \frac{1 - \rho^{\alpha+2}}{1 - \rho^{2\alpha}}, \quad (\text{C.25a})$$

$$B_o = -\sqrt{K} R_i^2 \frac{1 + \nu}{\alpha(\alpha - \nu + 1)} \frac{1 - \rho^{\alpha-2}}{1 - \rho^{2\alpha}}, \quad (\text{C.25b})$$

where $\rho \equiv R_i/R_o$.

Following the same route as in Eqs. (C.16)-(C.18), we find after expansion in powers of α^{-1} and assuming $\rho^\alpha \rightarrow 0$ that the total energy of the annulus is given by,

$$\begin{aligned} E &\simeq \frac{\pi}{2} Y R_o^2 (K R_o^2)^2 (1 + \rho^6) (1 - \nu)(1 + \nu)^3 \alpha^{-5} + \pi(1 + \nu) K (R_o^2 - R_i^2) B \\ &- \frac{3\pi}{2} (1 + \nu)^2 (K R_o^2) (1 + \rho^2) B \alpha^{-1}. \end{aligned} \quad (\text{C.26})$$

Minimization of this energy with respect to α gives,

$$\begin{aligned}\alpha &= (5/3)^{1/4}(1-\nu^2)^{1/4} \left(\frac{1+\rho^6}{1+\rho^2}\right)^{1/4} (KR_o^2)^{1/4} \left(\frac{YR_o^2}{B}\right)^{1/4} \\ &= (20)^{1/4}(1-\nu^2)^{1/4} \left(\frac{1+\rho^6}{1+\rho^2}\right)^{1/4} (KR_o^2)^{1/4} \left(\frac{t}{R_o}\right)^{-1/2}.\end{aligned}\quad (\text{C.27})$$

Note that in the limit of $\rho \rightarrow 0$ this result coincides with Eq. (C.20). Substituting Eq. (C.27) back in the energy, Eq. (C.26), we obtain,

$$E \simeq E_{iso} - \frac{6\pi}{5} \left(\frac{3}{5}\right)^{1/4} \frac{(1+\nu)^2}{(1-\nu^2)^{1/4}} (KR_o^2)^{3/4} \frac{(1+\rho^2)^{5/4}}{(1+\rho^6)^{1/4}} \left(\frac{B}{YR_o^2}\right)^{1/4} B, \quad (\text{C.28})$$

where E_{iso} is given by Eq. (C.23). Thus, the introduction of two boundary layers, at the inner and outer radii of the annulus, reduce the energy of an isometric immersion.

C.3 Stability criterion for isometric immersions with negative Gaussian curvature

In this appendix we extend the theory presented in Sec. 4.2 to surfaces of revolution, [see Eq. (4.4)], whose reference metric is given by,

$$\bar{g}_{\alpha\beta} = \begin{pmatrix} \bar{g}_r^2 & 0 \\ 0 & \bar{g}_\theta^2 \end{pmatrix}, \quad ds^2 = \bar{g}_r^2(r)dr^2 + \bar{g}_\theta^2(r)d\theta^2. \quad (\text{C.29})$$

Our aim is to derive a self-consistent stability criterion, similar to Eqs. (4.56), for isometric immersions with constant negative Gaussian curvature [81].

Following Sec. 4.2 it is straightforward to show that the energy functional, Eq. (4.15), is modified into,

$$E = \frac{Y}{2} \int_0^R \int_0^{2\pi} [\epsilon_{rr}^2 + \epsilon_{\theta\theta}^2 + 2\nu\epsilon_{rr}\epsilon_{\theta\theta}] \bar{g}_r\bar{g}_\theta d\theta dr + \frac{B}{2} \int_0^R \int_0^{2\pi} [\phi_{rr}^2 + \phi_{\theta\theta}^2 + 2\nu\phi_{rr}\phi_{\theta\theta}] \bar{g}_r\bar{g}_\theta d\theta dr, \quad (\text{C.30})$$

where the in-plane strains are given by,

$$\epsilon_{rr} = \sqrt{a_{rr}/\bar{g}_r} - 1 = \sqrt{(1 + \partial_r u_r)^2 + (\partial_r \zeta)^2}/\bar{g}_r - 1, \quad (\text{C.31a})$$

$$\epsilon_{\theta\theta} = \sqrt{a_{\theta\theta}/\bar{g}_\theta} - 1 = (r + u_r)/\bar{g}_\theta - 1, \quad (\text{C.31b})$$

and the ‘‘bending-strains’’, are given by,

$$\phi_{rr} = \sqrt{c_{rr}/\bar{g}_r} = \frac{1}{\bar{g}_r} \frac{(1 + \partial_r u_r)\partial_{rr}\zeta - \partial_{rr}u_r\partial_r\zeta}{(1 + \partial_r u_r)^2 + (\partial_r \zeta)^2} = \partial_r \phi^r / \bar{g}_r, \quad (\text{C.32a})$$

$$\phi_{\theta\theta} = \sqrt{c_{\theta\theta}/\bar{g}_\theta} = \frac{1}{\bar{g}_\theta} \frac{\partial_r \zeta}{\sqrt{(1 + \partial_r u_r)^2 + (\partial_r \zeta)^2}} = \sin \phi^r / \bar{g}_\theta. \quad (\text{C.32b})$$

Setting Eqs. (C.31) to zero, we obtain the displacement corresponding to the isometric immersion of Eq. (C.29),

$$u_r = \bar{g}_\theta - r, \quad (\text{C.33a})$$

$$\partial_r \zeta = \sqrt{\bar{g}_r^2 - (\partial_r \bar{g}_\theta)^2}. \quad (\text{C.33b})$$

Following the analysis in Sec. 4.5, we minimize the bending energy,

$$E_b = \frac{1}{2} \int_0^R \int_0^{2\pi} [M_{rr} \partial_r \phi^r / \bar{g}_r + M_{\theta\theta} \sin \phi^r / \bar{g}_\theta] \bar{g}_r \bar{g}_\theta d\theta dr,$$

with respect to ϕ^r to obtain the balance of bending moments. This gives,

$$\partial_r (\bar{g}_\theta M_{rr}) - \bar{g}_r \cos \phi^r M_{\theta\theta} = 0. \quad (\text{C.34})$$

where $M_{\alpha\beta}$ are given by Eqs. (4.19) and $\phi_{\alpha\beta}$ are given by Eqs. (C.32).

Substituting the displacements of Eqs. (C.33) in the ‘‘bending strains’’, Eqs. (C.32), we obtain,

$$\phi_{rr} = \left(\partial_r \bar{g}_\theta \partial_r \sqrt{\bar{g}_r^2 - (\partial_r \bar{g}_\theta)^2} - \partial_{rr} \bar{g}_\theta \sqrt{\bar{g}_r^2 - (\partial_r \bar{g}_\theta)^2} \right) / \bar{g}_r^3, \quad (\text{C.35a})$$

$$\phi_{\theta\theta} = \sqrt{\bar{g}_r^2 - (\partial_r \bar{g}_\theta)^2} / (\bar{g}_r \bar{g}_\theta). \quad (\text{C.35b})$$

In addition, using Eq. (C.32b), we have that,

$$\cos \phi^r = \partial_r \bar{g}_\theta / \bar{g}_r. \quad (\text{C.36})$$

Substituting Eqs. (C.35) in (4.19) and then, along with Eq. (C.36), in (C.34) we finally obtain the self-consistency condition,

$$\partial_r \left(\bar{g}_\theta \left(\partial_r \bar{g}_\theta \partial_r \sqrt{\bar{g}_r^2 - (\partial_r \bar{g}_\theta)^2} - \partial_{rr} \bar{g}_\theta \sqrt{\bar{g}_r^2 - (\partial_r \bar{g}_\theta)^2} \right) / \bar{g}_r^3 \right) - \partial_r \bar{g}_\theta \sqrt{\bar{g}_r^2 - (\partial_r \bar{g}_\theta)^2} / (\bar{g}_r \bar{g}_\theta) = 0. \quad (\text{C.37})$$

It is now straightforward to verify that a pseudosphere, $\bar{g}_r = \tanh r$ and $\bar{g}_\theta = 1/\cosh r$, and hyperboloid of revolution, $\bar{g}_r = b \operatorname{sn}(r, b)$ and $\bar{g}_\theta = \operatorname{dn}(r, b)$ (sn and dn denoting the Jacobi elliptic functions [124]), both do not satisfy Eq. (C.37). Thus, both are mechanically unstable. As in the case of the cone, we note that these conclusions do not rule out the possibility that the objects approach these shapes in the limit $t \rightarrow 0$.

C.4 Comparison between thin sheet theories based on model-independent force-balance equations

As has been demonstrated in the main text by several examples, the ESK model and the present one produce different equations of equilibrium and different equilibrium configurations. Yet, obviously, both models describe balance of forces and torques. Therefore, using an appropriate representation, both should result in identical (albeit not equivalent) equations of equilibrium. Thus the lack of equivalence would be confined to the relations between stress and deformation (the constitutive relations), and we would get an instructive comparison of the stress and torque under similar loading conditions in the two models. Such a representation is the goal of this Supplemental Material.

While the present model is based on the Biot strain measure, Eq. (4.10), the ESK theory [68] is based on the second Piola-Kirchhoff strain, Eq. (4.1). As a result, our equilibrium equations, Eqs. (4.32) and (4.53a), manifestly differ from the ones obtained in Ref. [68], Eq. (3.10) in that paper.

To derive the conditions of force and torque balance we first define the co-moving coordinate system $\{\hat{\mathbf{t}}_r, \hat{\mathbf{t}}_\theta, \hat{\mathbf{n}}\}$, where $\hat{\mathbf{t}}_\alpha = \partial_\alpha \mathbf{f} / |\partial_\alpha \mathbf{f}|$ are two in-plane unit vectors and $\hat{\mathbf{n}}$ is the unit normal, given the spatial configuration $\mathbf{f}(r, \theta)$. Second, we cut an infinitesimal patch of the surface, whose borders lie along lines of constant coordinates [15, p. 24], and balance the force and torque vectors applied on its edges. This gives [15, p. 29],

$$0 = \partial_r(\Phi \mathbf{F}_r) + \partial_\theta \mathbf{F}_\theta, \quad (\text{C.38a})$$

$$0 = \partial_r(\Phi \mathbf{M}_r) + \partial_\theta \mathbf{M}_\theta - \Phi \partial_r \mathbf{f} \times \mathbf{F}_r - \partial_\theta \mathbf{f} \times \mathbf{F}_\theta, \quad (\text{C.38b})$$

where \mathbf{F}_α and \mathbf{M}_α are the forces and bending moments per undeformed unit length along the directions $\alpha = r, \theta$. Lastly, we resolve the components of these vectors projected on our triad basis,

$$\mathbf{F}_\alpha = \sigma_{\alpha r} \hat{\mathbf{t}}_r + \sigma_{\alpha \theta} \hat{\mathbf{t}}_\theta + \sigma_{\alpha 3} \hat{\mathbf{n}}, \quad (\text{C.39a})$$

$$\mathbf{M}_\alpha = \hat{\mathbf{n}} \times (M_{\alpha r} \hat{\mathbf{t}}_r + M_{\alpha \theta} \hat{\mathbf{t}}_\theta). \quad (\text{C.39b})$$

Note the delicate point, crucial for the sake of this section, that the tensors $\sigma_{\alpha\beta}$ and $M_{\alpha\beta}$ here correspond to the *actual* forces and torques, i.e., the fluxes of linear and angular momenta. As such, they do not depend on the choice of model; unlike Eqs. (4.17) and (4.19) in the main

text, we do not relate them at this moment to a certain definition of strain. In other words, they are not necessarily equal to the variation of the energy of the chosen model with respect to the strain and curvature of that model. Similarly, the configuration is represented in these equations through the model-independent spatial triad $\{\hat{\mathbf{t}}_r, \hat{\mathbf{t}}_\theta, \hat{\mathbf{n}}\}$.

For axisymmetric deformations, Eq. (4.4), we always have $\sigma_{r\theta} = M_{r\theta} = 0$, and Eqs. (C.38) and (C.39) form a system of five differential equations for the eight unknowns, $\{\sigma_{\alpha\alpha}, \sigma_{\alpha 3}, M_{\alpha\alpha}, u_r, \zeta\}$, where the configuration is now represented by the displacements u_r and ζ , obtainable from $\{\hat{\mathbf{t}}_r, \hat{\mathbf{t}}_\theta, \hat{\mathbf{n}}\}$. Thus, to have a closure we must derive constitutive relations between the stress and torque components and the actual deformation.

The definition of mechanical energy, as well, does not depend on the choice of model. It is the sum of two terms: (i) The work done by in-plane forces to displace the sheet from its rest state to the given configuration (not displacement squared), and (ii) the work done by bending moments to change the out-of-plane angles from their rest values. For clarity of the expressions that follow, it is helpful to represent the displacements equivalently by in-plane stretching fields, $\gamma_{\alpha\alpha} \equiv \sqrt{a_{\alpha\alpha}/\bar{g}_{\alpha\alpha}}$, and out-of-plane bending fields, $\bar{g}_{\alpha\alpha}\phi_{\alpha\alpha} \equiv b_{\alpha\alpha}/\gamma_{\alpha\alpha}$ (where $\alpha = r, \theta$, and the mixed terms vanish by axisymmetry). The variation of the energy is given then by the infinitesimal work,

$$\delta E = \int_0^R \int_0^{2\pi} (\sigma_{\alpha\beta} \delta\gamma_{\alpha\beta} + M_{\alpha\beta} \delta\phi_{\alpha\beta}) \Phi dr d\theta. \quad (\text{C.40})$$

We note that Eq. (C.40) is the 2D extension of the so-called principle of virtual work [29, 34]. In addition, similar to our proof in Appendix A it can be shown that $\delta\gamma_{\alpha\beta}$ and $\delta\phi_{\alpha\beta}$ are consistent with minimization of the energy with respect to the configuration. These infinitesimals are proportional to the 1D variations, $\delta\epsilon_{ss}$ and $\delta\phi$, considered in Sec. 4.3.

If we now consider the energy functional of each model, express it in terms of the actual deformation fields $\gamma_{\alpha\alpha}$ and $\phi_{\alpha\alpha}$, and take the variation with respect to these fields, we will get the constitutive relations for the actual stresses and bending moments, as arising from each model.

The energy functional of the present model (Eq. (4.15)) is rewritten in terms of the deformation fields as

$$\begin{aligned} E_{2\text{D}} &= \frac{Y}{2} \int_0^R \int_0^{2\pi} [(\gamma_{rr} - 1)^2 + (\gamma_{\theta\theta} - 1)^2 + 2\nu(\gamma_{rr} - 1)(\gamma_{\theta\theta} - 1)] \Phi d\theta dr \\ &+ \frac{B}{2} \int_0^R \int_0^{2\pi} [\phi_{rr}^2 + \phi_{\theta\theta}^2 + 2\nu\phi_{rr}\phi_{\theta\theta}] \Phi d\theta dr. \end{aligned} \quad (\text{C.41})$$

Variations with respect to $\gamma_{\alpha\alpha}$ and $\phi_{\alpha\alpha}$ give

$$\sigma_{rr} = Y [(\gamma_{rr} - 1) + \nu(\gamma_{\theta\theta} - 1)], \quad (\text{C.42a})$$

$$\sigma_{\theta\theta} = Y [(\gamma_{\theta\theta} - 1) + \nu(\gamma_{rr} - 1)], \quad (\text{C.42b})$$

$$M_{rr} = B(\phi_{rr} + \nu\phi_{\theta\theta}), \quad (\text{C.42c})$$

$$M_{\theta\theta} = B(\phi_{\theta\theta} + \nu\phi_{rr}). \quad (\text{C.42d})$$

The energy functional of the ESK model is obtained by specializing Eq. (4.2) to the axisymmetric case and re-expressing it in terms of the deformation fields, yielding

$$\begin{aligned} \text{ESK: } E_{2D} = & \frac{Y}{8} \int_0^R \int_0^{2\pi} [(\gamma_{rr}^2 - 1)^2 + (\gamma_{\theta\theta}^2 - 1)^2 + 2\nu(\gamma_{rr}^2 - 1)(\gamma_{\theta\theta}^2 - 1)] \Phi d\theta dr \\ & + \frac{B}{2} \int_0^R \int_0^{2\pi} [(\gamma_{rr}\phi_{rr})^2 + (\gamma_{\theta\theta}\phi_{\theta\theta})^2 + 2\nu(\gamma_{rr}\phi_{rr})(\gamma_{\theta\theta}\phi_{\theta\theta})] \Phi d\theta dr. \end{aligned} \quad (\text{C.43})$$

Variations of this energy with respect to $\gamma_{\alpha\alpha}$ and $\phi_{\alpha\alpha}$ give

$$\text{ESK: } \sigma_{rr} = \frac{Y}{2} \gamma_{rr} [(\gamma_{rr}^2 - 1) + \nu(\gamma_{\theta\theta}^2 - 1)] + B\phi_{rr} (\gamma_{rr}\phi_{rr} + \nu\gamma_{\theta\theta}\phi_{\theta\theta}), \quad (\text{C.44a})$$

$$\sigma_{\theta\theta} = \frac{Y}{2} \gamma_{\theta\theta} [(\gamma_{\theta\theta}^2 - 1) + \nu(\gamma_{rr}^2 - 1)] + B\phi_{\theta\theta} (\gamma_{\theta\theta}\phi_{\theta\theta} + \nu\gamma_{rr}\phi_{rr}), \quad (\text{C.44b})$$

$$M_{rr} = B\gamma_{rr} (\gamma_{rr}\phi_{rr} + \nu\gamma_{\theta\theta}\phi_{\theta\theta}), \quad (\text{C.44c})$$

$$M_{\theta\theta} = B\gamma_{\theta\theta} (\gamma_{\theta\theta}\phi_{\theta\theta} + \nu\gamma_{rr}\phi_{rr}). \quad (\text{C.44d})$$

The comparison between the constitutive relations in Eqs. (C.42) and Eqs. (C.44) underlines once again the difference between the two models. While the former relations are linear, the latter are nonlinear; while in the former $\sigma_{\alpha\alpha}$ depend only on $\gamma_{\alpha\alpha}$ and $M_{\alpha\alpha}$ depend only on $\phi_{\alpha\alpha}$, in the latter there are mixed terms.

A natural question then is how the actual stresses given by these relations correspond to the ones obtained by variation of the energy with respect to the strain as it is defined in each model. In the present model they are identical; compare Eqs. (C.42) to Eqs. (4.17) and (4.19). This is because the relation between $\gamma_{\alpha\alpha}$ and the strain $\epsilon_{\alpha\alpha}$ used in this model is linear; hence, $\delta\epsilon_{\alpha\alpha} = \delta\gamma_{\alpha\alpha}$. The stress and moments tensors, $s^{\alpha\alpha}$ and $m^{\alpha\alpha}$, which were defined in Ref. [68] differ from the actual ones, Eqs. (C.44). The stress, $s^{\alpha\alpha}$, is based on variation of the energy with respect to the strain $\tilde{\epsilon}_{\alpha\alpha}$ and the bending moment, $m^{\alpha\alpha}$, is based on variation of the energy with respect to the second fundamental form $b_{\alpha\alpha}$. The two sets of stresses and bending moments,

$\{\sigma_{\alpha\alpha}, M_{\alpha\alpha}\}$ from Eqs. (C.44) and $\{s^{\alpha\alpha}, m^{\alpha\alpha}\}$ are inter-related according to

$$\text{ESK: } \sigma_{rr} = \gamma_{rr}s^{rr} + \phi_{rr}m^{rr}, \quad (\text{C.45a})$$

$$\sigma_{\theta\theta} = \Phi^2(\gamma_{\theta\theta}s^{\theta\theta} + \phi_{\theta\theta}m^{\theta\theta}), \quad (\text{C.45b})$$

$$M_{rr} = \gamma_{rr}m^{rr}, \quad (\text{C.45c})$$

$$M_{\theta\theta} = \Phi^2\gamma_{\theta\theta}m^{\theta\theta}. \quad (\text{C.45d})$$

In summary, the equations of equilibrium (C.38b) and (C.39b) are model-independent and, in particular, common to the two models compared here. They become different only once the different constitutive relations, either (C.42) or (C.44), are substituted in them. Upon this substitution, one obtains the equations of equilibrium, predicted by the respective model from minimization of its respective energy over spatial configurations \mathbf{f} . We now demonstrate it in two examples.

C.4.1 Flat deformations

In the case of flat deformations, $\zeta = 0$, we have from both models, $M_{\alpha\alpha} = 0$. Substituting this result in the torque balance equation (C.38b), we get also that the normal stresses vanishing, $\sigma_{\alpha 3} = 0$. In addition, for the case of planar axisymmetric deformations Eq. (C.38a) is automatically satisfied in the tangential and normal directions. Thus, the only non-vanishing equation is the balance of forces in the radial direction, which reads,

$$\partial_r(\Phi\sigma_{rr}) - \sigma_{\theta\theta} = 0. \quad (\text{C.46})$$

This recovers Eq. (4.31) of the main text. Since we have not yet used a constitutive relation, this equation holds also in the ESK model.

Substituting in Eq. (C.46) the constitutive relations of the present model, Eqs. (C.42a) and (C.42b), we recover the linear equilibrium equation of the main text, Eq. (4.32). Repeating the same using the ESK constitutive relations (C.44a) and (C.44b), we obtain

$$\partial_r(\Phi\gamma_{rr}s^{rr}) - \Phi^2\gamma_{\theta\theta}s^{\theta\theta} = 0, \quad (\text{C.47})$$

where the ESK stresses of Eq. (C.45) have been used. Finally, introducing the Christoffel symbols, $\Gamma_{rr}^r = \partial_r\gamma_{rr}/\gamma_{rr}$ and $\Gamma_{\theta\theta}^r = -\Phi\gamma_{\theta\theta}/\gamma_{rr}$, we recover Eq. (7) of Ref. [78],

$$\frac{1}{\Phi}\partial_r(\Phi s^{rr}) + \Gamma_{rr}^r s^{rr} + \Gamma_{\theta\theta}^r s^{\theta\theta} = 0. \quad (\text{C.48})$$

This equation exhibits the covariant form of the ESK theory. At the same time it has the disadvantage of being nonlinear in the displacement, u_r , compared to the present model's linear Eq. (4.32).

C.4.2 Normal force balance in an isometric immersion

As a second example we return to the issue addressed in Sec. 4.5, i.e., the balance of normal forces in the spherical-cap isometry of a sheet with elliptic reference metric. Once again, we apply the different sets of constitutive relations of the two models to the model-independent equations of equilibrium, and compare the results. In the ESK case this procedure recovers, here based on force balance, the first of Eqs. (3.10) in Ref. [68]. In the present model it leads to a different equation of equilibrium. The two equations disagree concerning the balance of normal forces in an isometric spherical cap, as presented in Sec. 4.5. The spherical cap satisfies the present equation and does not satisfy the ESK one. As will be shown below, this disagreement arises from the additional coupling terms between stretching and bending appearing in Eqs. (C.44a) and (C.44b).

To derive the equation of normal force balance we first project Eq. (C.38a) onto the normal direction, and Eq. (C.38b) onto the tangential direction,

$$0 = \frac{1}{\Phi} \partial_r (\Phi \sigma_{r3}) + \sigma_{rr} \phi_{rr} + \sigma_{\theta\theta} \phi_{\theta\theta}, \quad (\text{C.49a})$$

$$\gamma_{rr} \Phi \sigma_{r3} = -\partial_r (\Phi M_{rr}) + M_{\theta\theta} \cos \phi^r. \quad (\text{C.49b})$$

(The geometrical meaning of $\cos \phi^r$ is explained in Fig. 4.1 of the main text.) Eliminating σ_{r3} gives,

$$0 = \frac{1}{\Phi} \partial_r \left[\frac{1}{\gamma_{rr}} (\partial_r (\Phi M_{rr}) - M_{\theta\theta} \cos \phi^r) \right] - \sigma_{rr} \phi_{rr} - \sigma_{\theta\theta} \phi_{\theta\theta}. \quad (\text{C.50})$$

Equation (C.50) expresses normal force balance regardless of model.

Now, we substitute in Eq. (C.50) the constitutive relations of the present model, Eqs. (C.42). For isometric immersion $\gamma_{rr} = \gamma_{\theta\theta} = 1$, we have from Eqs. (C.42a) and (C.42b) that $\sigma_{\alpha\alpha} = 0$. As a result, Eq. (C.50) can be integrated, thus recovering, for free boundary conditions, Eq. (4.53a) of the main text. As discussed in Sec. 4.5, this equation of normal force balance is satisfied by the spherical cap isometry, Eq. (4.58).

Now we substitute in Eq. (C.50) the ESK constitutive relations Eqs. (C.44). This gives

$$0 = \frac{1}{\Phi} \partial_r \left[\Phi \left(\frac{1}{\Phi} \partial_r (\Phi m^{rr}) + \Gamma_{rr}^r m^{rr} + \Gamma_{\theta\theta}^r m^{\theta\theta} \right) \right] - s^{rr} b_{rr} - s^{\theta\theta} b_{\theta\theta} - m^{rr} c_{rr} - m^{\theta\theta} c_{\theta\theta}, \quad (\text{C.51})$$

where $c_{\alpha\alpha} = \bar{g}_{\alpha\alpha} \phi_{\alpha\alpha}^2$, and the Christoffel symbols have been used again, $\Gamma_{rr}^r = \partial_r \gamma_{rr} / \gamma_{rr}$, $\Gamma_{\theta\theta}^r = -(\Phi \gamma_{\theta\theta} / \gamma_{rr}) \cos \phi^r$.

For the isometry, $\gamma_{\alpha\alpha} = 1$, we have from Eqs. (C.45) that $M_{rr} = m^{rr}$ and $M_{\theta\theta} = \Phi^2 m^{\theta\theta}$. As a result, the first terms in Eqs. (C.51) and (C.50) become equal, and the terms $s^{\alpha\alpha} b_{\alpha\alpha}$ and $\sigma_{\alpha\alpha} \phi_{\alpha\alpha}$ in the two equations vanish. However, the last terms in Eq. (C.51), $m^{\alpha\alpha} c_{\alpha\alpha}$, do not have a counterpart in the general equation of normal force balance (C.50). They originate in the bending contributions appearing in the ESK stresses of Eqs. (C.45) or (C.44), compared to those of Eqs. (C.42). They do not vanish for an isometry, leaving $\sigma_{rr} = \phi_{rr} M_{rr}$ and $\sigma_{\theta\theta} = \phi_{\theta\theta} M_{\theta\theta}$. Upon substitution of the spherical cap, Eq. (4.58), in Eq. (C.51), the terms $m^{\alpha\alpha} c_{\alpha\alpha}$ remain finite, and normal force balance is not satisfied.

Bibliography

- [1] M. C. Cross and P. C. Hohenberg, *Rev. Mod. Phys.* **65**, 851 (1993).
- [2] J. P. Gollub and J. S. Langer, *Rev. Mod. Phys.* **71**, S396 (1999).
- [3] D. Walgraef, *Spatio-Temporal Pattern Formation* (Springer, 1996).
- [4] Z. C. Tu and Z. C. Ou-Yang, *J. Comput. Theor. Nanosci.* **5**, 422 (2008).
- [5] F. Tanaka and H. Takahashi, *J. Chem. Phys.* **83**, 6017 (1985).
- [6] B. I. Yakobson, C. J. Brabec, and J. Bernholc, *Phys. Rev. Lett.* **76**, 2511 (1996).
- [7] E. Cerda and L. Mahadevan, *Phys. Rev. Lett.* **90**, 074302 (2003).
- [8] E. Hohlfeld and L. Mahadevan, *Phys. Rev. Lett.* **106**, 105702 (2011).
- [9] N. S. Gov and S. A. Safran, *Biophys J.* **88**, 1859 (2005).
- [10] R. D. Schroll, E. Katifori, and B. Davidovitch, *Phys. Rev. Lett.* **106**, 074301 (2011).
- [11] B. Davidovitch, R. D. Schroll, D. Vella, M. Adda-Bedia, and E. A. Cerda, *Proc. Natl. Acad. Sci.* **108**, 18227 (2011).
- [12] B. Davidovitch, R. D. Schroll, and E. Cerda, *Phys. Rev. E* **85**, 066115 (2012).
- [13] E. Cerda and L. Mahadevan, *Proc. Math. Phys. Eng. Sci.* **461**, 671 (2005).
- [14] T. A. Witten, *Rev. Mod. Phys.* **79**, 643 (2007).
- [15] A. L. Gol'Denveizer, *Theory of Elastic Thin Shells* (Pergamon, 1961).
- [16] F. John, *Comm. Pure Appl. Math.* **18**, 235 (1965).
- [17] W. T. Koiter and J. G. Simmonds, “Theoretical and applied mechanics: Proceedings of the 13th international congress of theoretical and applied mechanics, moscow university, august 21–16, 1972,” (Springer Berlin Heidelberg, Berlin, Heidelberg, 1973) pp. 150–176.

- [18] E. Reissner, *Ingenieur-Archiv* **40**, 402 (1971).
- [19] L. D. Landau and E. M. Lifshitz, *Theory of Elasticity 3rd Edition* (Butterworth-Heinemann, 1986).
- [20] M. M. Lipschutz, *Theory and problems of differential geometry (Schaum's outline series)* (McGraw-Hill, 1969).
- [21] W. A. Oldfather, C. A. Ellis, and D. M. Brown, *Isis* **20**, 72 (1933).
- [22] A. E. H. Love, *A Treatise on the Mathematical Theory of Elasticity* (Dover Publications, 1927).
- [23] C. A. Truesdell, *The rational mechanics of flexible or elastic bodies : 1638-1788 : introduction to Leonhardi Euleri Opera Omnia. Vol. 10. et 11., seriei secundae* (1960).
- [24] S. B. Marston and C. W. J. Smith, *J. Muscle Res. Cell. Motil.* **6**, 669 (1985).
- [25] V. M. Vassilev, P. A. Djondjorov, and I. M. Mladenov, *J. Phys. A* **41**, 435201 (2008).
- [26] P. Diggins IV, Z. A. McDargh, and M. Deserno, *J. Am. Chem. Soc.* **137**, 12752 (2015).
- [27] W. Helfrich and R. M. Servuss, *Il Nuovo Cimento D* **3**, 137 (1984).
- [28] A. Magnusson, M. Ristinmaa, and C. Ljung, *Int. J. Solids Struct.* **38**, 8441 (2001).
- [29] H. Irschik and J. Gerstmayr, *Acta Mechanica* **206**, 1 (2009).
- [30] S. S. Antman, *Nonlinear problems of elasticity* (Springer, 2004).
- [31] A. Humer, *Acta Mechanica* **224**, 1493 (2013).
- [32] O. Oshri and H. Diamant, *Soft Matter* **12**, 664 (2016).
- [33] A. Libai and J. Simmonds, *The Nonlinear Theory of Elastic Shells* (Academic Press, 1988).
- [34] E. Reissner, *ZAMP* **23**, 795 (1972).
- [35] A. Pflüger, *Stabilitätsprobleme der Elastostatik* (Springer, 1964).
- [36] G. Yoshiaki, Y. Tomoo, and O. Makoto, *Int. J. Solids Struct.* **26**, 375 (1990).
- [37] M. Batista, *Int. J. Solids Struct.* **87**, 153 (2016).
- [38] S. Lafortune, A. Goriely, and M. Tabor, *Nonlinear Dyn.* **43**, 173 (2006).

- [39] L. Pocivavsek, R. Dellsy, A. Kern, S. Johnson, B. Lin, K. Y. C. Lee, and E. Cerda, *Science* **320**, 912 (2008).
- [40] B. Audoly, *Phys. Rev. E* **84**, 011605 (2011).
- [41] H. Diamant and T. A. Witten, *Phys. Rev. Lett.* **107**, 164302 (2011).
- [42] J. Huang, B. Davidovitch, C. D. Santangelo, T. P. Russell, and N. Menon, *Phys. Rev. Lett.* **105**, 038302 (2010).
- [43] F. Brau, P. Damman, H. Diamant, and T. A. Witten, *Soft Matter* **9**, 8177 (2013).
- [44] H. Diamant and T. A. Witten, *Phys. Rev. E* **88**, 012401 (2013).
- [45] V. Démery, B. Davidovitch, and C. D. Santangelo, *Phys. Rev. E* **90**, 042401 (2014).
- [46] M. Rivetti and S. Neukirch, *J. Mech. Phys. Solids* **69**, 143 (2014).
- [47] M. Rivetti, *Comptes Rendus Mcanique* **341**, 333 (2013).
- [48] S. T. Milner, J. F. Joanny, and P. Pincus, *EPL* **9**, 495 (1989).
- [49] H. Diamant and T. A. Witten, [arXiv:1009.2487](https://arxiv.org/abs/1009.2487) .
- [50] V. Jurdjevic, *Arch. Rational Mech. Anal.* **124**, 305 (1993).
- [51] R. Levien, *Electrical Engineering and Computer Sciences University of California at Berkeley* , 175 (2008).
- [52] M. Nizette and A. Goriely, *J. Math. Phys.* **40**, 2830 (1999).
- [53] P. A. Djondjorov, M. T. Hadzhilazova, I. M. Mladenov, and V. M. Vassilev, *Ninth Int. Geometry, Integrability and Quantization* (2008).
- [54] A. E. Lobkovsky, *Phys. Rev. E* **53**, 3750 (1996).
- [55] A. Föppl , B.G. Teubner, Leipzig, Germany **5**, 132 (1907).
- [56] T. von Kármán, *Encyk. D. Math. Wiss.* **IV**, 311 (1910).
- [57] B. Audoly, *Phys. Rev. Lett.* **83**, 4124 (1999).
- [58] M. Kücken, *Forensic Sci. Int.* **171**, 85 (2007).
- [59] J. Dervaux and M. Ben Amar, *Phys. Rev. Lett.* **101**, 068101 (2008).
- [60] Y. Cohen and I. Procaccia, *Phys. Rev. E* **81**, 066103 (2010).

- [61] A. A. Lee, C. L. Gouellec, and D. Vella, *Extreme Mech. Lett.* **5**, 81 (2015).
- [62] H. King, R. D. Schroll, B. Davidovitch, and N. Menon, *Proc. Natl. Acad. Sci.* **109**, 9716 (2012).
- [63] D. Vella, A. Ajdari, A. Vaziri, and A. Boudaoud, *Phys. Rev. Lett.* **107**, 174301 (2011).
- [64] D. Vella, H. Ebrahimi, A. Vaziri, and B. Davidovitch, *EPL* **112**, 24007 (2015).
- [65] J. Chopin and A. Kudrolli, *Phys. Rev. Lett.* **111**, 174302 (2013).
- [66] J. Chopin, V. Démery, and B. Davidovitch, *J. Elasticity* **119**, 137 (2015).
- [67] M. Ben-Amar and Y. Pomeau, *Proc. Math. Phys. Eng. Sci.* **453**, 729 (1997).
- [68] E. Efrati, E. Sharon, and R. Kupferman, *J. Mech. Phys. Solids* **57**, 762 (2009).
- [69] E. Sharon and E. Efrati, *Soft Matter* **6**, 5693 (2010).
- [70] Y. Klein, E. Efrati, and E. Sharon, *Science* **315**, 1116 (2007).
- [71] E. Efrati, Y. Klein, H. Aharoni, and E. Sharon, *Physica D* **235**, 29 (2007).
- [72] J. Bae, J.-H. Na, C. D. Santangelo, and R. C. Hayward, *Polymer* **55**, 5908 (2014).
- [73] M. Byun, C. D. Santangelo, and R. C. Hayward, *Soft Matter* **9**, 8264 (2013).
- [74] J.-H. Na, N. P. Bende, J. Bae, C. D. Santangelo, and R. C. Hayward, *Soft Matter* **12**, 4985 (2016).
- [75] Y. Klein, S. Venkataramani, and E. Sharon, *Phys. Rev. Lett.* **106**, 118303 (2011).
- [76] M. Marder, *Found. Phys.* **33**, 1743 (2003).
- [77] E. Sharon, B. Roman, M. Marder, G.-S. Shin, and H. L. Swinney, *Nature* **419**, 579 (2002).
- [78] E. Efrati, E. Sharon, and R. Kupferman, *Phys. Rev. E* **80**, 016602 (2009).
- [79] S. Armon, H. Aharoni, M. Moshe, and E. Sharon, *Soft Matter* **10**, 2733 (2014).
- [80] J. Gemmer and S. C. Venkataramani, *Soft Matter* **9**, 8151 (2013).
- [81] J. A. Gemmer and S. C. Venkataramani, *Physica D* **240**, 1536 (2011).
- [82] M. Moshe, I. Levin, H. Aharoni, R. Kupferman, and E. Sharon, *Proc. Natl. Acad. Sci.* **112**, 10873 (2015).
- [83] M. Moshe, E. Sharon, and R. Kupferman, *Phys. Rev. E* **92**, 062403 (2015).

- [84] I. Levin and E. Sharon, *Phys. Rev. Lett.* **116**, 035502 (2016).
- [85] D. Grossman, E. Sharon, and H. Diamant, *Phys. Rev. Lett.* **116**, 258105 (2016).
- [86] O. Oshri, F. Brau, and H. Diamant, *Phys. Rev. E* **91**, 052408 (2015).
- [87] P. J. Hudleston and S. H. Treagus, *J. Struct. Geol.* **32**, 2042 (2010).
- [88] V. M. Kaganer, H. Möhwald, and P. Dutta, *Rev. Mod. Phys.* **71**, 779 (1999).
- [89] W. Lu, C. M. Knobler, R. F. Bruinsma, M. Twardos, and M. Dennin, *Phys. Rev. Lett.* **89**, 146107 (2002).
- [90] A. Gopal, V. A. Belyi, H. Diamant, T. A. Witten, and K. Y. C. Lee, *J. Phys. Chem. B* **110**, 10220 (2006).
- [91] Q. Zhang and T. A. Witten, *Phys. Rev. E* **76**, 041608 (2007).
- [92] K. Y. C. Lee, *Annu. Rev. Phys. Chem.* **59**, 771 (2008).
- [93] M. Kücken and A. C. Newell, *EPL* **68**, 141 (2004).
- [94] E. Cerda, L. Mahadevan, and J. M. Pasini, *Proc. Natl. Acad. Sci.* **101**, 1806 (2004).
- [95] B. Davidovitch, *Phys. Rev. E* **80**, 025202 (2009).
- [96] P. M. Reis, F. Corson, A. Boudaoud, and B. Roman, *Phys. Rev. Lett.* **103**, 045501 (2009).
- [97] D. P. Holmes and A. J. Crosby, *Phys. Rev. Lett.* **105**, 038303 (2010).
- [98] Y. Ebata, A. B. Croll, and A. J. Crosby, *Soft Matter* **8**, 9086 (2012).
- [99] B. Li, Y.-P. Cao, X.-Q. Feng, and H. Gao, *Soft Matter* **8**, 5728 (2012).
- [100] C. C. Donato, M. A. F. Gomes, and R. E. de Souza, *Phys. Rev. E* **66**, 015102 (2002).
- [101] N. Stoop, F. K. Wittel, and H. J. Herrmann, *Phys. Rev. Lett.* **101**, 094101 (2008).
- [102] E. Bayart, S. Deboeuf, F. Corson, A. Boudaoud, and M. Adda-Bedia, *EPL* **95**, 34002 (2011).
- [103] G. W. Hunt, M. K. Wadee, and N. Shiacolas, *J. Appl. Mech.* **60**, 1033 (1993).
- [104] S. Lee and A. Waas, *Int. J. Non. Linear Mech.* **31**, 313 (1996).
- [105] L. Boué, M. Adda-Bedia, A. Boudaoud, D. Cassani, Y. Couder, A. Eddi, and M. Trejo, *Phys. Rev. Lett.* **97**, 166104 (2006).

- [106] S. Deboeuf, M. Adda-Bedia, and A. Boudaoud, *EPL* **85**, 24002 (2009).
- [107] H. Aharoni and E. Sharon, *Nat. Mater.* **9**, 993997 (2010).
- [108] F. Brau, H. Vandeparre, A. Sabbah, C. Poulard, A. Boudaoud, and P. Damman, *Nature Phys.* **7**, 5660 (2011).
- [109] A. D. Cambou and N. Menon, *Proc. Natl. Acad. Sci.* **108**, 14741 (2011).
- [110] R. D. Schroll, E. Katifori, and B. Davidovitch, *Phys. Rev. Lett.* **106**, 074301 (2011).
- [111] H. Vandeparre, M. Piñeirua, F. Brau, B. Roman, J. Bico, C. Gay, W. Bao, C. N. Lau, P. M. Reis, and P. Damman, *Phys. Rev. Lett.* **106**, 224301 (2011).
- [112] M. R. Semler, J. M. Harris, A. B. Croll, and E. K. Hobbie, *Phys. Rev. E* **88**, 032409 (2013).
- [113] L. Zhuo and Y. Zhang, *Int. J. Solids Struct.* **53**, 28 (2015).
- [114] D. Vella, P. Aussillous, and L. Mahadevan, *EPL* **68**, 212 (2004).
- [115] J. Huang, M. Juszkievicz, W. H. de Jeu, E. Cerda, T. Emrick, N. Menon, and T. P. Russell, *Science* **317**, 650 (2007).
- [116] B. D. Leahy, L. Pocivavsek, M. Meron, K. L. Lam, D. Salas, P. J. Viccaro, K. Y. C. Lee, and B. Lin, *Phys. Rev. Lett.* **105**, 058301 (2010).
- [117] D. Vella, M. Adda-Bedia, and E. Cerda, *Soft Matter* **6**, 5778 (2010).
- [118] T. J. W. Wagner and D. Vella, *Phys. Rev. Lett.* **107**, 044301 (2011).
- [119] M. Rivetti and A. Antkowiak, *Soft Matter* **9**, 6226 (2013).
- [120] R. D. Schroll, M. Adda-Bedia, E. Cerda, J. Huang, N. Menon, T. P. Russell, K. B. Toga, D. Vella, and B. Davidovitch, *Phys. Rev. Lett.* **111**, 014301 (2013).
- [121] M. Pineirua, N. Tanaka, B. Roman, and J. Bico, *Soft Matter* **9**, 10985 (2013).
- [122] F. Gesztesy and H. Holden, *Soliton equations and their algebro-geometric solutions* (Cambridge University Press, Cambridge, (2003)).
- [123] F. W. J. Olver, D. W. Lozier, R. F. Boisvert, and C. W. Clark, *NIST Handbook of Mathematical Functions* (Cambridge University Press, New York, (2010)).
- [124] M. Abramowitz and I. A. Stegun, *Handbook of Mathematical Functions* (Dover Publications, 1965).

- [125] L. D. Landau and E. M. Lifshitz, *The classical theory of fields* (Butterworth-Heinemann, Oxford (1998)).
- [126] D. Teychenné, G. Bonnaud, and J.-L. Bobin, *Phys. Rev. E* **49**, 3253 (1994).
- [127] W. Moreau, R. Easther, and R. Neutze, *Am. J. Phys.* **62**, 531 (1994).
- [128] R. Anderson, I. Vetharaniam, and G. Stedman, *Phys. Rep.* **295**, 93 (1998).
- [129] M. B. Green, J. H. Schwartz, and E. Witten, *Superstring Theory* (Vol. 1, Cambridge University Press (1987)).
- [130] C. Coulais, J. T. B. Overvelde, L. A. Lubbers, K. Bertoldi, and M. van Hecke, *Phys. Rev. Lett.* **115**, 044301 (2015).
- [131] N. Stoop and M. M. Müller, *Int. J. Non. Linear Mech.* **75**, 115 (2015).
- [132] O. Oshri and H. Diamant, [arXiv:1606.06552v3](https://arxiv.org/abs/1606.06552v3) .
- [133] E. Cerda and L. Mahadevan, *Phys. Rev. Lett.* **80**, 2358 (1998).
- [134] M. Marder, E. Sharon, S. Smith, and B. Roman, *EPL* **62**, 498 (2003).
- [135] E. Efrati, E. Sharon, and R. Kupferman, *Soft Matter* **9**, 8187 (2013).
- [136] J. Dervaux, P. Ciarletta, and M. Ben-Amar, *J. Mech. Phys. Solids* **57**, 458 (2009).
- [137] M. Pezzulla, S. A. Shillig, P. Nardinocchi, and D. P. Holmes, *Soft Matter* **11**, 5812 (2015).
- [138] J. Dervaux and M. Ben-Amar, *Phys. Rev. Lett.* **101**, 068101 (2008).
- [139] C. D. Santangelo, *EPL* **86**, 34003 (2009).
- [140] M. A. Dias, J. A. Hanna, and C. D. Santangelo, *Phys. Rev. E* **84**, 036603 (2011).
- [141] B. Audoly and A. Boudaoud, *Phys. Rev. Lett.* **91**, 086105 (2003).
- [142] J. Guven, M. M. Müller, and P. Vázquez-Montejo, *J. Phys. A* **45**, 015203 (2012).
- [143] M. M. Müller, M. Ben-Amar, and J. Guven, *Phys. Rev. Lett.* **101**, 156104 (2008).
- [144] M. Ben-Amar and A. Goriely, *J. Mech. Phys. Solids* **53**, 2284 (2005).
- [145] A. Goriely and M. Ben Amar, *Phys. Rev. Lett.* **94**, 198103 (2005).
- [146] M. Lewicka, L. Mahadevan, and M. R. Pakzad, *Proc. Math. Phys. Eng. Sci.* **467**, 402 (2010).

- [147] N. Oppenheimer and T. A. Witten, *Phys. Rev. E* **92**, 052401 (2015).
- [148] J. Kim, J. A. Hanna, M. Byun, C. D. Santangelo, and R. C. Hayward, *Science* **335**, 1201 (2012).
- [149] Y. B. Fu and R. W. Ogden, *Nonlinear Elasticity Theory and Applications* (Cambridge University Press, 2001).
- [150] E. H. Dill, *Arch. Hist. Exact Sci.* **44**, 1 (1992).
- [151] M. A. Biot, *Mechanics of incremental deformations* (John Wiley & Sons, 1965).
- [152] P. G. Ciarlet, *An Introduction to Differential Geometry with Applications to Elasticity* (Springer Netherlands, 2005).
- [153] B. Davidovitch, R. D. Schroll, and E. Cerda, *Phys. Rev. E* **85**, 066115 (2012).
- [154] S. Timoshenko, *Theory of Elasticity 3rd Edition* (Mcgraw-Hill College, 1970).
- [155] J. G. Simmonds and A. Libai, *Comput. Mech.* **2**, 99 (1987).
- [156] M. Lewicka and M. R. Pakzad, *ESAIM: COCV* **17**, 1158 (2011).
- [157] E. Jambon-Puillet, D. Vella, and S. Protiere, *Soft Matter* **12**, 9289 (2016).
- [158] G. R. Marple, P. K. Purohit, and S. Veerapaneni, *Phys. Rev. E* **92**, 012405 (2015).
- [159] P. Chen and J. Viñals, *Phys. Rev. E* **60**, 559 (1999).
- [160] J. Rajchenbach, A. Leroux, and D. Clamond, *Phys. Rev. Lett.* **107**, 024502 (2011).
- [161] O. Lioubashevski, H. Arbell, and J. Fineberg, *Phys. Rev. Lett.* **76**, 3959 (1996).
- [162] J. Wu, R. Keolian, and I. Rudnick, *Phys. Rev. Lett.* **52**, 1421 (1984).
- [163] J. W. Miles, *J. Fluid Mech.* **148**, 451 (1984).
- [164] Y. Jiaren and H. Guoxiang, *Chinese Phys. Lett.* **5**, 305 (1988).
- [165] E. W. Laedke and K. H. Spatschek, *J. Fluid Mech.* **223**, 589 (1991).
- [166] A. Larraza and S. Putterman, *J. Fluid Mech.* **148**, 443 (1984).
- [167] G. L. Lamb, *Rev. Mod. Phys.* **43**, 99 (1971).
- [168] R. M. DeLeonardis, S. E. Trullinger, and R. F. Wallis, *J. Appl. Phys.* **51**, 1211 (1980).

- [169] G. Costabile, R. D. Parmentier, B. SaCostabilevo, D. W. McLaughlin, and A. C. Scott, *Appl. Phys. Lett.* **32**, 587 (1978).
- [170] G. Rizzi and M. L. Ruggiero, *Relativity in Rotating Frames* (Kluwer Academic, Dordrecht, The Netherlands (2004)).
- [171] R. Rynasiewicz, *Philos. Sci.* **67**, 70 (2000).
- [172] H. Goldstein, C. Poole, and J. Safko, *Classical Mechanics* (3rd edition, Addison-Wesley (2002)).

משקל מכאני. עבור מטריקת מטרה בעל עקמומיות גאוסיאנית חיובית, נמצא כי כיפה כדורית מקיימת את התנאי לשיווי משקל עד כדי איזור צר של שכבת גבול בקצותיה.

לסיכום, התוצאות המובאות בעבודה זו מהוות צעד נוסף לעבר מציאת תיאוריה עיקבית ומלאה שתוכל לתאר גופים אלסטיים דקים העוברים מעוותים גדולים, רחוק מאד ממצב שיווי המשקל הרפוי שלהם.

תקציר

היווצרות תבניות ספונטאניות בתווך אלסטי בכלל, ועל יריעות אלסטיות דקות בפרט, היא כיום תחום מחקר מוביל ופעיל בתחום הפיזיקה של החומרים הרכים. יריעה אלסטית דקה היא חומר מוצק מאקרוסקופי תלת-ממדי שהעובי שלו קטן מאד יחסית לשאר לממדיו. בשל תכונה ייחודית זו יריעות דקות הן גמישות מאד וניתנות לכיפוף בקלות יתרה. לכן ע"י הפעלת כוחות חיצוניים (לרב קטנים מאד), נוצרים מבנים מורפולוגיים עשירים על פני השטח של היריעה. עבודה זו באה להרחיב את התיאוריה של יריעות דקות בשלושת הפרויקטים הבאים:

הפרויקט הראשון עוסק ביריעה דקה המונחת על גבי מצע נוזלי ונתונה לכוחות דחיסה ציריים משני צדדיה. כאשר מקרבים במעט את שני קצותיה של היריעה, מופיע על פניה מבנה גלי-מחזורי המשתרע על כל שטחה ושניתן לאפינו ע"י אורך גל המוגדר היטב, λ . כאשר ממשיכים לקרב את שני קצותיה של היריעה האחד אל עבר השני, המבנה שעל פניה משתנה והופך בהדרגה ממחזורי-גלי למבנה ממוקם בו כל הדפורמציה נמצאת במרכז היריעה. עבודה קודמת שעסקה במערכת זו מצאה פתרון מדויק כאשר אורך היריעה נלקח כאינסופי. מפתרון זה נמצא שהמבנה הגלי בלתי-יציב לכל דחיסה צירית, קטנה ככל שתהיה. בעבודה הנוכחית אנו מרחיבים את התיאוריה הקיימת ליריעות בעלות אורך סופי, L , כדי שנוכל לנתח את המעבר שנצפה בניסויים בין המבנה הגלי למבנה הממוקם. בעזרת התיאוריה המורחבת אנו מוצאים פתרונות מדויקים למבנה הגלי עבור יריעות באורך סופי ופתרונות מקורבים למבנה הממוקם. בנוסף אנו מנתחים את המעבר בין שני המבנים ומוצאים שהוא מתנהג כמעבר פאזה מסדר שני. הנקודה הקריטית בה מתרחש השינוי היא כאשר שני צידי היריעה מוזזים ב- $\Delta_F = \lambda^2/L$.

הפרויקט השני עוסק באנלוגיה שבין מוטות אלסטיים דקים (או יריעות דקות המכופפות בכיוון אחד בלבד) לתנועה של גופים קשיחים. האנלוגיה הקינטית של קירכהוף מקשרת בין מוטות אלסטיים דקים שאינם דחיסים לבין התנועה של גופים קשיחים. בעבודה זו אנו מרחיבים את האנלוגיה של קירכהוף למוטות דקים אך דחיסים ומראים שהתיקונים האלסטיים הנובעים מתוספת זו שקולים לתיקונים יחסותיים לתנועה של גופים קשיחים. בעזרת האנלוגיה המורחבת אנו מוצאים סימטריה חדשה למוטות אלסטיים דחיסים ובנוסף, ע"י שימוש בפתרונות ידועים לגופים אלסטיים, אנו מוצאים פתרון מדויק לתנועה של מטוטלת פיזיקלית יחסותית. לבסוף אנו דנים כיצד האנלוגיה המורחבת יכולה לעזור ללימוד מערכות אחרות של גופים רכים.

הפרויקט השלישי עוסק ביריעות אלסטיות דקות ומתוסכלות – יריעות אלסטיות הנתונות למאמצים פנימיים גם ללא הפעלת כוחות חיצוניים. התיאוריה הקיימת ליריעות אלסטיות מתוסכלות מבוססת על טנזור מעוותים המודד שינויים של מטריקת המשטח לפני ואחרי הדפורמציה. עבור בעיות פשוטות בעלות סימטריה סיבובית אנו בוחנים תאוריה אלטרנטיבית המוגדרת ע"י טנזור מעוותים המבוסס על מדידת אורכים (במקום אורכים בריבוע). בעוד שתי התיאוריות מתכנסות בגבול של מעוותים קטנים מאד ובגבול של יריעות בלתי-דחיסות, עבור מקרים אחרים אנו מוצאים ששתי התיאוריות נבדלות אחת מהשנייה. התיאוריה החלופית מציגה מספר תכונות שאינן קיימות בתיאוריה הנוכחית: (א) עבור דפורמציות שטוחות מתקבלת משוואת שיווי משקל ליניארית פתירה במדויק. (ב) התיאוריה החדשה מתלכדת עם תורת האלסטיקה המקובלת למוטות דחיסים כאשר היריעה מורשית להתעוות בכיוון אחד בלבד. באופן ספציפי, ממודל זה מתקבל שמוט המכופף לרדיוס קבוע איננו משנה את אורכו. (ג) מתוך התיאוריה החדשה מתקבל קריטריון פשוט הקובע האם יריעה ללא מעוותים פנימיים (הניתנת לשיכון איזומטרי במרחב) נמצאת בשיווי

עבודה זו נעשתה בהדרכתו של

פרופסור חיים דימנט

אוניברסיטת תל אביב



הפקולטה למדעים מדויקים
ע"ש ריימונד ובברלי סאקלר
בית הספר לפיזיקה ואסטרונומיה

חיבור לשם קבלת התואר "דוקטור לפילוסופיה"

היווצרות תבניות בריעות אלסטיות דקות

הוגש לסנאט של אוניברסיטת תל אביב על ידי

עוז אושרי

מנחה: פרופ' חיים דימנט

פברואר 2017